Strengthening of thin metallic cylindrical shells using fibre reinforced polymers

Thesis submitted in fulfilment of the requirements for the degree of Doctor of Philosophy

By

Mustafa Batikha

Supervisors: Professor J. Michael Rotter

Dr. Jian-Fei Chen

Institute for Infrastructure & Environment

The School of Engineering and Electronics

The University of Edinburgh

William Rankine Building, The King's Buildings, Edinburgh, Scotland, UK

EH9 3JL

2008

Declaration

This thesis entitled “Strengthening of thin metallic cylindrical shells using fibre reinforced polymers”, is submitted to the Institute for Infrastructure & Environment, The School of Engineering and Electronics, The University of Edinburgh, William Rankine Building, The King's Buildings, Edinburgh, EH9 3JL, for the Degree of Doctor of Philosophy.

The research was solely the work of the author expect where otherwise acknowledged in the text and has not formed the basis of a submission for any other degree. Publications based on this thesis:

Batikha M, Chen JF and Rotter JM (2007). “FRP strengthening of metallic cylindrical shells against elephant‘s foot buckling.” Proc. of the Conference on Advanced Composites in Construction, ACIC 07, 2-4 April, Bath, UK, 157-164.

Batikha M, Chen JF and Rotter JM (2007). “Numerical modelling of shells repaired using FRP.” Proc. of the 3rd International Conference on Steel and Composites Structures, ICSCS 07, 30 July-1 August, Manchester, UK, 1065-1069.

Batikha M, Chen JF, Rotter JM (2007). “Elastic buckling of FRP-strengthened cylinders with axisymmetric imperfections”. Proc., Asia-Pacific Conference on FRP in Structures, APFIS 2007, 12-14 December, Hong Kong, 1011-1016.

Batikha M, Chen JF, Rotter JM (2008). “Strengthening metallic shells with FRP against buckling”. Proc. of the 4th International Conference on FRP Composites in Civil Engineering, CICE 2008, 22-24 July, Zurich, Switzerland, accepted.

Mustafa Batikha

Date

Abstract

Steel silos are widely used as long-term or short-term containers for the storage of granular solids, of which a huge range are stored, from flour to iron ore pellets, coals, cement, crushed rocks, plastic pellets, chemical materials, sand, and concrete aggregates. The radius to thickness ratio for silos is in the range of 200 to 3000, so they fall into the category of thin shells, for which failure by buckling is the main concern and requires special attention in design. The primary aim of this thesis is to investigate the possible application of Fibre Reinforced Polymer (FRP) as a new repair and strengthening technique to increase the buckling capacity of thin metallic cylindrical shells. Extensive research has been conducted on the use of fibre reinforced polymer (FRP) composites to strengthen concrete, masonry and timber structures as well as metallic beams. However, all these studies were concerned with failure of the structure by material breakdown, rather than stability. As a result, this thesis marks a major departure in the potential exploitation of FRP in civil engineering structures.

Many analyses of cylindrical shells are presented in the thesis. These are all focussed on strengthening the shell against different failure modes. Two loading conditions were explored: uniform internal pressure accompanied by axial load near a base boundary, and axial loads with geometric imperfections. For the latter, local imperfections are usually critical, and two categories of imperfection were studied in detail: an inward axisymmetric imperfection and a local dent imperfection.

For the first loading condition, which leads to elephant's foot buckling, an analytical method was used to derive general equations governing the linear elastic behaviour of a cylindrical shell that has been strengthened with FRP subject to internal pressure and axial compression. It was used to identify optimal application of the FRP. All the later studies were conducted using nonlinear finite element analysis (using the ABAQUS program) to obtain extensive predictions of many conditions causing shell buckling and the strengthening effect of well-placed FRP.

In all the cases studied in this thesis, it was shown that a small quantity of FRP composite, applied within a small zone, can provide a significant enhancement of the resistance to buckling failure of a thin metal cylinder. These calculations demonstrate that this new technique is of considerable practical value. However, it is clear that not all the relevant questions have been fully answered, so the author poses appropriate questions and makes suggestions for future work.

Acknowledgements

I am very grateful to Professor J Michael Rotter for his continued encouragement and his helpful guidance in doing this research. The first time I met him he promised I would complete on time, his promise has come true. I owe Professor Rotter a debt of gratitude for his careful reading of this thesis and the corrections and suggestions he has made.

I would like also to thank Dr. Jian-Fei Chen for his help, guidance and the good ideas he suggested during this research.

The author gratefully acknowledges the financial support of Damascus University during the years of this research.

I would like to express my special thanks to my parents who are always with me.

I thank my sisters, brothers and friends who are always encouraging me through the difficult times.

Finally, I would like to express my warm appreciation for three of my friends who accompanied me daily throughout this research: Hamdi Habbab, Li Yang and Nadir Yousif.

Thank you all for your support.

Notation

The symbols used in this thesis are listed below. Only one meaning has been assigned to each symbol unless otherwise defined in the text where the symbol occurs.

Symbol	Meaning
σ_{cl}	classical elastic buckling stress
E	Young's modulus
ν	Poisson's ratio
t	shell wall thickness
R	cylinder radius
Z	Batdorf parameter
L	cylinder length
λ	bending half –wavelength
GNA	Geometrical Nonlinear Analysis
e_2	ring eccentricity
a	distance between rings
E_L	Young's modulus of the FRP lamina in fibre direction
E_T	Young's modulus of the FRP lamina in transverse direction
G_{LT}	in-plane shear modulus of the FRP lamina
ν_{LT}	Poisson's ratio of the FRP lamina
E_f	Young's modulus of the fibre
ν_f	Poisson's ratio of the fibre
E_m	Young's modulus of the resin

G_m	shear modulus of the resin
ν_m	Poisson's ratio of the resin
V_f	fibre volume friction
V_m	matrix volume friction
W_f	fibre weight
$[T]$	transformation matrix from (θ,z) coordinate system to (L,T) coordinate system
$[Q]$	stiffness matrix
$\{\kappa\}$	the change of curvature
$\{\varepsilon\}$	strain matrix in the reference surface.
$[A]$	in-plane stiffness matrix
$[B]$	extension-bending coupling matrix
$[D]$	bending stiffness matrix
$[\tilde{D}]$	modified bending stiffness ($[\tilde{D}] = [D] - [B]^T [A]^{-1} [B]$)
B_θ	extensional stiffness of a layered shell in circumferential direction
B_z	extensional stiffness of a layered shell in meridional direction
$C_{\theta z}$	shear stiffness of a layered shell in (θ, z) plane.
D_θ	bending stiffness of a layered shell in circumferential direction
D_z	bending stiffness of a layered shell in meridional direction
$D_{\theta z}$	twisting stiffness of a layered shell
μ_θ	Poisson's ratios associated with bending in circumferential direction
μ_z	Poisson's ratios associated with bending in meridional direction
μ'_θ	Poisson's ratios associated with extension in circumferential direction
μ'_z	Poisson's ratios associated with extension in meridional direction
h	height of the cylindrical shell
t_s	thickness of the metal cylinder

E_s	Young's modulus of the metal cylinder
ν_s	Poison's ratio of the metal cylinder
h_f	height of FRP sheet
t_f	Thickness of FRP sheet
x_f	starting distance of FRP sheet above the base
$E_{f\theta}$	Young's modulus of FRP sheet in the circumferential direction
E_{fz}	Young's modulus of FRP sheet in the meridional direction
$\nu_{f\theta}$	Poisson's ratio of FRP sheet in the circumferential direction
p	uniform internal pressure
N_z	vertical load per unit circumference
w	radial displacement
β	circumferential rotation
D	shell flexural rigidity
D_s	shell flexural rigidity for the metal.
D_{fz}	shell flexural rigidity of FRP sheet in meridional direction.
N_{zs}	axial force in the cylindrical metal shell.
N_{zf}	axial force in the FRP shell.
α	extensional stiffness ratio ($E_{f\theta}t_f/E_st_s$)
t_b	effective thickness for the composite FRP-steel section.
LA	Linear elastic Analysis
GMNA	Geometrically and Materially Nonlinear Analysis
GNIA	Geometrically Nonlinear Analysis with Imperfections
w_m	membrane theory normal deflection
λ_b	meridional bending half-wavelength for the composite FRP-steel section.
w_{mb}	membrane theory normal deflection for the composite FRP-steel section.
N_θ	circumferential stress resultant
M_z	bending moment in meridional direction
M_θ	bending moment in meridional direction
Q_z	shear stress resultant in meridional direction

σ_{vM}	von Mises stress
σ_{mz}	meridional membrane stress.
$\sigma_{m\theta}$	circumferential membrane stress
σ_{bz}	meridional bending stress
σ_{vM0}	membrane von Mises
α_z	meridional elastic imperfection factor
Δw_k	characteristic imperfection amplitude
Q	meridional compression fabrication quality parameter
δ_0	imperfection amplitude
λ_0	half wavelength for the adopted shape of imperfection.
y	circumferential coordinate from the centre of the dent ($y=R\theta$)
L_z	half wavelength characterising the dent height.
L_θ	half wavelength characterising the width of the rectangular dent.
L_{sq}	square dent dimension
L_{sqm}	critical square dent size
n_{cl}	buckling mode wave number of the perfect cylinder
L_{zw}	dent height in the Wullschleger (2006) study
$L_{\theta w}$	dent width in the Wullschleger (2006) study
δ_0^*	marginal initial dent amplitude for the critical dimensions in the Wullschleger (2006) study.

Contents

Chapter 1

Introduction

1.1 General background on steel silos

Steel silos are widely used as long-term or short-term containers for the storage of granular solids. Granular solids cover a huge range of materials such as flour, iron ore pellets, coals, cement, crushed rocks, plastic, chemical materials, sand, concrete aggregate, etc.

The plan form of silos can take a rectangular shape or a circular shape; the latter covers the majority of steel silos as it is structurally more efficient.

In general, silos can be divided into two categories: ground-supported silos (Fig.1-1) or elevated silos which consist of cylindrical shell, barrel, and a conical hopper (Fig.1-2). The second category is preferred because the bulk solid can be discharged by gravity flow. However, elevated silos are supported to the ground using a long skirt or columns which can be terminated below the transition, extended to the top ring or terminated part way into the cylinder. It is worth mentioning that the radius to thickness ratio for silos is in the range of 200 to 3000. Therefore, silos fall into the category of thin wall shells where buckling failure is the main concern and demands special attention.

The buckling of a thin metal shell has been studied scientifically since the early twentieth century (Timoshenko, 1936). The classical period of those studies refers to

the period between the 1900s and the 1970s with simple load cases and small geometric imperfections, before the computer era when finite element analysis started to be used as a powerful tool together with non-linear equilibrium paths. Then, the discrepancy between the theoretical and the experimental strengths started to be more comprehensively explored and explained (Teng and Rotter, 2004). It was shown (Teng and Rotter, 2004) that four factors control this discrepancy: pre-buckling deformations, boundary conditions, eccentricities and non-uniformities in applied load or support, and geometric imperfections. However, the effect of geometric imperfections was considered to have a more significant influence on buckling strength than the other factors (Yamaki, 1984; Teng and Rotter, 2004). Consequently, researchers are still working to investigate this subject and are including it in other areas of exploring the buckling of thin metal shells.

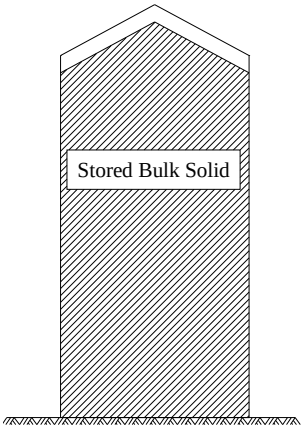

Figure 1.1: Ground supported silo

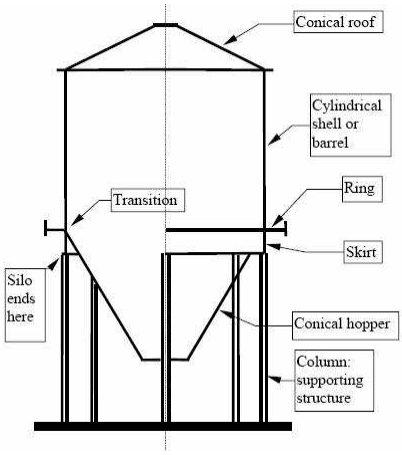

Fig. 1-2: Terminology used in silo structures (BS EN1993-4-1:2007; Rotter, 2001).

Strengthening metal shells against buckling was to become the concern of many researchers. Ring stiffeners and stringers were used widely (Singer, 2004). The purpose of ring stiffeners is to increase the buckling strength, whereas the role of stringers is to increase the axial or bending strength (Singer, 2004). Moreover, the effect of the position of the ring or stringer inside or outside the silo on the buckling strength was a field to be explored by many researchers (Singer *et al.*, 1966). It was seen that both cylindrical shell length and boundary conditions affect the buckling strength. For instance, using the outside ring is more effective for short shells (Singer *et al.*, 1966). Another example is end rotational restraint is effective for short stringer-stiffened cylindrical shells, while by contrast the axial restraint is more important for long ones (Singer *et al.*, 1967).

1.2 General background on fibre reinforced polymer, FRP

Fibre reinforced polymer, FRP, is composed of two principal elements: fibres and resin material, where the fibres give FRP the strength, whereas the resin binds the fibres together. The fibres are made from carbon, aramid or glass. Therefore, the strength can be varied, depending on the kind of fibres used in making FRP. However, the strength of FRP can be at least twice, and as much as 10 times as strong as steel plates.

The advantages of using FRP as a strengthening technique can be stated as follows (Cripps, 2002; Teng *et al.*, 2002; Technical report No. 55 of Concrete Society, 2004):

High strength to weight ratio: Lifting equipment eliminated; reduced labour cost, speedy application; minimal increases in weight and size

Durable performance: many examples show that external GFRP cladding units which are 25 years old or more are still looking good. However, regular re-painting is required.

Flexibility of shape: can be handled in rolls; easy for wrapping on curved surfaces and around columns and shells.

Non-conducting and non magnetic: safety in high powered electrical systems, except carbon fibre.

Easily cut to length on site.

Overlapping ability because the material is thin.

Increasing the ductility of the element, consequently effective seismic resistance.

Applying to the external surface with no need of access to the interior in the case of storage structures.

The chief disadvantages of using FRP are: first; the environmental impact with chemical-producing FRP and difficulties in recycling. Moreover, the resins absorb water, and the moisture affects the properties of FRP if it reaches the fibre/matrix interfaces. However, modern FRP versions are less sensitive to moisture or temperature. Secondly; there is the problem of fire where most polymers will burn when exposed to fire.

FRP is linear elastic with no stress redistribution because FRP has a straight line stress-strain response with no yielding until rupture. Further, the compressive strengths of carbon and glass fibres are close to their tensile strengths; that of aramid is significantly lower in compression (Technical report No. 55 of Concrete Society, 2004).

The first use of FRP to strengthen structures was with concrete elements; extensive research has been undertaken in this area since the 1990s (Teng *et al.*, 2002). This FRP research has been extended to the strengthening of metallic beams, masonry and timber structures (Triantafillou, 1998; Gilfillan, 2003; Cadei *et al.*, 2004). In all these cases, strength, rather than stability, was the main concern. The use of FRP to increase the buckling strength of thin metallic shells has scarcely been explored at all.

1.3 Objectives and scope of this thesis

The primary aim of this study is to investigate the application of FRP to increase the buckling capacity of thin metallic cylindrical shells.

The work presented in this thesis may be conveniently divided into two conditions for cylindrical shell buckling: internal pressure accompanied by axial load, and axial loads with geometric imperfections.

Thin cylindrical shells are sensitive to the magnitude of the imperfections, which can cause elastic buckling near a local imperfection if the internal pressure is

small, but under high internal pressure, this sensitivity is much reduced. It was shown (Rotter, 1990; Teng and Rotter, 1992) that elastic-plastic buckling occurs under high internal pressure with a local reduction of the flexural stiffness due to plasticity near the boundary conditions. Under this local reduction, an increase in the radial displacements leads to a rise in the circumferential membrane stress resultant, and elastic-plastic collapse, known as elephant's foot buckling, results (Rotter, 1990).

Linear elastic shell Analysis, LA, and Geometrically and Materially Nonlinear Analysis, GMNA, are used in this thesis to show that a small amount of FRP, placed at the critical location, can significantly decrease the radial deformation of the shell, leading to an increase of the elephant's foot buckling strength.

In the second set of studies, Geometrically Nonlinear elastic Analysis with Imperfections included, GNIA, is considered when exploring the elastic buckling strength of an FRP strengthened cylindrical shell under axial loads only with both axisymmetric inward imperfections and local dents.

1.4 Structures of the thesis

The thesis is divided into seven chapters. A brief description for each chapter is presented below:

Chapter 1 introduces the background to the many ideas used in this thesis, the objectives and scope of this research and the structure of the thesis.

Chapter 2 reviews the literature relating to this study. It describes the historical background to the buckling of cylindrical shells, FRP strengthened structures and FRP strengthening of metallic shells.

Chapter 3 gives a brief review of FRP properties and modelling. It describes the principles which need to be considered when the FRP is analysed.

Chapter 4 presents a preliminary study of the strengthening of pressurized cylindrical shells using externally bonded FRP. The linear elastic equations for the strengthened cylinder are derived for both pinned and fixed base boundary conditions. In addition, the optimal dimensions of the FRP sheet together with the critical location are obtained to prevent a local peak radial displacement from occurring.

Chapter 5 explores the use of FRP to strengthen a thin cylindrical shell against elephant's foot buckling. In this chapter, geometrically and materially nonlinear analysis is undertaken to explore the effectiveness of an FRP sheet against elephant's foot buckling. As in chapter 4, the optimal FRP dimensions are derived for this case too.

Chapter 6 examines the elastic buckling strength of an FRP strengthened cylindrical shell with axisymmetric inward imperfections under axial loads. In this chapter, the effects of the amplitude of the imperfection, the FRP stiffness and the FRP height are investigated.

Chapter 7 presents the buckling behaviour of a cylindrical metal shell with a dent, and strengthened with FRP. Different amplitudes of the initial depth of the dent are studied and the elastic buckling strength is found for different dimensions of the dent. The strengthening of a rectangular dent using FRP is studied as an example. For this case, both different FRP sheet stiffness and FRP sheet dimensions are investigated to optimise the gain in buckling strength.

Chapter 8 presents the conclusions drawn from the previous chapters. Recommendations for further research are also made.

Chapter 2

Literature review

2.1 Introduction

As indicated in Section 1.3, the primary aim of this thesis is to explore the buckling capacity of thin metal cylindrical shells using FRP.

Therefore, this chapter starts with a description of the most relevant works in the area of buckling of cylindrical shells. In this thesis, the focus is on two conditions in cylindrical shells: internal pressure accompanied by axial load and axial loads with geometric imperfections. The content of this chapter reflects this focus.

Background information on the strengthening of cylindrical shells is given, and some typical techniques are discussed for preventing the collapse of the cylindrical shells.

Previous studies of the application of FRP composites to strengthen structures are identified. Current work on the strengthening of cylindrical shells against buckling using FRP is also described.

Finally, a summary of this chapter is given, identifying the new studies presented in this thesis.

2.2 Buckling of thin cylindrical shells

The buckling of thin cylindrical shells is a complex field compared with columns or flat plates, where the classical buckling theory can give a good prediction of their buckling capacity. The reason is that shells often have an unstable postbuckling behaviour, as shown in Fig. 2-1.

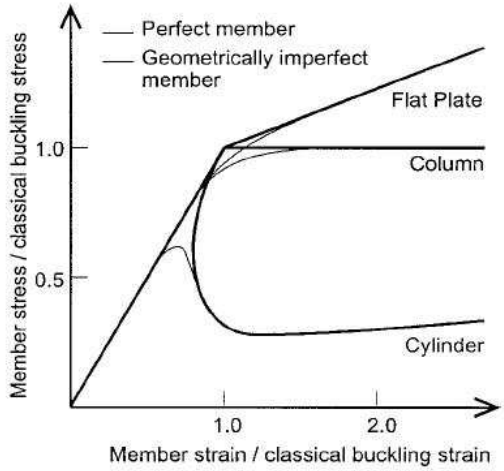

Fig. 2-1: Buckling behavior of columns, flat plates and cylindrical shells (Pircher and Bridge, 2001).

Figure 2-1 indicates how, before the critical buckling load is reached, all these systems show a linear response. Beyond the buckling strength, columns cannot develop transverse stresses to restrain additional out-of-plane displacements (Pircher and Bridge, 2001; Singer *et al.*, 1998). By contrast, the flat plate continues to carry increased loading. Plates lose only a part of their load carrying capacity at buckling, because of the redistribution of the normal stress (Singer *et al.*, 1998).

However, the buckling of a thin cylindrical shell is completely different. The load drops abruptly after the critical strength has been reached, and reaches a highly deformed postbuckling condition.

The buckling of thin metal shells has been studied scientifically since the early twentieth century. The period between the 1900s and the 1970s can be referred to as the classical period of those studies, when both classical solutions (Timoshenko, 1936; Flügge 1973) and massive sets of tests (Singer *et al.*, 2002) were produced for shell buckling under simple loads and with small geometric imperfections. The linear bifurcation stress, known as classical elastic buckling stress, σ_{cl} (Eq. 2-1), was found early (Lorenz, 1908; Timoshenko, 1910; Southwell, 1914):

$$\sigma_{cl} = \frac{E}{[3(1-\nu^2)]^{1/2}} \frac{t}{R} \approx 0.605 \; E \frac{t}{R} \tag{2-1}$$

in which E is Young's modulus, ν is Poisson's ratio (around 0.3 for steel), t is the shell wall thickness and R is the cylinder radius.

However, the discrepancy between the classical theory strength and the test was too great to be accepted, and was affected by one of four factors (Teng and Rotter, 2004):

Prebuckling deformations and their contributions in changing the stress.

Boundary conditions.

Eccentricities and non-uniformities in applied load or support.

Geometric imperfections and residual stresses.

Since then, the computer era has given researchers a huge motivation to acquire more understanding about this discrepancy. The application of finite element analysis, together with non-linear equilibrium paths, was a valuable step to find the answers to many questions.

Studies of prebuckling deformations show that they have a small effect (~15%) on the difference between the theory and tests (Teng and Rotter, 2004).

The effect of the boundary conditions was explored extensively. Yamaki (1984) presented different boundary conditions, described in Table 2-1 below. The boundary conditions were found to have very little influence on buckling strength, with the fact that most cylindrical shells fall into the category of medium length, as described in Eurocode 3 Part 1.6 (2007).

The concept of shell length is defined according to the buckling response of cylindrical shells (Rotter, 2004). The short cylinder buckles in one or two buckle waves down the cylinder length (Fig. 2-2a), whereas medium cylinders fail by a series of diamond patterns, chequer-board or outward axisymmetric buckles (Fig. 2-2c). By contrast, very long cylinders collapse by Euler buckling as a column with no distortion of the circumferential cross section (Rotter, 1990; Rotter, 2004; Chajes, 1985), as illustrated in Fig. 2-2b.

The effects of both boundary conditions and shell length are demonstrated in Fig. 2-3, where shell length is defined in terms of the Batdorf parameter, Z, given by Eq. 2-2:

$$Z = \sqrt{1-v^2}\,\frac{L^2}{Rt} \cong 5.7(\frac{L}{\lambda})^2 \tag{2-2}$$

where L is the cylinder length and λ is the linear bending half –wavelength (Eq. 2-3):

$$\lambda = \frac{\pi}{(3(1-v^2))^{1/4}}\sqrt{Rt} = 2.444\sqrt{Rt} \tag{2-3}$$

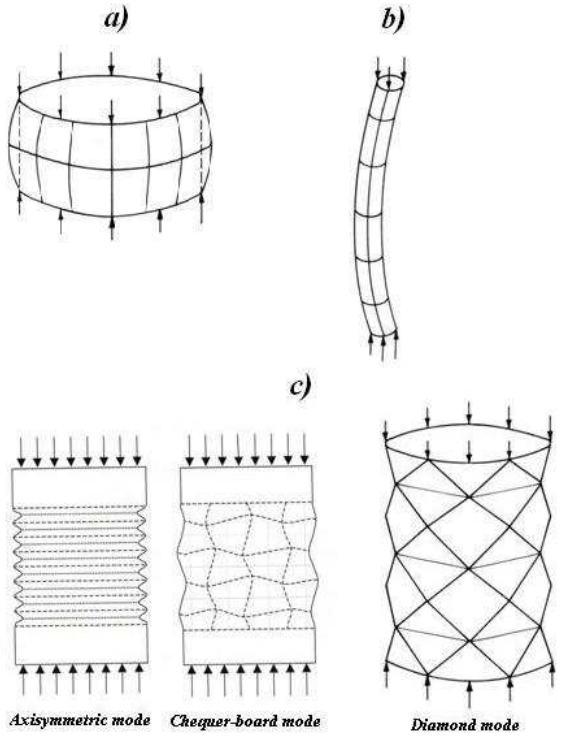

Fig. 2-2: Buckling modes for axially compressed cylinders (Chajes, 1985; Rotter, 2004)

Table 2-1: Critical buckling strength for different boundary conditions (Yamaki, 1984; Rotter, 2004)

Name	δu	δv	δw	δβ	Name	δu	δv	δw	δβ
S1	r	r	r	f	C1	r	r	r	r
S2	r	f	r	f	C2	r	f	r	r
S3	f	r	r	f	C3	f	r	r	r
S4	f	f	r	f	C4	f	f	r	r

Notes:

f =free to displace during buckling.

r=restrained displacement during buckling.

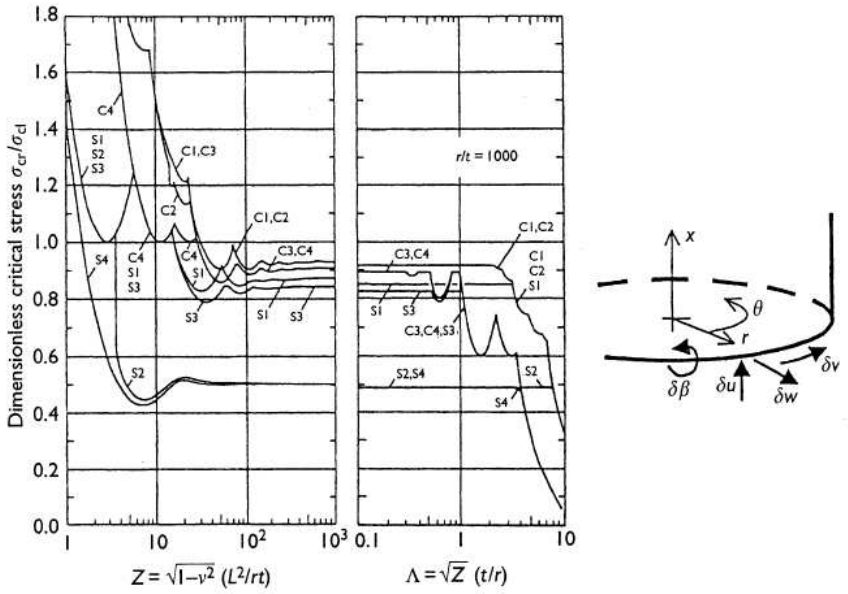

Fig. 2-3: Effect of boundary conditions and shell length on perfect elastic shell buckling load (Rotter, 2004; Yamaki, 1984)

For medium length cylinder ($Z>50$, $\Lambda<1$), the boundary conditions have little effect on buckling strength, except for the boundary conditions S2 and S4 (Fig. 2-3). Figure 2-3 also shows that prebuckling deformations affect the buckling strength by about 8% for C1 to 17% for S3 from the classical value. Further, when the circumferential displacements, δv, are not restrained for the pinned boundary condition (S2 and S4), the buckling stress for the perfect shell falls to about half of its classical strength. Short elastic cylinders provide high buckling strength, as seen in Fig. 2-3.

2.2.1 Imperfect cylinders

The effect of geometric imperfections was considered to have a very significant influence on buckling strength. A lap joint (Rotter and Teng, 1989; Rotter, 1998; 2004) causes a local eccentricity in the thrust of vertical line in the cylinder wall and consequently produces a local bending moment. In addition, the moving of the shell inwards and outwards brings local membrane circumferential stresses to be combined to the membrane meridional stresses, causing buckling failure. The shape of imperfections was studied extensively to show that local axisymmetric imperfections give a dramatic reduction to the buckling strength under

pure axial load (Rotter and Teng, 1989; Rotter, 1996; 2004). In addition, it was seen that the elastic buckling strength is independent of radius to thickness ratio (Rotter and Teng, 1989). Moreover, the boundary conditions are not important for the buckling strength with imperfections far away from the ends (Rotter, 1997; Pircher and Bridge, 2001).

For internally pressurized cylinders, the collapse load is less sensitive to the wall imperfections (Rotter, 1990; Teng and Rotter, 1992). Changing the buckling mode from diamond to a very local axisymmetric at high internal pressure reduces the imperfection sensitivity (Rotter and Teng, 1989; Rotter, 1990; Rotter and Zhang, 1990). Plastic instability occurs in the region of local bending near the boundary condition. This leads to more stable postbuckling behaviour (Rotter, 2004). Rotter (1997) showed that unpressurized cylinders with radius to thickness ratio, R/t, less than 400 buckle plastically. Moreover, Rotter and Teng (1989) presented that the meridional form of the buckling mode is very localized in thin shells, while thick shells provide a buckling mode for the whole shell, so the boundary conditions become important.

2.2.2 Non-uniform loads in silo design

Non-uniformly loads need to be considered when the buckling design of a silo is undertaken. The eccentricities of filling and discharge, (Fig. 2-4), are an instance of this. The pressures on vertical walls of silos are obtained in terms of a fixed load and a free load (Rotter, 2001; BS EN 1991-4:2006). The fixed loads are defined as Janssen filling pressures in silos, demonstrated by Rotter (2001), while, in contrast, free load, known as patch load, ensures that the unavoidable unsymmetrical loads are taken into account during the design.

Local patch loads from eccentricities of filling and discharge defined by BS EN 1991-4 (2006) vary in a sine wave around the circumference, extend over a specified zone and are to be added to those obtained from symmetrical loading. Further, applying a patch load should be investigated for different positions on the silo wall.

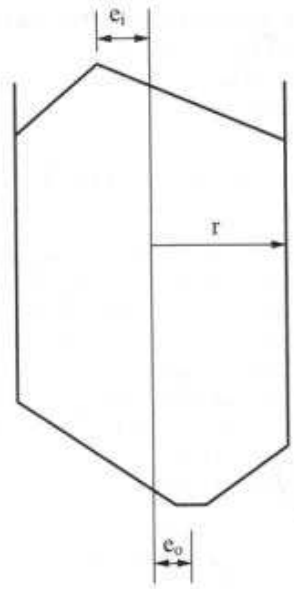

Fig. 2-4: Eccentricities of filling and discharge (Rotter, 2001).

Gillie and Rotter (2002) explored the effect of changing the circumferential width, the vertical extent and the pressure distribution form for the patch load. It was found that the silo responds as there is a point load when the patch load is small. In contrast, a wide patch load causes the silo to behave as if a distributed load is applied. Moreover, a patch load wider than 30° provides circumferential membrane stresses which are independent of the patch size or application height.

Wind load is another example of the effect of non-uniform loads. Wind pressures on a silo wall have been studied widely (Greiner, 1998). Greiner and Guggenberger (2004) found that buckling occurs in the mid-height region of the shell in the stagnation zone. Also, Greiner and Derler (1995) showed that, for short shells, buckling is governed by circumferential compression and the buckles cover the whole height of the cylinder. For medium length cylinders, the classical buckling analysis indicates that buckling occurs at the lower edge by shear and axial compression or by a combination of both, but geometrical nonlinear analysis shows that the buckles move to the mid height of the cylinder. Further, the buckling strength is reduced to about 50% of the classical load. The importance of geometric nonlinearity is obvious from that study.

2.3 Typical techniques for strengthening cylindrical shells against buckling

Strengthening cylindrical shells against buckling has been extensively studied by researchers. Ring stiffeners and stringers (longitudinal stiffeners) were used widely as typical techniques for reinforcing cylindrical shells against buckling. Ring stiffeners are used mainly to enhance the buckling resistance to external pressure, while stringers are applied to increase the axial buckling strength efficiently (Singer, 2004). However, they may give much effective enhancement for the cylinder if they act together (Singer *et al.,* 2002). It was shown that buckles will occur in the wall if the ring is stocky but shell wall is thin. However, the ring itself is susceptible to buckling if it is made from slender plate or shell segments (Teng and Zhao, 2004). Singer (2004) and Singer *et al.* (2002) described the buckling modes of ring-stiffened shells. They can be divided into three cases: local shell instability (Fig. 2-5a), overall collapse (Fig. 2-5b) and axisymmetric plastic collapse (Fig. 2-5 c).

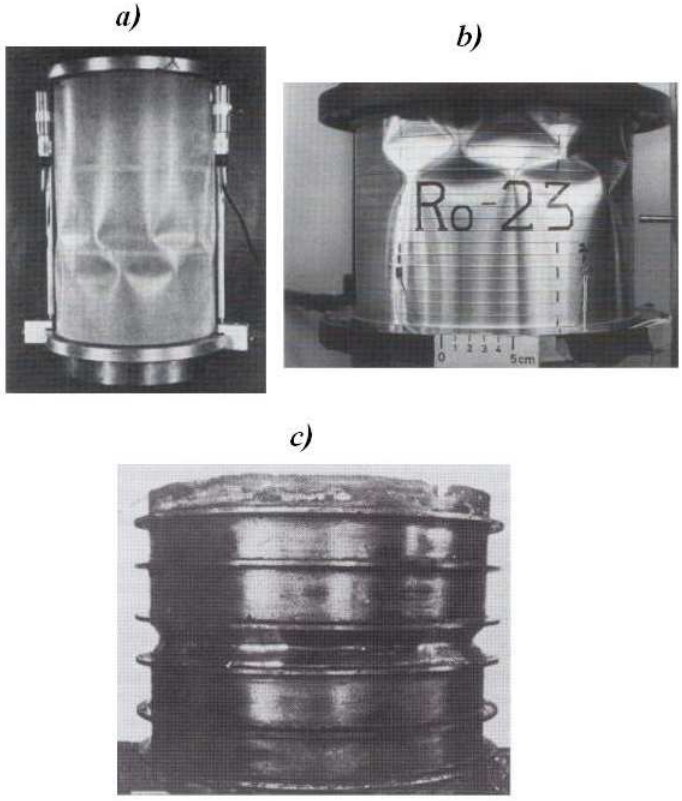

Fig. 2-5: Buckling cases for ring-stiffened shell (Singer, 2004).

In Fig. 2-5a, where the rings are widely spaced, local shell buckling occurs between rings. For closely spaced internal rings (Fig. 2-5b), non-axisymmetric buckling occurs and global instability takes place. By contrast, outside rings (Fig. 2-5c) provide higher buckling strength by forcing an axisymmetric mode of collapse (Singer, 2004). The position of the ring outside or inside the shell is important.

Rings are the most effective stiffeners for shells under external pressure. Figure 2-6 explores the influence of the ring area, A, on the buckling load (Singer *et al.*, 1966), where $P_{uns.eq.}$ is the buckling load for an unstiffened shell with equivalent thickness of the same weight, e_2 is the ring eccentricity to the centre of the shell wall to be taken positive if the ring is inside and negative if the ring is outside, h is the wall thickness and a is the distance between rings.

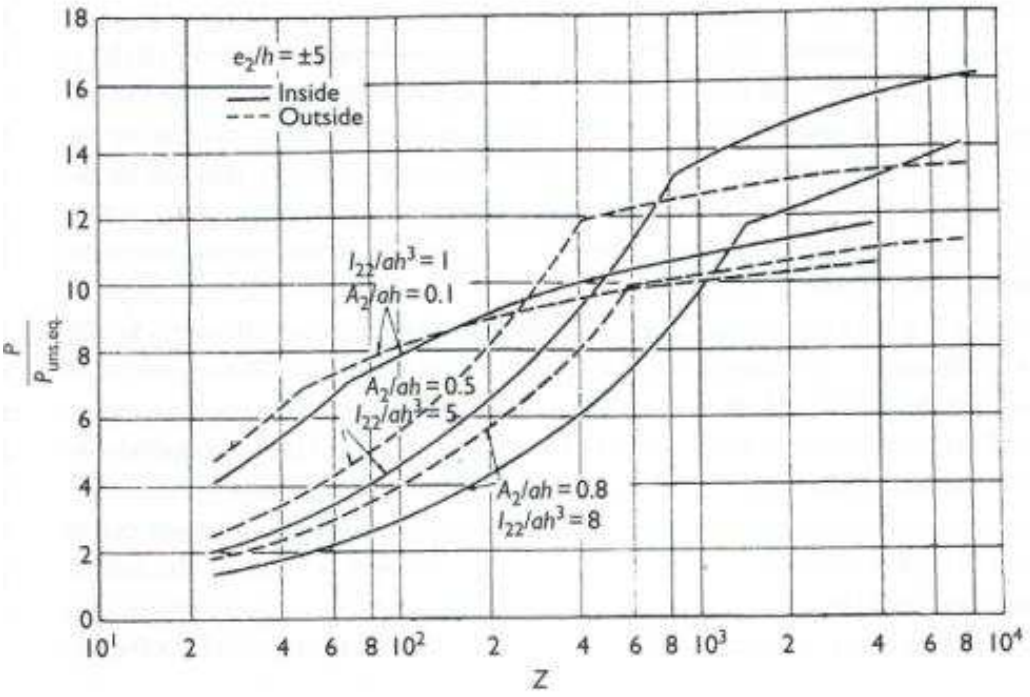

Fig. 2-6: Influence of ring area on the buckling strength for shell under hydrostatic pressure (Singer *et al.*, 1966).

In short shells when Z (Eq. 2-2) is small, the smallest rings are the best, but a heavy ring, $A_2/ah=0.8$, gives a higher buckling load for large Z. It appears that an optimum area ratio can be obtained there. Singer *et al.* (1966) divided the effect of the eccentricity of rings into two effects: a primary one where outside rings raise the bending stiffness in the circumferential direction more than inside rings (necessary for short cylinders) and a secondary effect where inside rings enhance the

extensional stiffness in the circumferential direction more than outside rings (for long cylinders).

Stringers (longitudinal stiffeners) both increase the axial and bending strength. Therefore, they are much more effective than rings for axial compression (Singer *et al.*, 1967). Cylinders with closely spaced stringers fail by global instability (Fig. 2-7a). When the stringers are widely spaced, local buckling occurs between stringers (Fig. 2-7b).

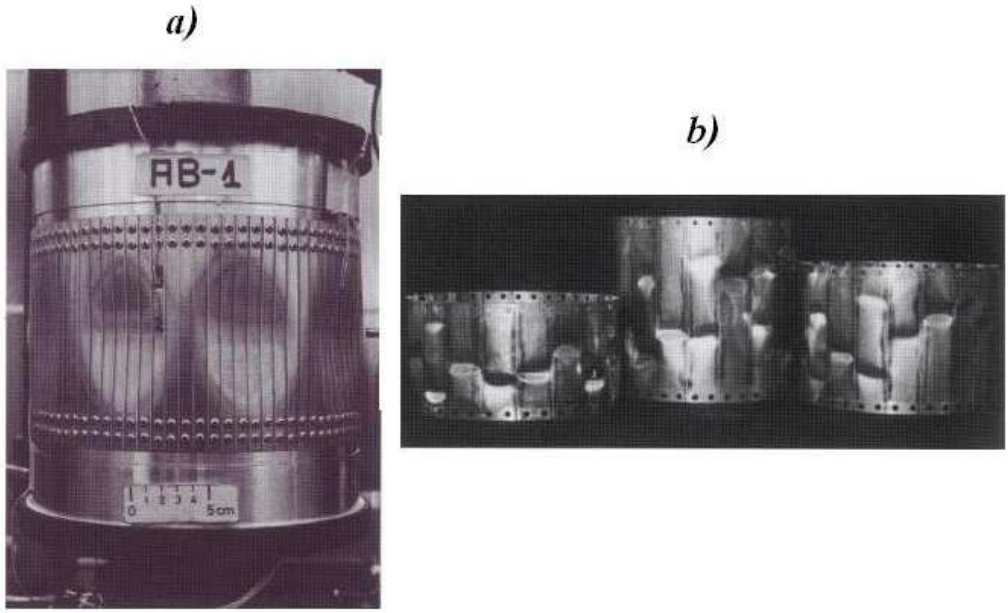

Fig. 2-7: Buckling forms for a stringer-stiffened cylindrical shell (Singer, 2004).

The position of stringers was discussed by Singer *et al.*, (1967) showing that outside stringers provide higher buckling loads than inside stringers when the shell is short. Moreover, a clamped base is much better in this range (Fig. 2-8). The buckling strength decreases rapidly for cylindrical shells of large Z. However, the curves in Fig. 2-8 are calculated using linear buckling theory to obtain the buckling loads, and the experiments on stiffened shells exhibit higher strengths than are shown in this figure (Singer *et al.*, 1967). In general, the studies of Singer and his co-authors show that all practical outside stringer-stiffened shells give higher buckling loads than inside ones.

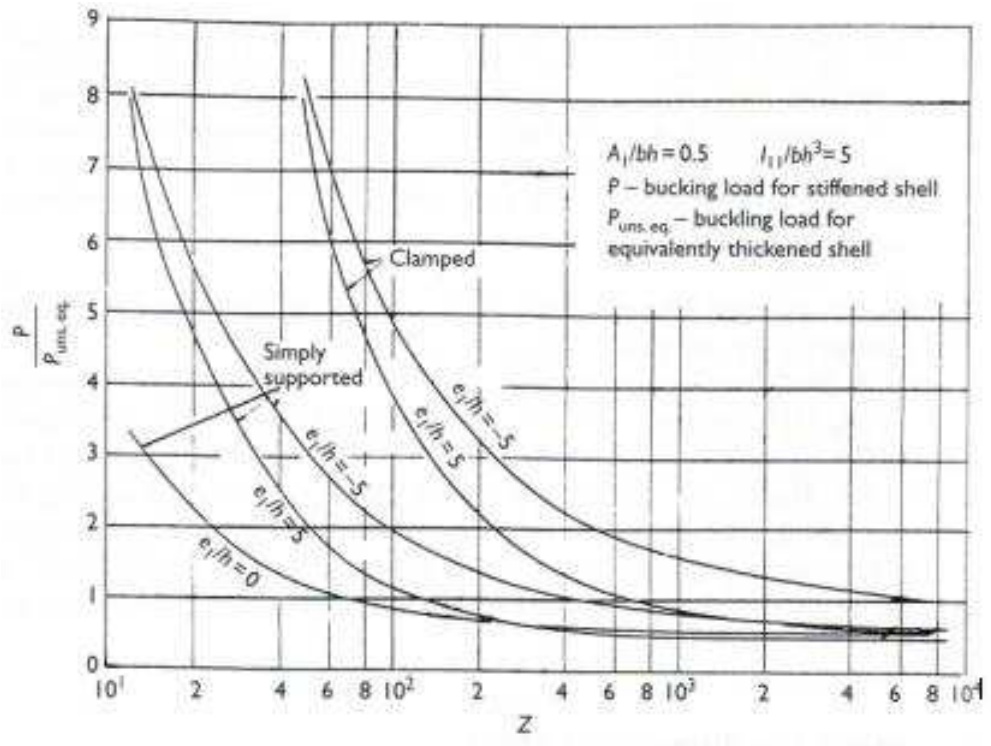

Fig. 2-8: Buckling load of stringer-stiffened cylindrical shells under axial compression (Singer *etal.*, 1967)

2.3.1 End rings

It is worth mentioning that the upper end ring may have a good influence on the buckling resistance. Rotter (1985a) indicated that the top ring has a strong influence on the axial stress when applied pressures vary slowly around the circumference (e.g. eccentric filling, wind, etc.). Greiner and Guggenberger (2004) strongly recommended using a strong upper end-ring for thin walled cylindrical shells under wind loads. It was found that it is not only necessary to take the wind load over the upper half of the shell, but also to avoid global buckling in the postbuckling range.

2.3.2 Using a ring to strengthen a cylinder locally

Under high internal pressure accompanied by axial forces, Chen *et al.*, (2005, 2006) proposed that using a small ring stiffener is very effective in preventing elastic-plastic failure by elephant's foot buckling in cylindrical shells. Based on the

linear elastic bending theory (Rotter, 1985b), the optimal dimensions and location for this stiffener were derived. It was seen that a ring that is either a larger ring or a smaller than the optimal size may reduce the buckling strength. The same effect can be seen in Fig. 2-6 (Singer, 1966) when the cylinder is long (large Z). In addition, Greiner (2004) showed that, for a practical stepped wall cylinder under uniform external pressure, a very small ring can raise the buckling resistance by about 50% compared with an unstiffened shell. Further, Chen *et al.*, (2005, 2006) showed that the location of this ring should be chosen carefully. Otherwise, early elephant's foot buckling may occur.

2.4 FRP composites to strengthen structures

Fibre Reinforced Polymer (FRP) composites have been used widely in construction for the last 30 years. Examples of FRP applications on buildings are presented in many references (e.g. Cripps, 2002). FRP is composed of fibres combined together by an appropriate resin which also plays a very significant role in protecting the fibres from environmental effects. The most suitable fibres for strengthening applications are shown in Table 2-2 where typical values of their properties are given.

Table 2-2: Typical dry fibres properties (Concrete Society, 2004; Cadei *et al.*, 2004)

Fibre	Tensile strength (MPa)	Modulus of elasticity (GPa)	Strain to failure (%)	Density (t/m3)	Coefficient of thermal expansion (10^{-6}/C)
Carbon: High strength	4300-4900	230-240	1.9-2.1	1.8	-0.38
Carbon: High modulus	2740-5490	294-329	0.7-1.9	1.78-1.81	-0.83
Carbon: Ultra high modulus	2600-4020	540-640	0.4-0.8	1.91-2.12	-1.1
Aramid: High strength and high modulus	3200-3600	124-130	2.4	1.44	2.1
Glass	2400-3500	70-85	3.5-4.7	2.6	4.9

Table 2-2 shows that fibres with higher stiffness (elastic modulus) tend to have smaller strength and failure strain.

Typical properties of different resins are shown in Table 2-3. Epoxies are generally in use more than other resins because of both the high strength and high failure strain. These advantages make epoxies more efficient in problems where the bond is very important, as in the case of flexural and shear strengthening of beams (Teng *et al.,* 2002). Further, epoxies have excellent environmental and chemical resistance, high performance, low shrinkage and strong adhesion.

The advantages of using FRP (Section 1.2) were a huge motivation for many researchers to conduct extensive studies since the 1990s to strengthen concrete members (columns, beams and slabs). As a result, several guidelines have been produced dealing with the design of externally FRP-strengthened concrete structures such as those of Cripps (2002), Teng *et al.,* (2002), Technical Report No. 55 of the Concrete Society (2004), BD 84/02 of the Highways Agency (2002), etc.

Table 2-3: Typical dry fibres properties (Cadei *et al.,* 2004)

Resin	Tensile strength (MPa)	Modulus of elasticity (GPa)	Strain to failure (%)	Density (t/m3)	Poisson's ratio	Coefficient of thermal expansion (10^{-6}/C)
Epoxy	60-85	2.6-3.8	1.5-8	1.11-1.2	0.3-0.4	30-70
Polyester	50-75	3.1-4.6	1-2.5	1.11-1.25	0.35-0.38	30-70
Phenolic	60-80	3-4	1-1.8	1-1.25	Not available	80
Polyurethane	15-25	0.5	10	1.15-1.2	0.4	40

Strengthening concrete columns using FRP was studied extensively. Circular column (Seible *et al.,* 1997; Teng and Lam, 2004; Chaallal *et al.,* 2006; Teng *et al.,* 2007), elliptical column (Teng *et al.,* 2002; Wang and Wu, 2008) and rectangular columns (Mirmiran *et al.,* 1997; Teng *et al.,* 2002) were examined.

Using FRP to strengthen the flexural strength of a reinforced concrete member was undertaken early by many researchers. Concrete beams (Chen and Teng, 2001; Smith and Teng, 2002; Teng *et al.,* 2002; Thomsen *et al.,* 2004; Toutanji *et al.,* 2007) and slabs (Teng *et al.,* 2000, 2001; Ebead and Marzouk, 2004; Enochsson *et al.,* 2007) were investigated.

The research on strengthening concrete structures has been extended to the strengthening of masonry (Triantafillou, 1998; Chen, 2002) and timber structures (Triantafillou, 1997; Gilfillan *et al*., 2003).

Strengthening metallic members using FRP has been the subject of a limited amount of research. However, some effort has begun to compensate for this (e.g. Cadei *et al.*, 2004). Metallic beams have been the main concern recently (Photiou *et al.*, 2006; Stratford and Cadei, 2006). Photiou *et al.* (2006) explained that the type of FRP fibres must be chosen carefully. The high modulus fibres, Table 2-2, produced beams that displayed a ductile behaviour and higher flexural strength, whereas using ultra high modulus fibres caused the beam to fail early by FRP rupture. The reason is that the ultra high modulus fibres have a low ultimate strain (Table 2-2). Furthermore, the final strength of the metallic beam depends completely on the effectiveness of the adhesive. An elastic analysis study of the stresses in the adhesive was conducted by Stratford and Cadei (2006). A high peel stress with a high shear stress occurs at the end of the FRP strengthening plate. Changing the plate end geometry and defect sensitivity were discussed by Stratford and Cadei (2006). Methods of reducing the stress concentration at the end of an FRP plate are shown in Fig. 2-9. Furthermore, by reducing the thickness of the FRP, while increasing its width, the stresses in the adhesive can be decreased (Cadei *et al.*, 2004; Stratford and Cadei, 2006).

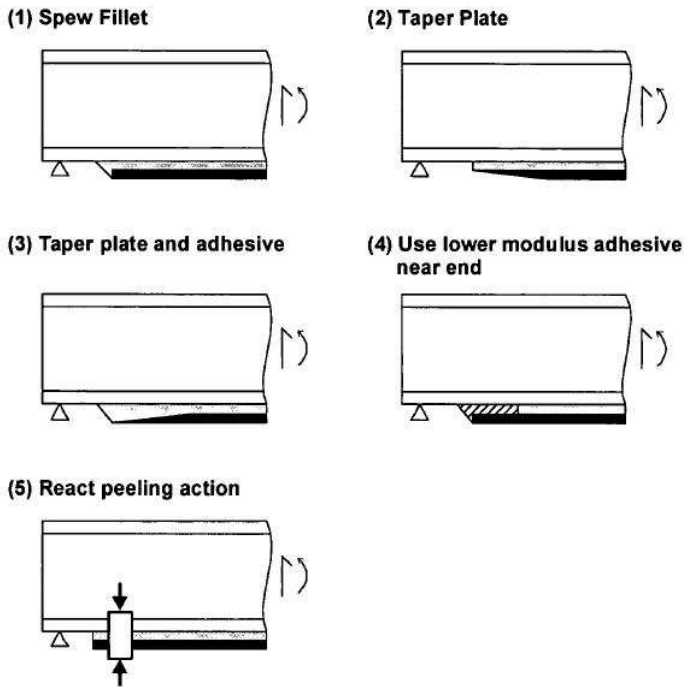

Fig. 2-9: Methods of reducing the stress concentration at the end of an FRP plate (Cadei *etal*., 2004).

2.5 FRP strengthening of a metallic cylindrical shell

It was shown in Section 2.4 that much research has been conducted to explore using FRP to strengthen structures made from different materials, but in all these cases, strength rather than stability is the main concern. Teng and Hu (2004, 2007) have recently studied the possibility of using FRP against elephant's foot elastic-plastic buckling. Their study was on thick circular tubes under axial loading alone. It was shown in both experiments and FE analysis that the outward buckling mode near the end, known as elephant's foot buckling, was prevented. Instead, inward buckling failure away from the ends was obtained together with high axial load capacity by increasing the thickness of FRP laminates. Further, the ductility was greatly improved even with a small amount of FRP confinement. In addition, an initial study of thin cylindrical shells under axial load accompanied with internal pressure was conducted by Teng and Hu (2007). Again, FRP confinement provided an effective technique to prevent the local collapse by elephant's foot buckling.

Strengthening a thin cylindrical shell against elephant's foot buckling by using FRP has been extended (Batikha *et al.*, 2007a, b) in this thesis and its supporting

papers. A linear elastic study (Batikha *et al.,* 2007a) and a Geometrically and Materially Nonlinear Analysis study (Batikha *et al.,* 2007b) showed that a small amount of FRP, placed at the critical location, can effectively eliminate elephant's foot buckling. In addition, elastic collapse of a thin cylindrical shell with an axisymmetric imperfection and a local dent were discussed in Batikha *et al. (*2007c, 2008) respectively. These last two studies have shown that the strength of the cylindrical shell can be effectively enhanced by bonding an external FRP locally within the area of the imperfection zone.

2.6 Summary

In this chapter, the buckling of a thin cylindrical shell was reviewed with typical methods of strengthening against stability failure. In addition, the new technique of repairing structures using FRP was explored. Examples of using FRP to strengthen concrete, masonry, timber and metallic members were provided. In all these cases, the effectiveness of the FRP on the element strength was described. Also, the study referred to the lack of research into the use of FRP to enhance the stability of thin metal cylindrical shells. It can be seen that this study is valuable in discovering the gain in buckling strength that a thin cylindrical shell can obtain under different conditions.

Chapter 3

Mechanical Properties of FRP composites

3.1 Introduction

In this chapter, the mechanical properties of FRP composites are described. This is vital background that must be understood before attempting to compute when an FRP laminate may be useful. The area of concern in this chapter is FRP with uniaxially aligned continues fibres.

This chapter begins with a description of the properties for one ply FRP with uniaxial direction fibres. Secondly, the effect of the orientation of the fibres on the mechanical properties of FRP ply is discussed. Finally, the properties of FRP sheet consisting of many layers acting together are described.

3.2 Mechanical properties of FRP lamina

Fibre reinforce polymer, FRP, is formed from the fibres, denoted herby the subscript *f*, and the resin known as the matrix, detonated by *m*. The arrangement of the fibres into the FRP must be known in order to specify the mechanical properties of FRP. Figure 3-1 shows the range of common fibre arrangements, although some of these classes are not commonly used in practice (e.g. random fibres in three dimensions) (McCrum *et al.*, 1997). However, uniaxial fibres are the main focus of this chapter (Fig. 3-2).

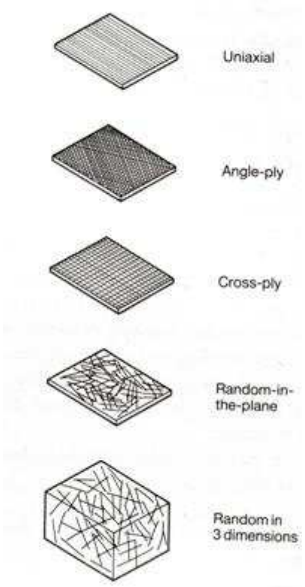

Fig. 3-1: Patterns of fibre arrangements (McCrum *et al.*, 1997).

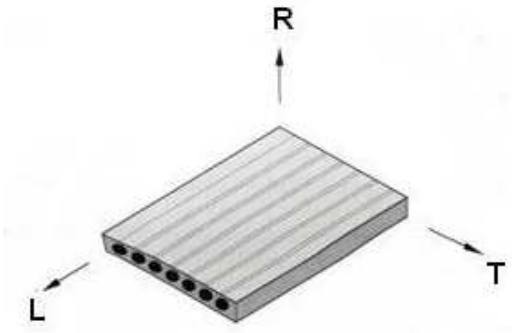

Fig. 3-2: The definition of axis for uniaxial fibre arrangements (Åström, 1997)

The uniaxial FRP lamina is considered as an orthotropic material in a planar stress state where the differences between the properties of the fibres and the matrix produce different engineering constants which are needed to model the material behaviour.

The fibre spacing in the matrix can significantly influence the mechanical properties of the FRP sheet, whether it is from a single isolated fibre or full contact fibres in the matrix. Vinson and Sierakowski (1986) indicated that FRP plates generally approach the behaviour of single fibres in practical situations. It should be noted that most references derive the mechanical properties of an FRP lamina by assuming the situation of isolated fibres (e.g. Åström, 1997; McCrum *et al.*, 1997).

In this section, four elastic constants for the lamina are presented using the simplified empirical-formulas developed by Vinson and Sierakowski (1986). The reason for chosen their model is that their approach includes the effects of the fibre packing geometry and loading conditions. It is important to mention here that the presented equations all assume that both the fibre and the matrix are homogeneous and isotropic, whereas the lamina is homogenous and orthotropic.

The moduli (E_L, E_T and G_{LT}) and Poisson's ratio ν_{LT} of the lamina are given by Eqs 3-1, 3-2, 3-3 and 3-4 respectively.

$$E_L = E_f V_f + E_m V_m \tag{3-1}$$

$$\frac{E_T}{E_m} = \frac{1+\xi\eta V_f}{1-\eta V_f} \tag{3-2}$$

$$\frac{G_{LT}}{G_m} = \frac{1+\xi\eta V_f}{1-\eta V_f} \tag{3-3}$$

$$\nu_{LT} = \nu_f V_f + \nu_m V_m \tag{3-4}$$

in which:

E_L, E_T are the elastic moduli of the FRP lamina in the fibre direction and the transverse direction respectively (Fig. 3-2).

G_{LT}, ν_{LT} are the in-plane shear modulus and Poisson's ratio respectively.

E_f and ν_f are the Young's modulus and Poisson's ratio for the fibre respectively.

E_m, G_m and ν_m are the Young's modulus, shear modulus and Poisson's ratio for the matrix.

The factor ξ represents taking the effect of the fibre packing geometry and loading conditions into account. For instance, $\xi=2$ is used for the calculation of E_T, while a value of $\xi=1$ is considered for G_{LT} (Ashton *et al.*, 1969 as reviewed in Vinson and Sierakowski, 1986).

The factor η is given as:

$$\eta = \frac{E_f / E_m - 1}{E_f / E_m + \xi} \tag{3-5}$$

in which:

V_f is the fibre volume friction and V_m is the matrix volume fraction, $V_m=1-V_f$.

Figure 3-3 illustrates the relationship between the unit weight, W_f, and volume, V_f, for five different common fibres (Table 3.1) (Åström, 1997).

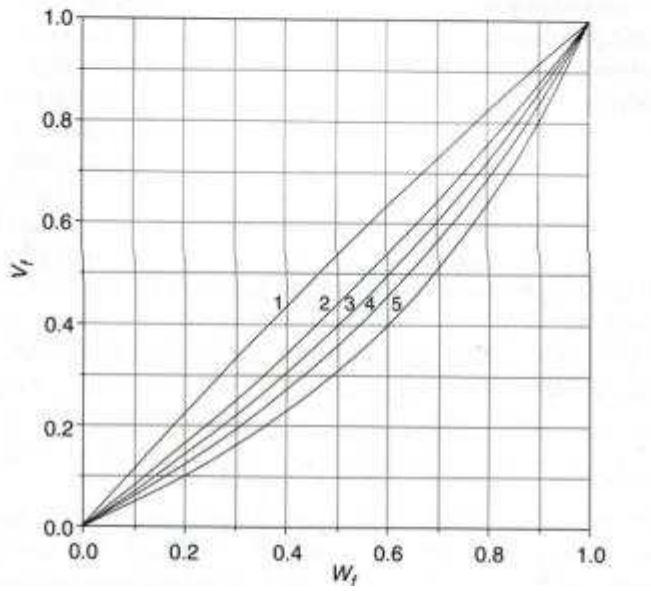

Fig. 3-3: The relationships between weight and volume for five density ratios listed in Table 3-1 (Åström, 1997).

Table 3-1: Density ratios for the curve number used in Fig.3-3 (Åström, 1997)

Curve number	Fibre to matrix density ratio (ρ_f/ρ_m)	Possible reinforcement type	Reinforcement density (Kg/m^3)
1	0.88	PE (Polyethylene)	970
2	1.31	Aramid	1440
3	1.55	Carbon (Low-density)	1700
4	1.82	Carbon (high-density)	2000
5	2.27	Glass	2500

In addition, the fiber percentage by weight, W_f, was shown in Teng *et al*. (2002) for three types of common FRP fibres: GFRP, CFRP and AFRP (Table 3-2).

Table 3-2: Fibre content by weight (%) (Teng *et al*., 2002)

Unidirectional composite material	Fibre content by weight (W_f) %
Carbon fibre/Polyester GFRP laminate	50-80
Carbon/Epoxy CFRP laminate	65-75
Aramid/Epoxy AFRP laminate	60-70

3.3 The effect of the orientation of the fibres

The fibres in the FRP lamina may be oriented in a direction which is not parallel to the geometric axis of the beam, plate or shell (Fig. 3-4). For these situations, new properties need to be obtained for an FRP lamina in the system coordinates (z and θ in Fig. 3-4).

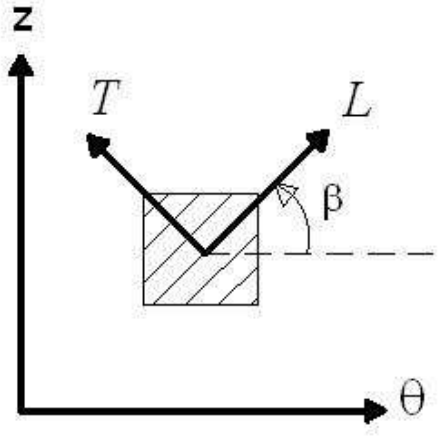

Fig. 3-4: Lamina coordinate systems.

The stresses and relative strains in the two coordinate systems shown in Fig. 3-4 can be expressed as given in Eq. 3-6, (Vinson and Sierakowski, 1986; Zienkiewicz, 1971).

$$\begin{Bmatrix} \sigma_L \\ \sigma_T \\ \tau_{LT} \end{Bmatrix} = [T] \begin{Bmatrix} \sigma_\theta \\ \sigma_z \\ \tau_{\theta z} \end{Bmatrix} \text{ and } \begin{Bmatrix} \varepsilon_L \\ \varepsilon_T \\ \gamma_{LT} \end{Bmatrix} = [T] \begin{Bmatrix} \varepsilon_\theta \\ \varepsilon_z \\ \gamma_{\theta z} \end{Bmatrix} \tag{3-6}$$

where [T] is an appropriate transformation matrix given in Eq. 3-7:

$$[T] = \begin{bmatrix} \cos^2\beta & \sin^2\beta & 2\cos\beta\sin\beta \\ \sin^2\beta & \cos^2\beta & -2\cos\beta\sin\beta \\ -\cos\beta\sin\beta & \cos\beta\sin\beta & \cos^2\beta - \sin^2\beta \end{bmatrix} \tag{3-7}$$

The relationship between stress and strain for an FRP lamina in terms of the principal material direction *(L, T)* is shown in Eq. 3-8:

$$\begin{Bmatrix}\sigma_L\\ \sigma_T\\ \tau_{LT}\end{Bmatrix}=\begin{bmatrix}Q_{LL} & Q_{LT} & 0\\ & Q_{TT} & 0\\ (Sym) & & 2Q_{SS}\end{bmatrix}\begin{Bmatrix}\varepsilon_L\\ \varepsilon_T\\ \gamma_{LT}\end{Bmatrix} \tag{3-8}$$

in which the components of the stiffness matrix, [*Q*], are defined in Eq. 3-9:

$$Q_{LL}=\frac{E_{LL}}{(1-\nu_{LT}\nu_{TL})}\,,\ Q_{TT}=\frac{E_{TT}}{(1-\nu_{LT}\nu_{TL})}$$

$$Q_{LT}=\frac{\nu_{TL}E_{LL}}{(1-\nu_{LT}\nu_{TL})}\ \text{and}\ Q_{SS}=G_{LT} \tag{3-9}$$

The relationship between ν_{ij} and ν_{ji} for an orthotropic material is:

$$\frac{\nu_{ij}}{\nu_{ji}}=\frac{E_{ii}}{E_{jj}} \tag{3-10}$$

From Eqs 3-6 and 3-8, the results to the *(θ, z)* coordinate system (Fig. 3-4) can then be expressed as:

$$\begin{Bmatrix}\sigma_\theta\\ \sigma_z\\ \tau_{\theta z}\end{Bmatrix}=[\overline{Q}]\ \begin{Bmatrix}\varepsilon_\theta\\ \varepsilon_z\\ \gamma_{\theta z}\end{Bmatrix} \tag{3-11}$$

where:

$$[\overline{Q}]=[T]^{-1}[Q]\ [T]=\begin{bmatrix}\overline{Q}_{11} & \overline{Q}_{12} & 2\overline{Q}_{13}\\ \overline{Q}_{21} & \overline{Q}_{22} & 2\overline{Q}_{23}\\ \overline{Q}_{13} & \overline{Q}_{23} & 2\overline{Q}_{33}\end{bmatrix} \tag{3-12}$$

The above relationships were described by Vinson and Sierakowski (1986)

3.4 The mechanical properties of layered FRP composites

The elastic constants for an orthotropic layered shell (Fig. 3-5) have been presented in many references (e.g. Baker *et al.*, 1986).

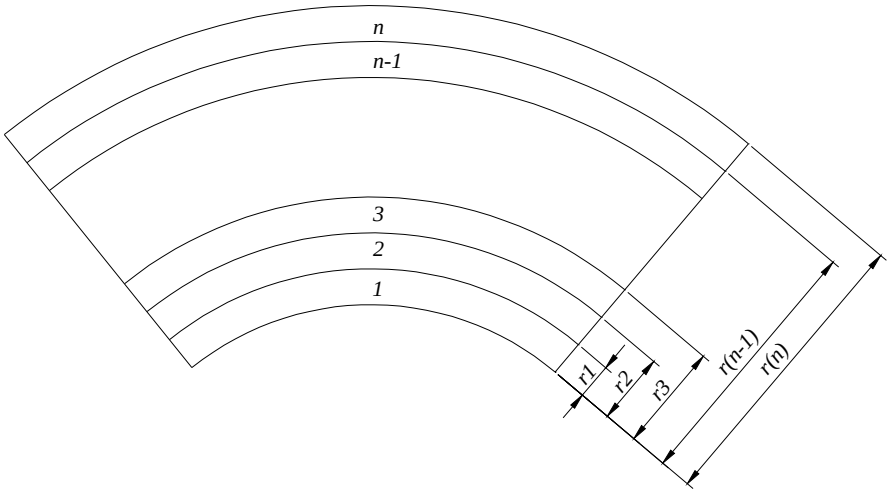

Fig. 3-5: Layered shell

The relationship between the increments of stress resultant (membrane forces *N* and bending/twisting moments *M*) and generalized strain (strain or change of curvature) is linear (Geier and Singh, 1997; Geier *et al.*, 2002):

$$\{N\} = [A]\ \{\varepsilon\} + [B]\ \{\kappa\}\ , \{M\} = [B]^T \{\varepsilon\} + [D]\ \{\kappa\} \tag{3-13}$$

in which:

$\{\kappa\}$ is the change of curvature vector.

$\{\varepsilon\}$ is the extensional strain vector.

[A], *[B]* and *[D]* are the in-plane stiffness matrix, the extension-bending coupling matrix and the bending stiffness matrix respectively, given as follows for a laminate of *n* layers (Fig. 3-5):

$$A_{ij} = \sum_{k=1}^{n} (\overline{Q_{ij}})_k (r_k - r_{k-1})\ ,\ [A] = \begin{bmatrix} A_{11} & A_{12} & A_{13} \\ & A_{22} & A_{23} \\ (Sym) & & A_{33} \end{bmatrix}$$

$$B_{ij} = \frac{1}{2} \sum_{k=1}^{n} (\overline{Q_{ij}})_k (r_k^2 - r_{k-1}^2)\ ,\ [B] = \begin{bmatrix} B_{11} & B_{12} & B_{13} \\ & B_{22} & B_{23} \\ (Sym) & & B_{33} \end{bmatrix} \text{ and} \tag{3-14}$$

$$D_{ij} = \frac{1}{3}\sum_{k=1}^{n}(\overline{Q_{ij}})_k (r_k^3 - r_{k-1}^3), [D] = \begin{bmatrix} D_{11} & D_{12} & D_{13} \\ & D_{22} & D_{23} \\ (Sym) & & D_{33} \end{bmatrix}$$

where $\overline{Q_{ij}}$ can be obtained from Eq.(3-12).

The modified bending stiffness matrix, $[\tilde{D}]$, can then be written as (Geier and Singh, 1997; Geier *et al.*, 2002):

$$[\tilde{D}] = [D] - [B]^T [A]^{-1} [B] = \begin{bmatrix} \tilde{D}_{11} & \tilde{D}_{12} & \tilde{D}_{13} \\ & \tilde{D}_{22} & \tilde{D}_{23} \\ (Sym) & & \tilde{D}_{33} \end{bmatrix} \tag{3-15}$$

$[\tilde{D}]$ is unchangeable matrix with the respect to the position of reference surface of the laminate.

The elastic constants for a layered shell are given as follows (Baker *et al.*, 1986):

$$\begin{aligned} &B_\theta = A_{11},\ B_z = A_{22},\ C_{\theta z} = A_{33}, \\ &D_\theta = \tilde{D}_{11}, D_z = \tilde{D}_{22},\ D_{\theta z} = \tilde{D}_{12}, \\ &\mu_\theta = \frac{\tilde{D}_{12}}{\tilde{D}_{22}}, \mu_z = \frac{\tilde{D}_{12}}{\tilde{D}_{11}}, \\ &\mu_\theta' = \frac{A_{12}}{A_{22}} \text{ and } \mu_z' = \frac{A_{12}}{A_{11}} \end{aligned} \tag{3-16}$$

in which:

B_θ, B_z are the extensional stiffnesses of a layered shell in θ and z directions respectively.

$C_{\theta z}$ is the shear stiffness of a layered shell in the (θ, z) plane.

D_θ, D_z are the bending stiffnesses of a layered shell in θ and z directions respectively.

$D_{\theta z}$ is the twisting stiffness of a layered shell.

μ_θ, μ_z are the Poisson's ratios associated with bending in θ and z directions respectively.

μ'_{θ}, μ'_{z} are the Poisson's ratios associated with extension in θ and z directions respectively.

Chapter 4

FRP preventing radial displacements in pressurized cylinders, Linear elastic Analysis (LA)

4.1 Introduction

In this chapter, FRP composites are applied to the external surface of a cylindrical shell under internal pressure accompanied by an axial load. Linear elastic shell Analysis (LA in the terminology of EN 1993-1-6, 2007) is used to investigate the effectiveness of this application of FRP to decrease the lateral displacement of a pressurised cylinder.

This chapter is divided into two parts:

First, a Linear elastic Analysis (LA) study is described in which the general equations governing the behaviour of an FRP-strengthened cylindrical shell under internal pressure accompanied by axial force are derived for different boundary conditions.

Second, the effectiveness of the external FRP in reducing the radial deformation of both pinned-base cylinder and fixed-base cylinders is explored. In addition, both the optimal dimensions and the critical location of an FRP sheet are obtained to prevent a peak from occurring in the radial displacement.

At the end of this chapter, a summary is given of the results established from this linear elastic study.

4.2 Stress resultants in a cylindrical shell strengthened with an FRP sheet

4.2.1 Geometry, boundary conditions, loading and material properties

A cylindrical shell of height h, radius r, and thickness t_s is strengthened by bonding FRP sheets to its exterior. The wall thickness of the cylindrical shell is assumed to be constant over the whole structure. The Young's modulus and the Poisson's ratio of the shell are E_s and ν_s respectively.

The boundary condition at the bottom is first considered as simply supported (radial, axial and circumferential displacements are restrained, but not the rotation) in the following analysis, but a fixed support is also considered later. The top boundary of the shell is assumed to be far away, so that the details of the boundary condition are not important.

An FRP sheet with a height of h_f and thickness of t_f is bonded to the external surface of the cylindrical shell, starting at a distance x_f above the base. The FRP sheet is treated as orthotropic with Young's modulus in the circumferential direction $E_{f\theta}$ and in the meridional direction E_{fz}, with a Poisson's ratio $\nu_{f\theta}$. It is assumed that the FRP sheet consists of uniaxial fibres in the circumferential direction.

A uniform internal pressure p and an axial load per unit circumference N_z at the top boundary are applied to the shell, as shown in Fig. 4-1. If the structure is a silo, the vertical loads arise from the frictional drag of the stored material against the wall. The internal pressure in the cylinder is assumed to be constant with the axial coordinate, since the buckling mode is generally very localized (Rotter and Zhang 1990).

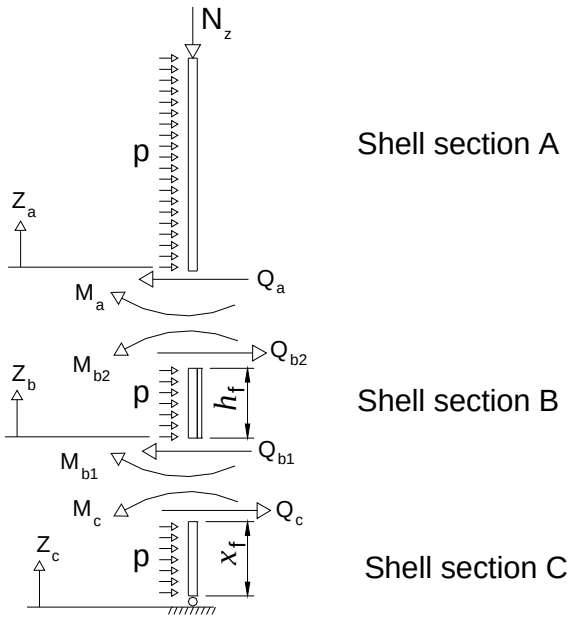

Fig. 4-1: Coordinate systems and stress resultants between different sections of the shell.

4.2.2 General shell equations

For a cylindrical shell of uniform thickness *t*, the radial displacement *w* under a uniform internal pressure *p* and a vertical load per unit circumference N_z is governed by Eq. 4-1, (Rotter, 1985b):

$$D\frac{d^4w}{dz^4}+\frac{Et}{r^2}w=p+\frac{\nu N_z}{r} \tag{4-1}$$

in which *D* is the shell flexural rigidity given by:

$$D=\frac{Et^3}{12(1-\nu^2)} \tag{4-2}$$

If an FRP sheet is attached to the outside surface of the shell, as in Section B, when the metal shell expands under the internal pressure and vertical loading, the FRP sheet will induce a confining pressure p_f on the metal shell, as shown in Fig. 4-2.

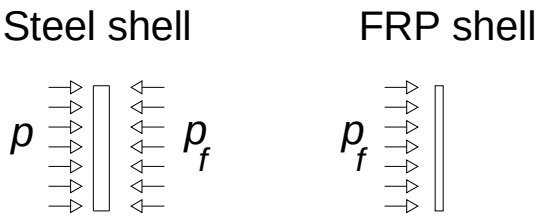

Fig. 4-2: Interaction pressure between the FRP and the metal shells within Section B.

The governing equation for the metal shell in Section B is then given by:

$$D_s \frac{d^4 w}{dz^4} + \frac{E_s t_s}{r^2} w = p - p_f + \frac{\nu_s N_{Zs}}{r} \tag{4-3}$$

and that for the FRP sheet is:

$$D_{fz} \frac{d^4 w}{dz^4} + \frac{E_{f\theta} t_f}{r^2} w = p_f + \frac{\nu_{fz} N_{Zf}}{r} \tag{4-4}$$

In Eqs 4-3 and 4-4, D_s and D_{fz} are the flexural rigidity of the metal and FRP shells respectively. They can be obtained by substituting the appropriate properties (elastic modulus and the Poisson's ratio) in the z direction and the thickness into Eq. 4-2.

Eliminating p_f from Eqs 4-3 and 4-4 gives:

$$(D_s + D_{fz}) \frac{d^4 w}{dz^4} + \frac{E_s t_s + E_{f\theta} t_f}{r^2} w = p + \left(\nu_s \frac{N_{zs}}{N_z} + \nu_{fz} \frac{N_{zf}}{N_z} \right) \frac{N_z}{r} \tag{4-5}$$

where N_{zs} is the axial force in the cylindrical metal shell in Section B, and N_{zf} is the value in the FRP shell.

By comparing Eq. 4-5 with Eq. 4-1, the differential equation for Section B can be written as follows:

$$D_b \frac{d^4 w}{dz^4} + \frac{E_b t_b}{r^2} w = p + \frac{\nu_b N_z}{r} \tag{4-6}$$

in which

$$D_b = D_s + D_{fz} \tag{4-7a}$$

$$E_b t_b = E_s t_s + E_{f\theta} t_f = E_s t_s (1 + \alpha) \tag{4-7b}$$

$$\nu_b = \nu_s \frac{N_{zs}}{N_z} + \nu_{fz} \frac{N_{zf}}{N_z} \tag{4-7c}$$

in which the extensional stiffness ratio of FRP to the steel shell is represented by:

$$\alpha = \frac{E_{f\theta} t_f}{E_s t_s} \tag{4-8}$$

Section B may be treated as an equivalent metal shell. The effective thickness t_b of the converted Section B may be derived by equating the ratio of the flexural to the extensional stiffness of the equivalent shell to that of the metal-FRP composite shell as:

$$\frac{D_b}{E_b t_b} = \frac{\frac{E_b t_b^3}{12(1-\nu_b^2)}}{E_b t_b} \tag{4-9}$$

Substituting Eqs 4-7a and 4-7b into the left hand side of Eq. 4-9 and rearranging the resulting equation gives:

$$t_b = \sqrt{\frac{12 D_b}{B_\theta}} \tag{4-10}$$

where B_θ is the extensional stiffness in circumferential direction for Section B:

$$B_\theta = \frac{E_b t_b}{1-\nu_b{}^2} = \frac{E_s t_s (1+\alpha)}{1-\nu_b{}^2} \tag{4-11}$$

The same expression for t_b can also be found in Baker *et al.* (1986) for an equivalent homogeneous isotropic cylinder, having the same stiffness properties as the composite orthotropic cylinder.

If the FRP fibres are applied in the circumferential direction, then Young's modulus of FRP in the meridional direction is very small compared with that in the circumferential direction and that of the metal shell. In addition, it is anticipated that only thin FRP sheets would be required to achieve the strengthening purpose. Therefore, both the flexural and extensional rigidities of the FRP in the meridional direction would be much smaller than those of the metal shell and can be neglected (Teng and Hu, 2004, 2007). In such a case, Eq. 4-5 may be rewritten by ignoring the terms relating to the meridional direction properties of FRP:

$$D_s \frac{d^4 w}{dz^4} + \frac{E_s t_s (1+\alpha)}{r^2} w = p + \nu_s \frac{N_z}{r} \tag{4-12}$$

Similarly, the properties for an equivalent metal shell for Section B can be obtained from Eqs 4-7 and 4-10 as:

$$D_b = D_s = \frac{E_s t_s^3}{12(1-\nu_s^2)} \tag{4-13a}$$

$$\nu_b = \nu_s \tag{4-13b}$$

$$\text{and} \quad t_b = \sqrt{\frac{12(1-\nu_s^2)D_s}{E_s t_s (1+\alpha)}} \tag{4-13c}$$

4.2.3 General solution

The general solution of Eq. 4-1 (Rotter, 1985b) is:

$$w = \{[C_1 \cos\frac{\pi z}{\lambda} + C_2 \sin\frac{\pi z}{\lambda}]e^{-\pi z/\lambda} + [C_3 \cos\frac{\pi z}{\lambda} + C_4 \sin\frac{\pi z}{\lambda}]e^{\pi z/\lambda} + 1\} w_m \tag{4-14}$$

in which λ is the meridional bending half-wavelength given by Eq. 2-3 and w_m is the membrane theory normal deflection:

$$w_m = (p + \frac{\nu_s N_z}{r})\frac{r^2}{E_s t_s} \tag{4-15}$$

For Section B, the meridional bending half-wavelength, λ_b, and the membrane theory normal deflection, w_{mb}, can be obtained as follows:

$$\lambda_b = \frac{\pi}{\left[3\left(1-\nu_s{}^2\right)\right]^{1/4}}\sqrt{r t_b} \tag{4-16a}$$

$$w_{mb} = \left(p + \nu_s \frac{N_z}{r}\right)\frac{r^2}{E_s t_s (1+\alpha)} \tag{4-16b}$$

The stress resultants in the shell may be expressed in terms of displacements as:

$$N_\theta = \frac{Et}{R} w + \nu N_z \tag{4-17a}$$

$$M_z = -D\frac{d^2 w}{dz^2} \tag{4-17b}$$

$$M_\theta = \nu M_z \tag{4-17c}$$

$$Q_z = -D\frac{d^3 w}{dz^3} \tag{4-17d}$$

Shell Section A

It is assumed that Section A of the metal cylindrical shell is long, so that the upper end boundary condition is not important. Writing:

$$\overline{x_a} = \frac{\pi z_a}{\lambda} = \frac{\pi(z - x_f - h_f)}{\lambda} \tag{4-18}$$

and from Eq. 4-14:

$$w = \left[\left(C_{a1}\cos\overline{x_a} + C_{a2}\sin\overline{x_a}\right)e^{-\overline{x_a}} + 1\right]w_m \tag{4-19a}$$

differentiation gives the meridional slope, curvature and third derivative as:

$$\beta = \frac{dw}{dz_a} = w_m \cdot \frac{\pi}{\lambda}\left[\begin{matrix} -C_{a1}(\sin\overline{x_a} + \cos\overline{x_a}) \\ +C_{a2}(\cos\overline{x_a} - \sin\overline{x_a}) \end{matrix}\right]e^{-\overline{x_a}} \tag{4-19b}$$

$$\frac{d^2 w}{dz_a^2} = 2w_m\left(\frac{\pi}{\lambda}\right)^2\left[C_{a1}\sin\overline{x_a} - C_{a2}\cos\overline{x_a}\right]e^{-\overline{x_a}} \tag{4-19c}$$

$$\frac{d^3 w}{dz_a^3} = 2w_m\left(\frac{\pi}{\lambda}\right)^3\left[C_{a1}(-\sin\overline{x_a} + \cos\overline{x_a}) + C_{a2}(\cos\overline{x_a} + \sin\overline{x_a})\right]e^{-\overline{x_a}} \tag{4-19d}$$

The deformation and internal forces at the junction between the shell Sections A and B (z_a=0 in Fig. 4-1) can be found from Eqs 4-17 and 4-19.

$$w_a = (C_{a1} + 1)w_m \tag{4-20a}$$

$$\beta_a = w_m\frac{\pi}{\lambda}[-C_{a1} + C_{a2}] \tag{4-20b}$$

$$M_a = 2D_s w_m\left(\frac{\pi}{\lambda}\right)^2 C_{a2} \tag{4-20c}$$

$$Q_a = -2D_s w_m\left(\frac{\pi}{\lambda}\right)^3\left[C_{a1} + C_{a2}\right] \tag{4-20d}$$

Shell Section B

Section B is a composite shell with different properties, as described earlier. It must be treated as a short shell since its two ends may be relatively close to each other.

$$\overline{x_b} = \frac{\pi z_b}{\lambda_b} = \frac{(z - x_f)}{\lambda_b} \tag{4-21}$$

From Eq. 4-14, the deformations in Section B are

$$w = \begin{bmatrix} \left(C_{b1}\cos\overline{x_b} + C_{b2}\sin\overline{x_b}\right)e^{-\overline{x_b}} \\ + \left(C_{b3}\cos\overline{x_b} + C_{b4}\sin\overline{x_b}\right)e^{\overline{x_b}} + 1 \end{bmatrix} w_{mb} \tag{4-22a}$$

$$\begin{aligned} \beta &= \frac{dw}{dz_b} \\ &= w_{mb}.\frac{\pi}{\lambda_b}\{[-C_{b1}(\sin\overline{x_b} + \cos\overline{x_b}) + C_{b2}(\cos\overline{x_b} - \sin\overline{x_b})]e^{-\overline{x_b}} \\ &+ [C_{b3}(-\sin\overline{x_b} + \cos\overline{x_b}) + C_{b4}(\cos\overline{x_b} + \sin\overline{x_b})]e^{\overline{x_b}}\} \end{aligned} \tag{4-22b}$$

$$\frac{d^2 w}{dz_b^2} = 2 w_{mb} \left(\frac{\pi}{\lambda_b}\right)^2 \begin{Bmatrix} [C_{b1}\sin\overline{x_b} - C_{b2}\cos\overline{x_b}]e^{-\overline{x_b}} \\ + [-C_{b3}\sin\overline{x_b} + C_{b4}\cos\overline{x_b}]e^{\overline{x_b}} \end{Bmatrix} \tag{4-22c}$$

$$\begin{aligned} \frac{d^3 w}{dz_b^3} = 2w_{mb}\left(\frac{\pi}{\lambda_b}\right)^3 \{&[C_{b1}(-\sin\overline{x_b} + \cos\overline{x_b}) \\ &+ C_{b2}(\cos\overline{x_b} + \sin\overline{x_b})]e^{-\overline{x_b}} \\ &+ [-C_{b3}(\sin\overline{x_b} + \cos\overline{x_b}) + C_{b4}(\cos\overline{x_b} - \sin\overline{x_b})]e^{\overline{x_b}}\} \end{aligned} \tag{4-22d}$$

The deformations and internal forces at z_b=0 can be found from Eqs 4-17 and 4-22:

$$w_{b1} = [C_{b1} + C_{b3} + 1]w_{mb} \tag{4-23a}$$

$$\beta_{b1} = w_{mb}.\frac{\pi}{\lambda_b}\ [-C_{b1} + C_{b2} + C_{b3} + C_{b4}] \tag{4-23b}$$

$$M_{b1} = -2D_b.w_{mb}.\left(\frac{\pi}{\lambda_b}\right)^2[-C_{b2} + C_{b4}] \tag{4-23c}$$

$$Q_{b1} = -2.D_b.w_{mb}.\left(\frac{\pi}{\lambda_b}\right)^3[C_{b1} + C_{b2} - C_{b3} + C_{b4}] \tag{4-23d}$$

Similarly, those at z_b=h_f are:

$$\begin{aligned} w_{b2} = &\{[C_{b1}\cos\varpi_b + C_{b2}\sin\varpi_b]e^{-\varpi_b} \\ &+ [C_{b3}\cos\varpi_b + C_{b4}\sin\varpi_b]e^{\varpi_b} + 1\}w_{mb} \end{aligned} \tag{4-24a}$$

$$\beta_{b2} = w_{mb}\frac{\pi}{\lambda_b}\{[-C_{b1}(\sin\varpi_b + \cos\varpi_b) + C_{b2}(\cos\varpi_b - \sin\varpi_b)]e^{-\varpi_b} + [C_{b3}(-\sin\varpi_b + \cos\varpi_b) + C_{b4}(\cos\varpi_b + \sin\varpi_b)]e^{\varpi_b}\} \quad (4\text{-}24b)$$

$$M_{b2} = -2D_b w_{mb}(\frac{\pi}{\lambda_b})^2\{[C_{b1}\sin\varpi_b - C_{b2}\cos\varpi_b]e^{-\varpi_b} + [-C_{b3}\sin\varpi_b + C_{b4}\cos\varpi_b]e^{\varpi_b}\} \quad (4\text{-}24c)$$

$$Q_{b2} = -2D_b w_{mb}(\frac{\pi}{\lambda_b})^3\{[C_{b1}(-\sin\varpi_b + \cos\varpi_b) + C_{b2}(\cos\varpi_b + \sin\varpi_b)]e^{-\varpi_b} + [-C_{b3}(\sin\varpi_b + \cos\varpi_b) + C_{b4}(\cos\varpi_b - \sin\varpi_b)]e^{\varpi_b}\} \quad (4\text{-}24d)$$

where, $\varpi_b = \frac{\pi h_f}{\lambda_b}$ (4-24e)

Shell Section C

Section C must also be treated as a short shell because its two boundaries may be close to each other. Writing

$$\overline{x_c} = \frac{\pi z_c}{\lambda} = \frac{\pi z}{\lambda} \quad (4\text{-}25)$$

The deformations in Section C can be obtained from Eq. 4-14 as:

$$w = \{[C_{c1}\cos\overline{x_c} + C_{c2}\sin\overline{x_c}]e^{-\overline{x_c}} + [C_{c3}\cos\overline{x_c} + C_{c4}\sin\overline{x_c}]e^{\overline{x_c}} + 1\}w_m \quad (4\text{-}26a)$$

$$\beta = \frac{dw}{dz_c} = w_m\frac{\pi}{\lambda}\{[-C_{c1}(\sin\overline{x_c} + \cos\overline{x_c}) + C_{c2}(\cos\overline{x_c} - \sin\overline{x_c})]e^{-\overline{x_c}} + [C_{c3}(-\sin\overline{x_c} + \cos\overline{x_c}) + C_{c4}(\cos\overline{x_c} + \sin\overline{x_c})]e^{\overline{x_c}}\} \quad (4\text{-}26b)$$

$$\frac{d^2w}{dz_c^2} = 2w_m(\frac{\pi}{\lambda})^2\{[C_{c1}\sin\overline{xc} - C_{c2}\cos\overline{x_c}]e^{-\overline{x_c}} + [-C_{c3}\sin\overline{x_c} + C_{c4}\cos\overline{x_c}]e^{\overline{x_c}}\} \quad (4\text{-}26c)$$

$$\frac{d^3w}{dz_c^3} = 2w_m(\frac{\pi}{\lambda})^3\{[C_{c1}(-\sin\overline{x_c} + \cos\overline{x_c}) + C_{c2}(\cos\overline{x_c} + \sin\overline{x_c})]e^{-\overline{x_c}} + [-C_{c3}(\sin\overline{x_c} + \cos\overline{x_c}) + C_{c4}(\cos\overline{x_c} - \sin\overline{x_c})]e^{\overline{x_c}}\} \quad (4\text{-}26d)$$

The deformations and internal forces at z_c=0 can be found from Eqs. 4-17 and 4-26:

$$w_{c0} = [C_{c1} + C_{c3} + 1]w_m \tag{4-27a}$$

$$\beta_{c0} = w_m \frac{\pi}{\lambda}[-C_{c1} + C_{c2} + C_{c3} + C_{c4}] \tag{4-27b}$$

$$M_{c0} = -2D_s w_m (\frac{\pi}{\lambda})^2 [-C_{c2} + C_{c4}] \tag{4-27c}$$

$$Q_{c0} = -2D_s w_m (\frac{\pi}{\lambda})^3 [C_{c1} + C_{c2} - C_{c3} + C_{c4}] \tag{4-27d}$$

Those at $z=x_f$ are:

$$\begin{aligned} w_c = &\{[C_{c1}\cos\varpi_c + C_{c2}\sin\varpi_c]e^{-\varpi_c} \\ &+ [C_{c3}\cos\varpi_c + C_{c4}\sin\varpi_c]e^{\varpi_c} + 1\}w_m \end{aligned} \tag{4-28a}$$

$$\begin{aligned} \beta_c = w_m \frac{\pi}{\lambda}\{&[-C_{c1}(\sin\varpi_c + \cos\varpi_c) + C_{c2}(\cos\varpi_c - \sin\varpi_c)]e^{-\varpi_c} \\ &+ [C_{c3}(-\sin\varpi_c + \cos\varpi_c) + C_{c4}(\cos\varpi_c + \sin\varpi_c)]e^{\varpi_c}\} \end{aligned} \tag{4-28b}$$

$$\begin{aligned} M_c = -2D_s w_m (\frac{\pi}{\lambda})^2 \{&[C_{c1}\sin\varpi_c - C_{c2}\cos\varpi_c]e^{-\varpi_c} \\ &+ [-C_{c3}\sin\varpi_c + C_{c4}\cos\varpi_c]e^{\varpi_c}\} \end{aligned} \tag{4-28c}$$

$$\begin{aligned} Q_c = -2D_s w_m (\frac{\pi}{\lambda})^3 \{&[C_{c1}(-\sin\varpi_c + \cos\varpi_c) \\ &+ C_{c2}(\cos\varpi_c + \sin\varpi_c)]e^{-\varpi_c} \\ &+ [-C_{c3}(\sin\varpi_c + \cos\varpi_c) + C_{c4}(\cos\varpi_c - \sin\varpi_c)]e^{\varpi_c}\} \end{aligned} \tag{4-28d}$$

where $\varpi_c = \frac{\pi x_f}{\lambda}$ (4-28e)

4.2.4 Compatibility and equilibrium between the shell segments

Boundary conditions at the base

The shell is first considered here to have a simply supported boundary at the base. The boundary conditions at the base can be expressed as:

$$w_{c0} = 0 \tag{4-29a}$$

$$M_{c0} = 0 \tag{4-29b}$$

Substituting Eqs 4-27 into 4-29 gives:

$$C_{c3} = -(C_{c1} + 1) \tag{4-30}$$

$$C_{c4} = C_{c2} \tag{4-31}$$

Continuity at Joint 1

The condition for deformation continuity at Joint 1 requires that

$$w_c = w_{b1} \tag{4-32a}$$

$$\beta_c = \beta_{b1} \tag{4-32b}$$

Substituting Eqs 4-28a and 4-28b into Eqs 4-23a and 4-23b respectively gives:

$$\begin{aligned} &C_{c1}(\cos\varpi_c e^{-\varpi_c}) + C_{c2}(\sin\varpi_c e^{-\varpi_c}) + C_{c3}(\cos\varpi_c e^{\varpi_c}) \\ &+ C_{c4}(\sin\varpi_c e^{\varpi_c}) - C_{b1}\frac{w_{mb}}{w_m} - C_{b3}\frac{w_{mb}}{w_m} + 1 - \frac{w_{mb}}{w_m} = 0 \end{aligned} \tag{4-33}$$

$$\begin{aligned} &C_{c1}[-(\sin\varpi_c + \cos\varpi_c)e^{-\varpi_c}] + C_{c2}[(\cos\varpi_c - \sin\varpi_c)e^{-\varpi_c}] \\ &+ C_{c3}[(-\sin\varpi_c + \cos\varpi_c)e^{\varpi_c}] \\ &+ C_{c4}[(\cos\varpi_c + \sin\varpi_c)e^{\varpi_c}] + C_{b1}.F_1 - C_{b2}.F_1 - C_{b3}.F_1 - C_{b4}.F_1 = 0 \end{aligned} \tag{4-34}$$

in which, $F_1 = \dfrac{w_{mb}}{w_m} \cdot \dfrac{\lambda}{\lambda_b}$ (4-35)

Equilibrium at Joint 1

Equilibrium at Joint 1 requires that:

$$M_c = M_{b1} \tag{4-36a}$$

$$Q_c = Q_{b1} \tag{4-36b}$$

Substituting Eqs 4-28c and 4-28d into Eqs 4-23c and 4-23d respectively gives:

$$\begin{aligned} &C_{c1}\sin\varpi_c e^{-\varpi_c} - C_{c2}\cos\varpi_c e^{-\varpi_c} - C_{c3}\sin\varpi_c e^{\varpi_c} + C_{c4}\cos\varpi_c e^{\varpi_c} \\ &+ C_{b2}F_2 - C_{b4}F_2 = 0 \end{aligned} \tag{4-37}$$

$$\begin{aligned} &C_{c1}[(-\sin\varpi_c + \cos\varpi_c)e^{-\varpi_c}] + C_{c2}[(\cos\varpi_c + \sin\varpi_c)e^{-\varpi_c}] \\ &+ C_{c3}[-(\sin\varpi_c + \cos\varpi_c)e^{\varpi_c}] \\ &+ C_{c4}[(\cos\varpi_c - \sin\varpi_c)e^{\varpi_c}] - F_3 C_{b1} - C_{b2}F_3 + C_{b3}F_3 - C_{b4}F_3 = 0 \end{aligned} \tag{4-38}$$

where, $F_2 = \dfrac{w_{mb}}{w_m}\dfrac{\lambda^2}{\lambda_b^2}\dfrac{D_b}{D}$ (4-39)

and, $F_3 = \frac{w_{mb}}{w_m}\frac{\lambda^3}{\lambda_b^3}\frac{D_b}{D}$ (4-40)

Continuity at Joint 2

Continuity at Joint 2 requires

$$w_a = w_{b2} \tag{4-41a}$$

$$\beta_a = \beta_{b2} \tag{4-41b}$$

Substituting Eqs 4-20a and 4-20b into Eqs 4-24a and 4-24b respectively gives:

$$\begin{aligned} &C_{b1}(\cos\varpi_b e^{-\varpi_b}) + C_{b2}(\sin\varpi_b e^{-\varpi_b}) + C_{b3}(\cos\varpi_b e^{\varpi_b}) \\ &+ C_{b4}(\sin\varpi_b e^{\varpi_b}) + C_{a1}(-\frac{w_m}{w_{mb}}) + 1 - \frac{w_m}{w_{mb}} = 0 \end{aligned} \tag{4-42}$$

$$\begin{aligned} &C_{b1}[-(\sin\varpi_b + \cos\varpi_b)e^{-\varpi_b}] + C_{b2}[(\cos\varpi_b - \sin\varpi_b)e^{-\varpi_b}] \\ &+ C_{b3}[(-\sin\varpi_b + \cos\varpi_b)e^{\varpi_b}] + C_{b4}[(\cos\varpi_b + \sin\varpi_b)e^{\varpi_b}] \\ &+ C_{a1}(\frac{1}{F_1}) + C_{a2}(-\frac{1}{F_1}) = 0 \end{aligned} \tag{4-43}$$

Equilibrium at Joint 2

The equilibrium at Joint 2 requires that

$$M_a = M_{b2} \tag{4-44a}$$

$$Q_a = Q_{b2} \tag{4-44b}$$

Substituting Eqs 4-20c and 4-20d into Eqs 4-24c and 4-24d respectively gives:

$$\begin{aligned} &C_{b1}(-\sin\varpi_b e^{-\varpi_b}) + C_{b2}(\cos\varpi_b e^{-\varpi_b}) + C_{b3}(\sin\varpi_b e^{\varpi_b}) \\ &+ C_{b4}(-\cos\varpi_b e^{\varpi_b}) + C_{a2}(-\frac{1}{F_2}) = 0 \end{aligned} \tag{4-45}$$

$$\begin{aligned} &C_{b1}[(-\sin\varpi_b + \cos\varpi_b)e^{-\varpi_b}] + C_{b2}[(\cos\varpi_b + \sin\varpi_b)e^{-\varpi_b}] \\ &+ C_{b3}[-(\sin\varpi_b + \cos\varpi_b)e^{\varpi_b}] + C_{b4}[(\cos\varpi_b - \sin\varpi_b)e^{\varpi_b}] \\ &+ C_{a1}(-\frac{1}{F_3}) + C_{a2}(-\frac{1}{F_3}) = 0 \end{aligned} \tag{4-46}$$

Substituting Eqs 4-30 and 4-31 into Eqs 4-33 to 4-46 and rearranging the resulting equations in matrix form gives

$$\begin{bmatrix} A_{11} & 0 & A_{13} & A_{14} & A_{15} & A_{16} & 0 & 0 \\ A_{21} & A_{22} & A_{23} & A_{24} & A_{25} & A_{26} & 0 & 0 \\ 0 & A_{32} & A_{33} & A_{34} & A_{35} & A_{36} & 0 & 0 \\ A_{41} & A_{42} & A_{43} & A_{44} & A_{45} & A_{46} & 0 & 0 \\ 0 & 0 & A_{53} & 0 & A_{55} & 0 & A_{57} & A_{58} \\ 0 & 0 & 0 & A_{64} & 0 & A_{66} & A_{67} & A_{68} \\ 0 & 0 & A_{73} & A_{74} & A_{75} & A_{76} & A_{77} & A_{78} \\ 0 & 0 & A_{83} & A_{84} & A_{85} & A_{86} & A_{87} & A_{88} \end{bmatrix} \times \begin{bmatrix} C_{a1} \\ C_{a2} \\ C_{b1} \\ C_{b2} \\ C_{b3} \\ C_{b4} \\ C_{c1} \\ C_{c2} \end{bmatrix} = \begin{bmatrix} B_1 \\ 0 \\ 0 \\ 0 \\ B_5 \\ B_6 \\ B_7 \\ B_8 \end{bmatrix} \tag{4-47}$$

which may be expressed as

$$[A]\{C\} = \{B\} \tag{4-48}$$

The coefficients A_{ij} and B_i in Eq. 4-47 are presented in Appendix I for pinned base. The coefficient vector {C} may be found as:

$$\{C\} = [A]^{-1} \times \{B\} \tag{4-49}$$

Note that coefficients C_{c3} and C_{c4} are not included in Eqs 4-47 and 4-49 but given in Eqs 4-30 and 4-31 respectively.

4.2.5 Radial displacement of the strengthened shell

Having obtained the coefficients from Eq. 4-49, the radial displacements of the strengthened shell can be calculated from:

$$w = \begin{cases} \{[C_{c1}\cos\overline{x_c} + C_{c2}\sin\overline{x_c}]e^{-\overline{x_c}} \\ +[C_{c3}\cos\overline{x_c} + C_{c4}\sin\overline{x_c}]e^{\overline{x_c}} + 1\}w_m & \text{for } 0 \le z < x_f \\ \{[C_{b1}\cos\overline{x_b} + C_{b2}\sin\overline{x_b}]e^{-\overline{x_b}} \\ +[C_{b3}\cos\overline{x_b} + C_{b4}\sin\overline{x_b}]e^{\overline{x_b}} + 1\}w_{mb} & \text{for } x_f \le z < x_f + h_f \\ \{[C_{a1}\cos\overline{x} + C_{a2}\sin\overline{x}]e^{-\overline{x_a}} + 1\}w_m & \text{for } h_f + x_f \le z \end{cases} \tag{4-50}$$

4.3 Patterns of deformation in the shell

The radial displacements and internal forces in the cylindrical shell, with an axisymmetrical FRP sheet of any size and bonded at any location, can be obtained from the above equations. An example cylindrical shell with a height h=5000mm, radius r=5000mm and thickness t_s=5mm was studied here. This shell has a radius to thickness ratio of 1000. Young's modulus E_s was taken as 200 GPa and Poisson's ratio ν_s as 0.3. An FRP sheet was bonded onto the shell starting at a height x_f above the base. The FRP sheet has a height h_f and thickness t_f. The elastic moduli $E_{f\theta}$, E_{fz}, in the circumferential and vertical directions, and the Poisson's ratio $\nu_{f\theta}$ were taken as 230GPa, 3GPa and 0.35 respectively. An internal pressure of 0.25 N/mm^2 and a vertical load of 500N/mm were applied. The effects of the FRP stiffness, height and position were explored.

Figure 4-3 shows the effect of the normalised FRP stiffness parameter α (Eq. 4-8) when $h_f/\lambda=1$ and the FRP starts from the base of the shell.

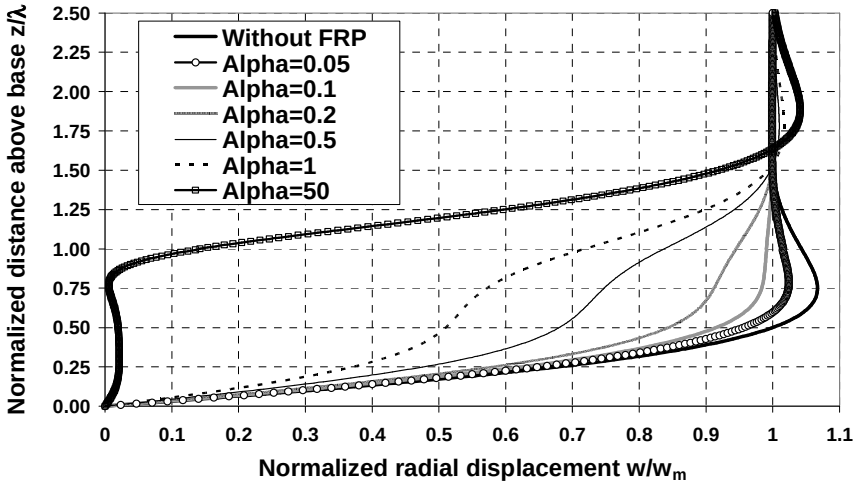

Fig. 4-3: Effect of FRP stiffness on shell deformation (h_f/λ = 1 and x_f/λ = 0).

When no FRP sheet is used, the maximum radial displacement occurs at a height of 0.75λ above the base, with the maximum deflection equal to 1.067w_m. A small amount of FRP (e.g. α=0.05) can reduce the maximum deflection but it cannot eliminate the peak. Whilst a larger amount of FRP (e.g. α=1) is used, the peak is eliminated within the region covered by the FRP, but it produces a new peak above

the FRP zone and the maximum deflection above the FRP zone increases as the amount of FRP increases. Using a very large FRP thickness (α=50) brings the deflection close to zero at the strip location and the maximum deflection occurs at another position above the FRP sheet. Clearly, using a large amount of FRP does not help in preventing the peak radial displacement from occurring. There is an optimal amount of FRP, with α being about 0.1, which can reduce the maximum deflection near the base to the membrane theory deflection, without introducing a peak elsewhere. This is taken here to be the optimum amount of FRP for strengthening purposes.

Figure 4-4 shows the effect of the normalized FRP height, h_f/λ, when the thickness and the starting position of FRP remains constant with α=0.1 and x_f/λ=0 respectively.

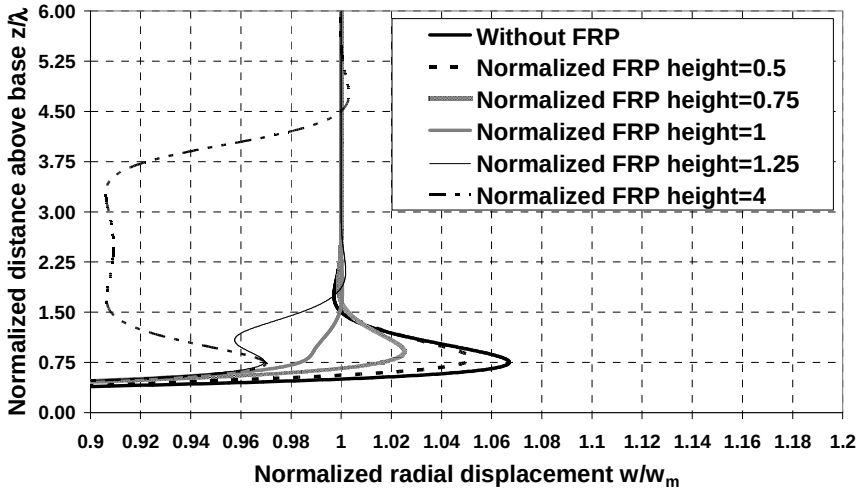

Fig. 4-4: Effect of normalized FRP height on the shell radial displacements (α = 0.1 and x_f/λ = 0).

When the FRP is attached only to a small section at the bottom of the shell (e.g. $h_f/\lambda=0.5$), the strengthening is not very effective as a large peak displacement remains above it. If the FRP height is increased, the peak deflection reduces. However, if the FRP height is too large, the cylinder starts to behave as a two-section shell with the lower section behaving as a metal-FRP composite shell and the upper as the original metal shell. The lower composite shell results in a peak at a distance of $0.75\lambda_b$ (λ_b given in Eq. 4-16a) from the base. A peak also appears above the position where the FRP ends, owing to bending arising from the discontinuity at the

end of the FRP. This reinforces the above observation that too much FRP may lead to larger deflection than those found for the optimal amount of FRP.

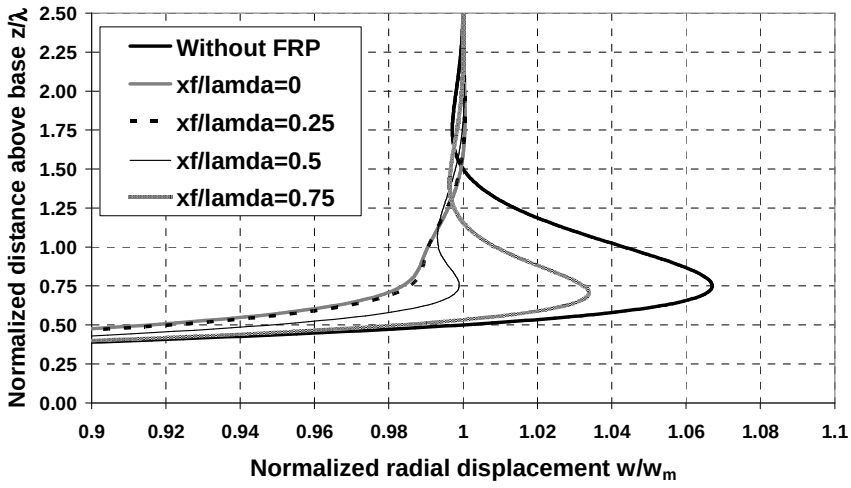

Fig. 4-5: Effect of FRP starting point on shell deformation (α = 0.1 and $(x_f+h_f)/\lambda$=1).

Figure 4-5 demonstrates the effect of the starting position of the FRP, x_f/λ, when both the thickness and the top end of the FRP remain constant, with α and $(x_f+h_f)/\lambda$ equal to 0.1 and 1.0 respectively. It appears that the maximum radial displacement is minimised when x_f/λ is about 0.5, in which case the FRP sheet centres at the height of 0.75λ above the base.

4.4 Optimal FRP strengthening to decrease the radial displacement

4.4.1 Estimation of optimal FRP strengthening

From Eq. 4-14 for a long cylindrical shell, it can be seen that the maximum value of the deflection w is located at $z=0.75\lambda$ when the cylindrical shell is not strengthened. The peak value of deflection is then $1.067w_m$, as shown in Fig. 4-5. In addition, it is clear that the dimensionless extensional rigidity of the FRP (α), the normalised height of the FRP sheet (h_f/λ) and its normalised starting position (x_f/λ) all affect the deformation of the strengthened shell. Figure 4-6 exhibits the effect of the normalized FRP height, h_f/λ, and the normalized start position, x_f/λ, on the

maximum displacement when α=0.1. It is seen that each curve has a minimum at which the position of the FRP is optimal.

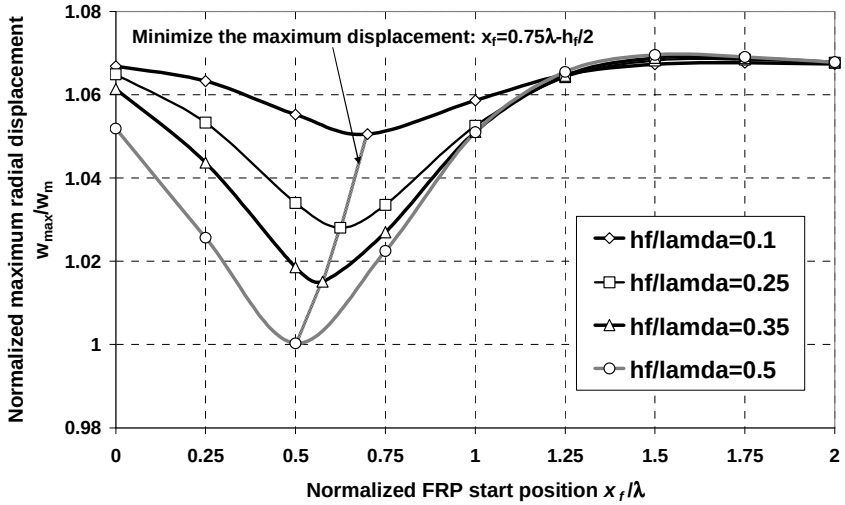

Fig. 4-6: The effect of h_f/λ and x_f/λ on the maximum radial displacement (α=0.1)

A close analysis shows that the minimum of the peak displacement is achieved if the FRP is centred at a distance of 0.75λ above the base, i.e.

$$x_f = 0.75\lambda - \frac{h_f}{2} \tag{4-51}$$

The deformation of the cylindrical shell strengthened with optimal FRP is expected to look like Fig. 4-7, which satisfies the boundary condition at the base, whilst the radial deformation is never greater than the membrane theory value anywhere in the shell.

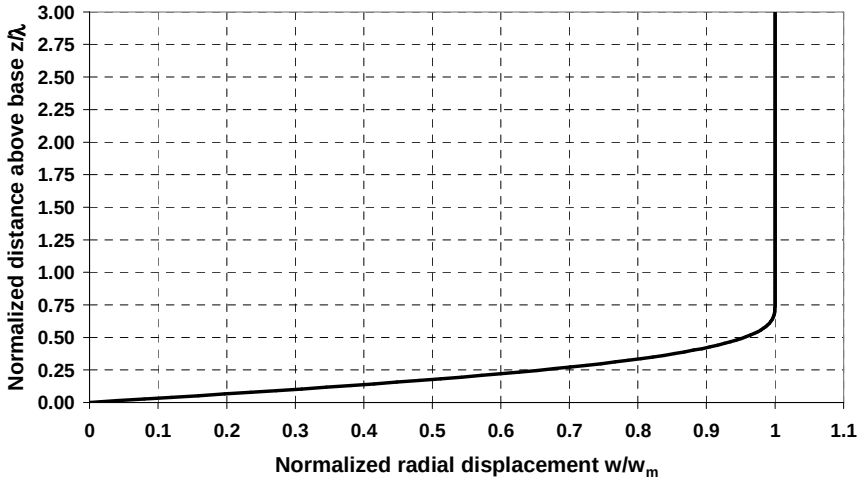

Fig. 4-7: The "ideal" deformation of a cylindrical shell strengthened with optimal FRP.

For the deformed shape of the shell, shown in Fig. 4-7, the radial displacement and the rotation at the joint between shell Sections A and B (Fig. 4-1) should be w_m and 0 respectively. This leads to the condition that $C_{a1}=C_{a2}=0$, according to Eqs 4-20a and 4-20b. Substituting C_{a1}=0 and C_{a2}=0 into Eqs 4-42 to 4-46 gives:

$$C_{b1} = \frac{\cos\varpi_b}{2} \times e^{\varpi_b} \times (\frac{w_m}{w_{mb}} - 1) \tag{4-52a}$$

$$C_{b2} = \frac{\sin\varpi_b}{2} \times e^{\varpi_b} \times (\frac{w_m}{w_{mb}} - 1) \tag{4-52b}$$

$$C_{b3} = \frac{\cos\varpi_b}{2} \times e^{-\varpi_b} \times (\frac{w_m}{w_{mb}} - 1) \tag{4-52c}$$

$$C_{b4} = \frac{\sin\varpi_b}{2} \times e^{-\varpi_b} \times (\frac{w_m}{w_{mb}} - 1) \tag{4-52d}$$

where ϖ_b is given in Eq. 4-24e.

It may be further assumed that the displacement, w, and rotation, β, at z=0.75λ above the base where the displacement peaks for the unstrengthened shell are equal to w_m and 0 respectively. From Eqs 4-26a and 4-26b, together with the boundary conditions at the base Eqs 4-30 and 4-31, give:

$$C_{c1} = [\sin 2\varpi - 1 - e^{2\varpi}]/[e^{2\varpi} - 2\sin 2\varpi - e^{-2\varpi})] \tag{4-53a}$$

$$C_{c2} = \frac{C_{c1}(e^{\varpi} - e^{-\varpi}) + e^{\varpi}}{\tan\varpi(e^{-\varpi} + e^{\varpi})} \tag{4-53b}$$

$$C_{c3} = -(C_{c1} + 1) \tag{4-53c}$$

$$C_{c4} = C_{c2} \tag{4-53d}$$

where ϖ=0.75π.

Substituting Eqs 4-52) and 4-53 into Eq. 4-37 results in:

$$\cos\varpi_c[C_{c1}(\tan\varpi_c e^{-\varpi_c}) + C_{c2}(-e^{-\varpi_c}) + C_{c3}(-\tan\varpi_c e^{\varpi_c}) + C_{c4}(e^{\varpi_c})] + F_2 \times \frac{\sin\varpi_b}{2}(\frac{w_m}{w_{mb}} - 1) \times (e^{\varpi_b} - e^{-\varpi_b}) = 0 \tag{4-54}$$

where F_2 is given in Eq. 4-39 and

$$\varpi_c = \frac{\pi x_f}{\lambda} = 0.75\pi - 0.5\varpi_b \frac{\lambda_b}{\lambda} \tag{4-55}$$

Substituting Eq. 4-55 into Eq. 4-54, the resulting transcendental equation contains only a single unknown ϖ_b. This equation can be solved for ϖ_b. From Eqs 4-24e and 4-55, x_f and h_f can be obtained as the optimal location for an FRP sheet, if the dimensionless stiffness α is pre-defined.

4.4.2 Worked example

The same cylindrical shell as that in Section 4.3 with the same properties for the both cylindrical shell and FRP sheet was studied here to verify the above procedure for estimating an optimal FRP strengthening scheme. The shell was assumed to be under an internal pressure of 0.25 N/mm^2 and vertical load of 500N/mm. For each dimensionless circumferential extensional rigidity value of the FRP, α, the above procedure can be used to estimate the optimal values of x_f and h_f. The results are shown in Figs 4-8 and 4-9.

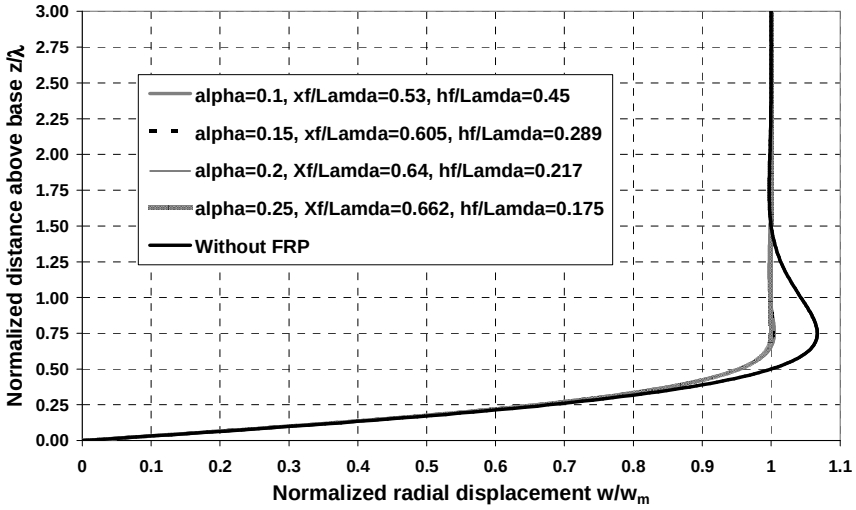

Fig. 4-8: Deformation of the example shell by strengthened with different stiffness FRP sheets located in optimal positions.

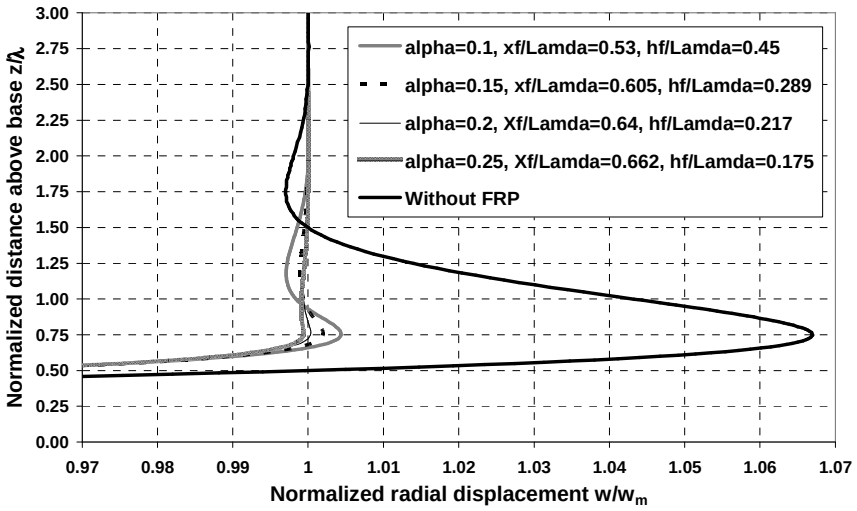

Fig. 4-9: Detailed deformation of the example shell strengthened with different stiffness FRP sheets located in optimal positions.

4.5 A cylindrical shell with a fixed base

4.5.1 Deformed shape

To study the effect of different boundary conditions, a fixed base was investigated. Compared with the shell with a pinned base, the only difference in this case is that the rotational boundary condition at the base becomes β_{c0}=0 at z=0. Applying this condition to Eq. 4-27b gives:

$$C_{c4} = 2C_{c1} - C_{c2} + 1 \tag{4-56}$$

From Eqs 4-30 and 4-32 to 4-46 and 4-56, the solution can be obtained in the same form as Eq. 4-47, but with different coefficients A_{ij} and B_i. These coefficients for a fixed base are given in Appendix II.

The same example as that in Section 4.3 but with a fixed base was studied here. Figure 4-10 shows the effect of the governing stiffness parameter α (Eq. 4-8) when a normalized FRP height h_f/λ is chosen as 1.0 and starting at the base (x_f/λ = 0).

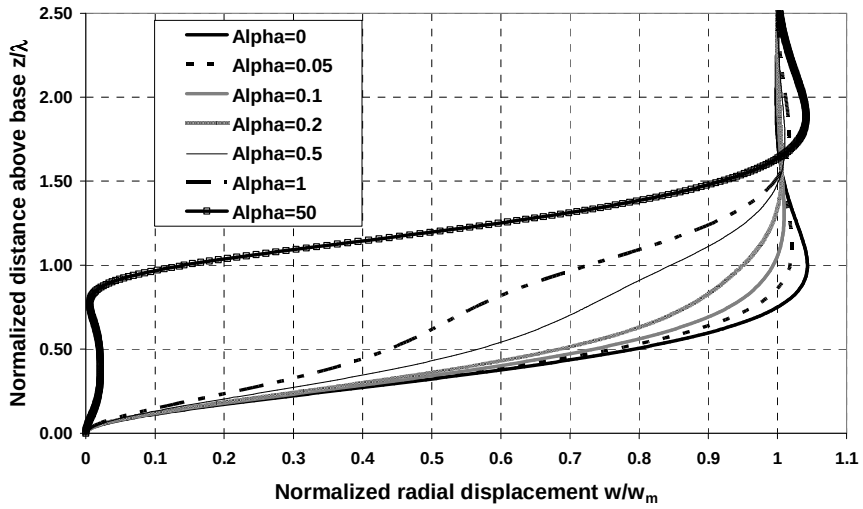

Fig. 4-10: Effect of FRP extensional rigidity α on the deformation of a shell with fixed base (h_f/λ=1 and x_f/λ = 0).

For the unstrengthened shell, the maximum radial displacement occurs at a height of λ (instead of 0.75λ for a cylindrical shell with pinned base) above the base with a value of 1.043w_m (c.f. 1.067w_m for a cylindrical shell with pinned base). The addition of a small amount of FRP can significantly reduce this peak value. The optimal value of α in this case is about 0.2 (e.f. $\alpha \cong 0.1$ for a cylinder with a pinned base). Again the use of a very large FRP stiffness (e.g. α=50) brings the deflection to zero in the strip location and produces a peak above the FRP. Figure 4-11 shows the effect of changing the normalized FRP height h_f/λ when α=0.1 and x_f/λ=0. It shows that an increase of normalized FRP height reduces the peak radial displacement initially, but a further increase introduces a peak above the FRP sheet which is less effective than the optimal case. Figure 4-12 demonstrates that changing the normalised starting position of FRP, x_f/λ, can significantly affect the shell deformation.

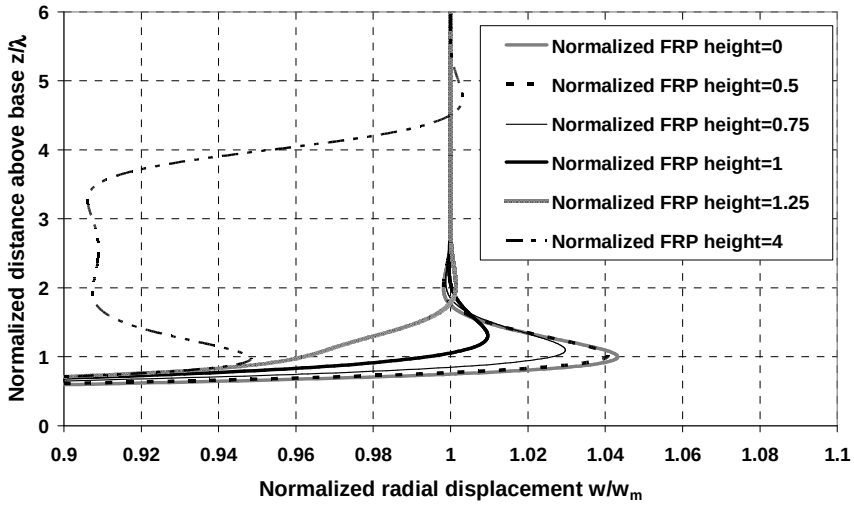

Fig. 4-11:Effect of normalized FRP height on fixed base shell radial displacements (α = 0.1 and x_f/λ = 0).

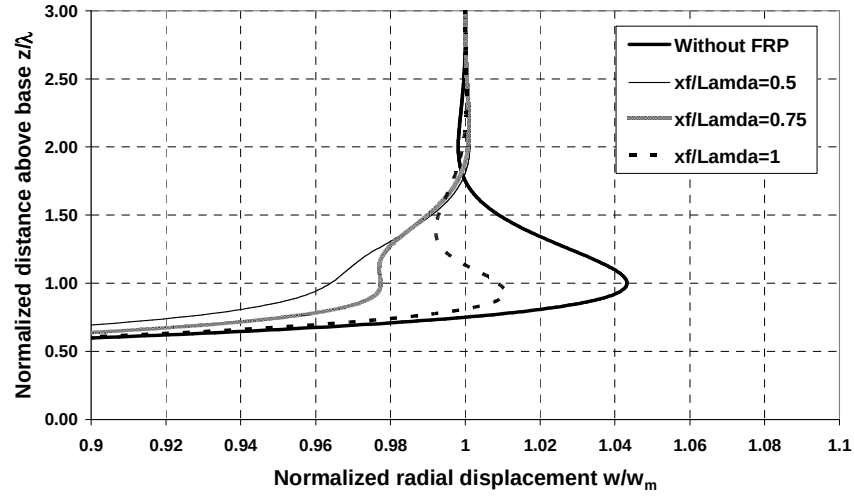

Fig. 4-12: Effect of FRP start position on fixed base shell deformation (α = 0.1 and $(x_f+h_f)/\lambda$ = 1.25).

4.5.2 Optimal FRP strengthening

As for the case of a shell with a pinned base, the parameters α, h_f/λ and x_f/λ affect the deformation of the strengthened shell. Figure 4-12 shows that the maximum value of the radial displacement w is located at $z=\lambda$ for an unstrengthened long cylindrical shell with a fixed base. The peak value of deflection is $1.043w_m$. Figure 4-13 shows the effects on the peak displacement of changing both the

normalized FRP height h_f/λ and the normalized start position x_f/λ. It is seen that the optimal position for the FRP sheet is that it is centred at z = λ. That is:

$$x_f = \lambda - \frac{h_f}{2} \tag{4-57}$$

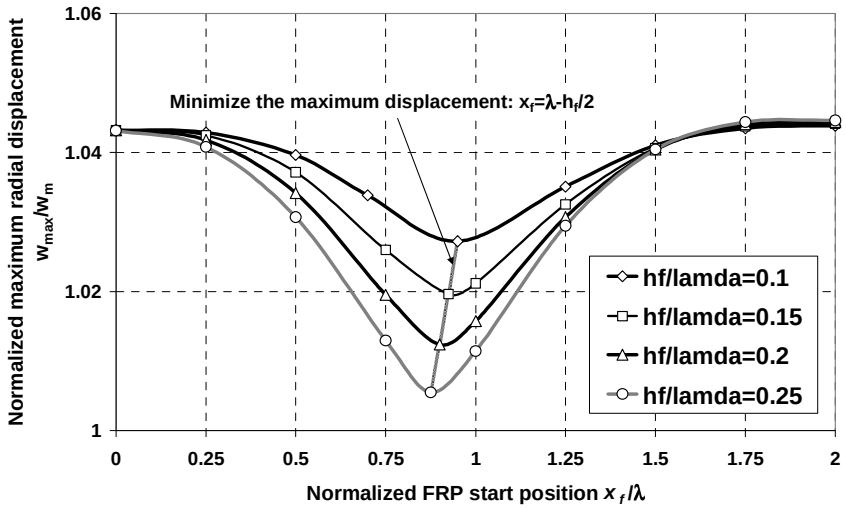

Fig. 4-13: The effect of h_f/λ and x_f/λ on the maximum radial displacement for fixed base cylindrical shell.

A similar procedure to that for a shell with a pinned base is developed here for estimating the optimal FRP parameters, assuming that the deformation of the strengthened shell with the optimal FRP is shown as in Fig. 4-14.

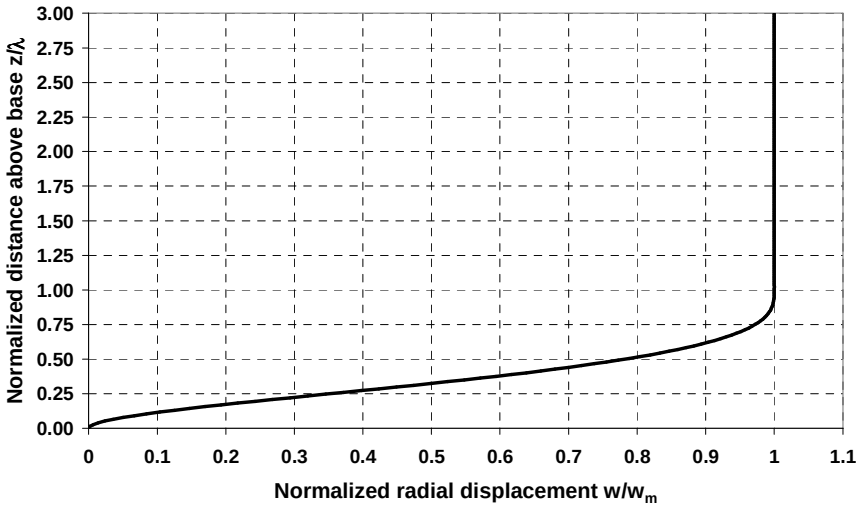

Fig. 4-14: The "ideal" deformation of a fixed base cylindrical shell strengthened with optimal FRP strengthening.

Applying $w=w_m$ and $\beta=0$ at the joint between shell Sections A and B gives the same Eqs 4-52. Further applying $w=w_m$ and $\beta=0$ to Eqs 4-26a and 4-26b respectively at z=λ, together with the boundary conditions Eqs 4-30 and 4-56 gives:

$$C_{c1} = -\frac{e^{\pi}}{(e^{\pi} - e^{-\pi})} = C_{c2} \tag{4-58a}$$

$$C_{c3} = -(1 + C_{c1}) \tag{4-58b}$$

$$C_{c4} = C_{c1} + 1 \tag{4-58c}$$

Substituting Eqs 4-58a to 4-58c into Eq. 4-54 and considering:

$$\varpi_c = \frac{\pi x_f}{\lambda} = \pi - 0.5\varpi_b \frac{\lambda_b}{\lambda} \tag{4-59}$$

the location of the optimal FRP sheet can be derived in the same way as for the pinned base from Eq. 4-54.

To verify the practical procedure, the worked example of Section 4.4.2 for the pinned base was studied again for a fixed base. Figure 4-15 shows the radial displacement after adding different stiffness of FRP sheet in the optimal location by using the equations of this study.

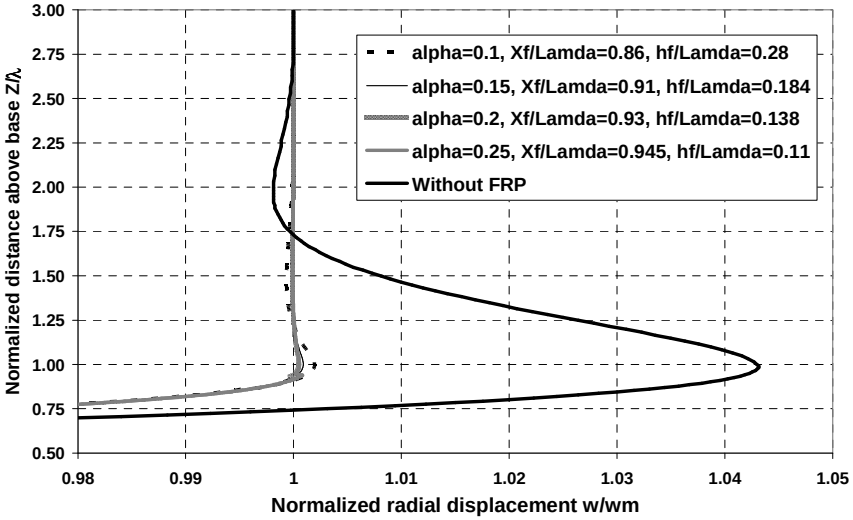

Fig. 4-15: Radial displacement for strengthened fixed base cylindrical shell by different FRP sheets.

From Fig. 4-15, it can be seen that the deflection of the shell decreased significantly by using this practical procedure. The radial displacement is very close to w_m at the centre of the FRP sheet, λ above the base, and satisfies the assumptions which were put for this practical procedure in Section 4.5.2.

4.6 Summary

This chapter has presented a preliminary study of the strengthening of a pressurized cylindrical shell using externally bonded FRP. The linear elastic equations for the strengthened cylindrical shell have been derived and illustrated through exploratory examples. Both pinned and fixed base boundary conditions for the cylindrical shell have been considered in this chapter. It has been shown that a small amount of FRP sheet, placed in the critical location, is optimal in reducing the peak radial deformation of the shell to the membrane theory value for the unstrengthened shell.

Chapter 5

Strengthening cylindrical shells against elephant's foot buckling using FRP

5.1 Introduction

The aim of this chapter is to investigate the application of FRP to increase the buckling strength of a thin metallic shell under high internal pressure accompanied with axial load. In this case an elastic-plastic stability failure, known as elephant's foot buckling, occurs. Geometrically and Materially Non linear Analysis (GMNA) is used to explore the influence of the attached FRP in producing higher buckling strengths.

This chapter begins with a description of elephant's foot buckling.

Then, a finite element analysis procedure using Geometrically and Materially Non linear Analysis (GMNA) is used to obtain the buckling strength.

Next, the effect of FRP strengthening on an axially compressed pressurized thin steel cylinder is demonstrated. Moreover, the optimal dimensions and quantities of FRP are found to eliminate elephant's foot buckling altogether.

Finally, a summary is presented of the important points shown in this chapter.

5.2 Elephant's foot buckling

Cylindrical shells are sensitive to the magnitude of the imperfections which can cause elastic buckling. However, it was shown by Rotter (1997) that for cylinders with weld depression imperfection, the failure mode in unpressurized cylinders is either elastic or elastic-plastic depending entirely on the radius to thickness ratio. Cylinders with R/t less than 400 fail plastically, irrespective of imperfection amplitude, whereas those at higher R/t all buckle elastically, even if a high imperfection amplitude causes a dramatic reduction in buckling strength. Under high internal pressure, the sensitivity of a thin cylindrical shell to imperfections is much reduced, as shown by Rotter and Teng (1989, 1992) and Rotter (1990, 1996, 2004). The reason for this is that the pressure causes the radial deformation to be raised, which introduces circumferential tensions, Eq. 4-17a. This circumferential membrane tension reduces the imperfection sensitivity and the axial loads at buckling increase (Rotter, 1989, 1990; Teng and Rotter, 1992). Teng and Rotter (1992) demonstrated that some localization of buckling deformations occurs as the internal pressure increases. The diamond buckles observed at low internal pressures become shorter in the axial direction until the buckling mode is axisymmetric at high internal pressure (Rotter, 1990). Figure 5-1 shows the buckling strength predictions of thin pinned cylindrical shell with R/t=1000, under internal pressure accompanied with vertical load.

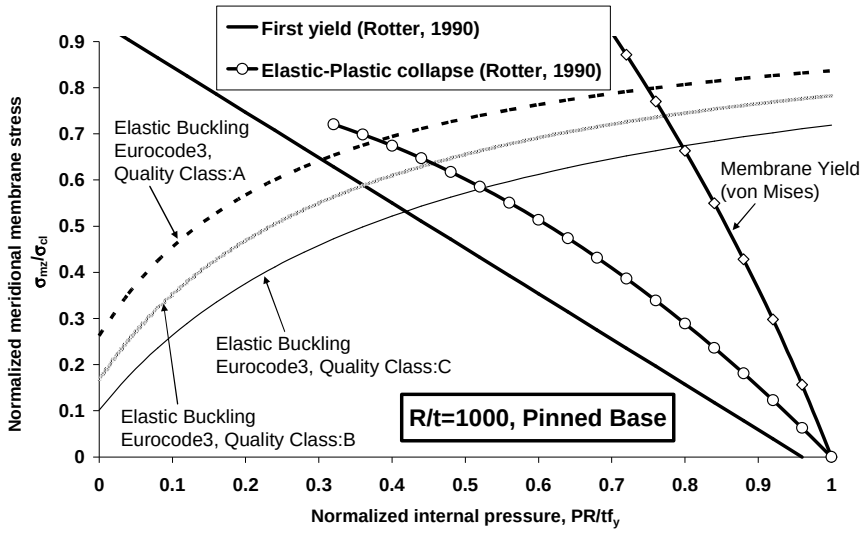

Fig. 5-1: Buckling strength predictions for R/t=1000 of pinned cylindrical shell.

Figure 5-1 was plotted using the appropriate equations presented by Rotter (1989, 1990). The von Mises stress, σ_{vM}, on the outside surface of the shell can then be written as follows:

$$\sigma_{vM} = \sqrt{(\sigma_{mz} + \sigma_{bz})^2 - (\sigma_{mz} + \sigma_{bz})(\sigma_{m\theta} + \nu\sigma_{bz}) + (\sigma_{m\theta} + \nu\sigma_{bz})^2} \qquad (5\text{-}1)$$

While the meridional membrane stress, σ_{mz}, is constant, it can be seen that the circumferential membrane stress, $\sigma_{m\theta}$, and the meridional bending stress, σ_{bz}, dominate von Mises stress.

The membrane value of the von Mises stress, σ_{vM0}, can be found from Eq. 5-1 when the bending moment is zero and the lateral displacement, w, is w_m, where w_m is the membrane theory normal deflection (Eq. 4-15).

In addition, the axial stress at first yield at a developing elephant's foot buckle can be predicted by Rotter 's (1989) approximation to the exact solution of the non-linear elastic bending equations:

$$\sigma_{mz} = \sigma_{cl}\left[1-\left(\frac{pR}{tf_y}\right)^2\right]\left(1-\frac{1}{1.12+\rho^{1.5}}\right)\left[\frac{\rho+\dfrac{f_y}{250}}{\rho+1}\right] \qquad (5\text{-}2)$$

$$\sigma_{vM_{\max}} = \left(\frac{pR}{t}+0.3\sigma_{mz}\right)\left(2.725+\frac{1+0.55\sigma}{\sqrt{1-\sigma^2}}\right)-2.65\frac{pR}{t} = f_y \qquad (5\text{-}3)$$

in which:

$$\sigma = \frac{\sigma_{mz}}{\sigma_{cl}} \qquad (5\text{-}4)$$

$$\rho = \frac{1}{400}\frac{R}{t} \qquad (5\text{-}5)$$

and σ_{cl} is the classical elastic buckling stress given by Eq.(2-1).

The elastic bifurcation buckling in other parts of the imperfect shell was described by Rotter (1997) and Eurocode3 Part1.6 (2007). This elastic buckling is related to the radius to thickness ratio and fabrication quality (Eurocode3 Part1.6, 2007) class as:

$$\sigma_{mz} = \sigma_{cl}.\alpha_z \tag{5-6}$$

where α_z is the meridional elastic imperfection factor, obtained from:

$$\alpha_z = \frac{0.62}{1+1.91(\Delta w_k / t)^{1.44}} \tag{5-7}$$

in which Δw_k is the characteristic imperfection amplitude, which Rotter (1997) proposed as:

$$\frac{\Delta w_k}{t} = \frac{1}{Q}\sqrt{\frac{R}{t}} \tag{5-8}$$

where, Q is the meridional compression fabrication quality parameter (Table 5-1) as specified by Eurocode 3 Part 1.6 (2007) and Rotter (2004).

Table 5-1: The meridional compression fabrication quality parameter, Q

Fabrication tolerance quality class	Description	Q
Class A	Excellent	40
Class B	High	25
Class C	Normal	16

From Fig. 5-1, it can be seen that elastic buckling occurs at low internal pressures. By increasing the internal pressure, yield of the wall leads to a local reduction of the flexural stiffness and the displacements increase. The circumferential membrane stress resultants are raised (Rotter, 1989) and elastic-plastic buckling occurs (Rotter 1990). At the base boundary condition, this elastic-plastic instability failure is known as elephant's foot buckling. Further, Rotter (1990) showed that, for thin cylinders, a clamped base provides a considerable increase in strength, whilst in thick cylinders, clamped and simple supports are similar.

5.3 Finite element analysis procedures

Using ABAQUS (Version 6.5-4), a cylindrical shell was studied with a height *h* of 5000mm, a radius *R* of 5000mm and thickness t_s of 5mm. This gives a radius to thickness ratio of 1000, and corresponds to a medium- length cylinder according to Eurocode3 part 1.6 (2007).

Young's modulus, E_s, and Poisson's ratio, ν_s, of the metal cylindrical shell were taken as 200 GPa and 0.3 respectively. Figure 5-2 shows the assumed stress-strain relationship for the metal.

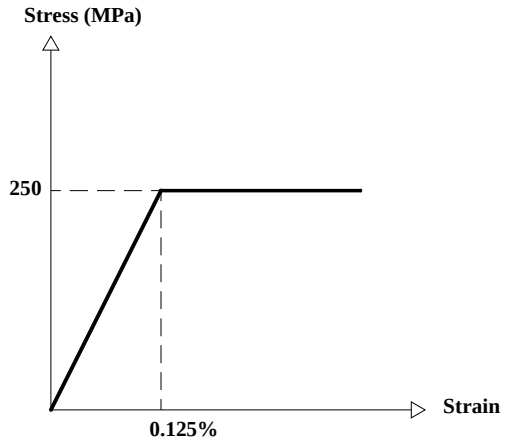

Fig. 5-2: Stress-Strain relation of the metal cylindrical shell.

The boundary condition at the bottom was taken as simply supported (radial, axial and circumferential displacements restrained, but not the rotation) and for the top, the boundary was free in all directions except for rotation about the circumference. These boundary conditions ensure that the local buckling occurs only at the base (Teng and Hu, 2007).

A uniform internal pressure of p and a vertical load per unit circumference of N_z were applied to the shell. The cylindrical shell was modelled using element SAX1. Element SAX1 is a 2-node axisymmetric general-purpose shell element with the effect of transverse shear deformation included (ABAQUS (Version 6.5-4)). Each node has three degrees of freedom (radial, axial displacements and a rotation). Using an axisymmetric element for modelling the shell in this case was considered from the fact that only axisymmetric collapse is expected. This element is also useful for saving computational time (Teng and Hu, 2007).

Geometrically and Materially Non linear Analysis (GMNA) was used with a modified Riks approach (Riks, 1979) to trace the nonlinear response. The Riks method, known as the "arc-length" technique, is an incremental approach to the solution of buckling and snap through problems (Fig. 5-3). In the Riks technique, both the load and displacement magnitude are unknown. It is assumed that there is a fixed coupled constraint which can be described as an arc length, ΔL, as an

additional equation to the equilibrium equations. Figure 5-4 shows the starting point S0, which is followed by an initial solution S_1 in the first iteration which then moves to S_2 in the second iteration by circular motion dS with centre at S_0 and with ΔL as a radius (Tsai and Palazotto, 1990, 1991). Finally, a convergence to the exact solutions S can be obtained.

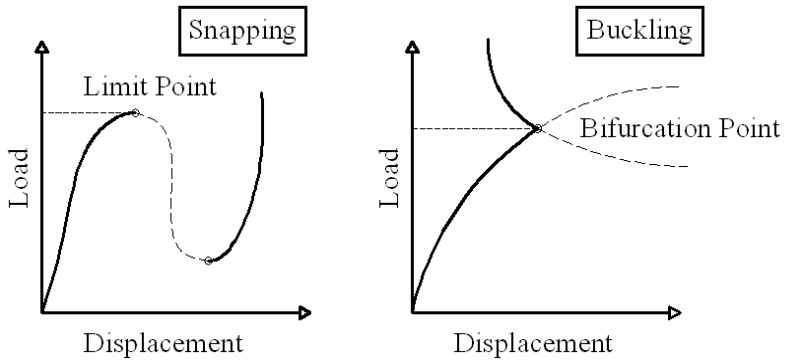

Fig. 5-3: Instability problems (Riks, 1979).

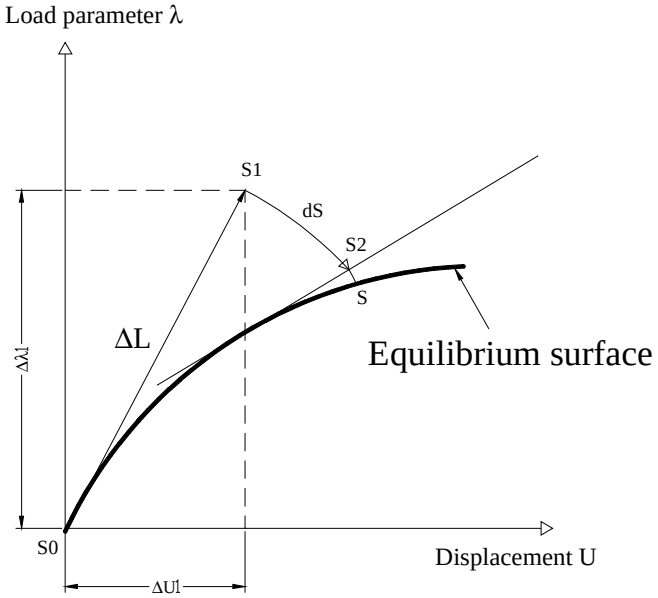

Fig. 5-4: Procedure for modified Riks method.

A mesh convergence study was conducted, as shown in Figs 5-5 and 5-6, for the cylinder described above. Figure 5-5 shows the change in the critical buckling stress divided by the classical buckling stress (Eq. 2-1) for different meshes for the cylinder under axial load only. As an alternative, Fig. 5-6 explores the change in the collapse internal pressure for different meshes for the same cylinder under uniform

internal pressure only. This mesh convergence leads to a mesh of height $0.02\sqrt{Rt}$ elements over a height of λ, the linear bending half-wavelength, above base. In fact, this mesh is very fine in comparison to the studies of Rotter and Teng (1989) and Rotter and Zhang (1990), where cubic elements of length of $0.25\sqrt{Rt}$ were used.

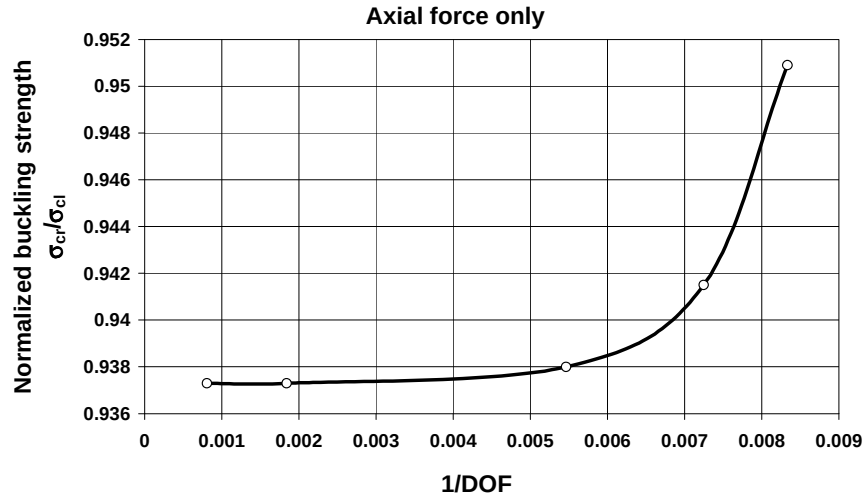

Fig. 5-5: Mesh convergence study for the cylinder under axial load only.

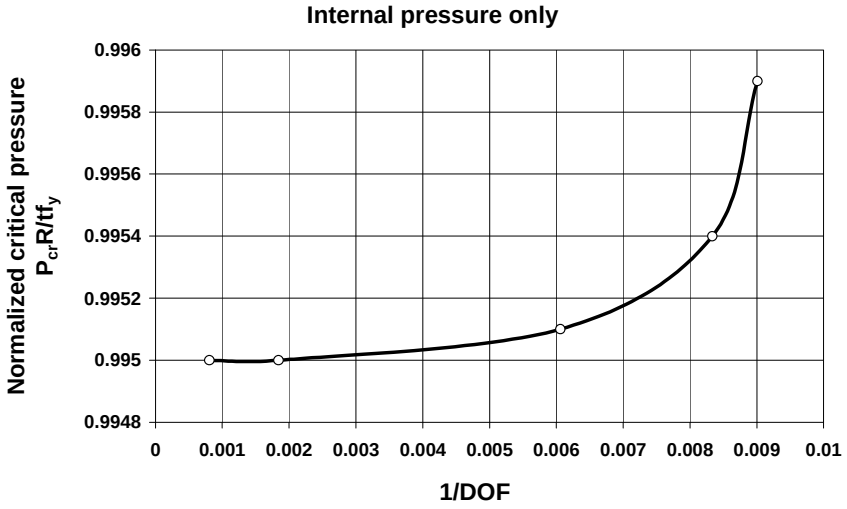

Fig. 5-6: Mesh convergence study for the cylinder under internal pressure only.

The collapse predictions of Fig. 5-1 are verified again using the element length given in this study (Fig. 5-7). From Fig.5-7, it is clear that the elastic plastic collapse strengths obtained by this study are very close to the equation developed by Rotter (1990) (Eq. 5-2).

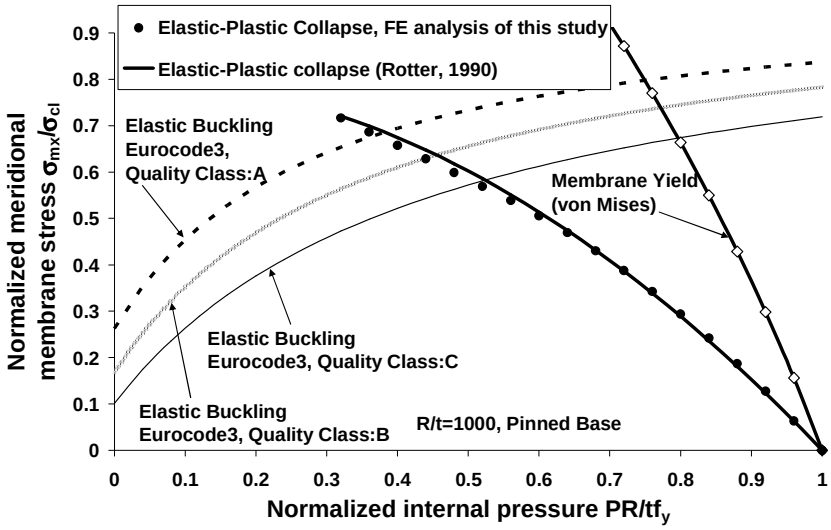

Fig. 5-7: Collapse predictions for R/t=1000 of pinned cylindrical shell.

5.4 Strengthening the cylindrical shell using FRP

For the cylindrical shell modelled in Section 5.3, an FRP sheet with a height of h_f is bonded to the external surface of the cylindrical shell starting at a distance x_f above the base. The FRP sheet is treated as orthotropic with Young's modulus in the circumferential direction, $E_{f\theta}$ and in the meridional direction, E_{fz} and with a Poisson's ratio in the circumferential direction, $\nu_{f\theta}$. The FRP lamina was modelled using element SAX1 defined in Section 5.3. Further, a perfect bond between the cylinder and the FRP strengthening was assumed.

To verify the model above, a comparison with the experimental results of Teng and Hu (2004, 2007) is shown in Fig. 5-8. The study of Teng and Hu (2004, 2007) was to demonstrate the effect of FRP confinement on thicker steel tubes. The experiments were done using a GFRP jacket.

In order to compare the experimental results of Teng and Hu with the model of this study, a fixed-base steel tube with height h of 450mm, radius R of 80.4mm and thickness t_s of 4.2mm was studied with Young's modulus E_s of 201GPa, Poisson's ratio ν_s of 0.3 and yield stress of 335 MPa with strain hardening modulus of 5% of the elastic value. GFRP was modelled over the whole height of the tube and had a thickness t_f of 0.53mm which refers to the three-ply FRP jacket of Teng and Hu. An orthotropic GFRP sheet was considered with moduli $E_{f\theta}$ and $\nu_{f\theta}$ as 80.1GPa and 0.35 respectively. The Young's modulus in the meridional direction of FRP, E_{fz}, was

ignored first, as in the work of Teng and Hu, because of its small stiffness. It was later taken as 3GPa.

It is worth mentioning that Teng and Hu modelled their tests using ABAQUS using B33 elements oriented in the hoop direction. B33 is a bi-cubic beam element with six degrees of freedom per node. The height of its cross section was taken as the height of the shell element. Also, elements S4R were used to model the tube. S4R is 4-node doubly curved general-purpose shell, with reduced integration with hourglass control and the effect of transverse shear deformation included (ABAQUS (Version 6.5-4)). Each node has six degrees of freedom (three displacements and three rotations).

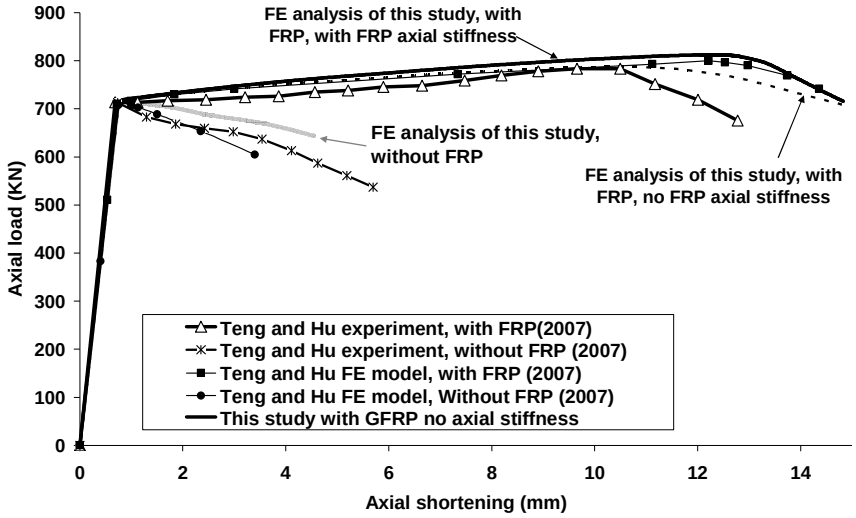

Fig. 5-8: Load-axial shortening curves.

Figure 5-8 shows the experimental load-deflection curves for a matched pair of experiments with and without FRP strengthening. The calculated load-deflection curves of Teng and Hu are also shown together with the calculated curves from this study.

These tests and calculations show that the strength and ductility of the steel tube are increased greatly by using FRP. Further, the shell elements to model the FRP used here give a failure load much closer to the experiment than the FE analysis of Teng and Hu (2007) where beam elements were used. Furthermore, a higher collapse load is observed when the axial stiffness of the FRP sheet is included. However, the above tube is a thick cylindrical shell, where R/t was around 19.

To demonstrate the strengthening effect of FRP on a thin cylindrical shell, the cylindrical shell of Section 5.3 with externally attached FRP with a Young's modulus in the circumferential direction, $E_{f\theta}$, of 230 GPa, and in the meridional direction, E_{fz}, of 3GPa, with a Poisson's ratio in the circumferential direction, $\nu_{f\theta}$, of 0.35 was analysed.

An internal pressure of 0.2 N/mm^2 was applied. In addition, different FRP thicknesses were explored using the height ratio $h_f/\lambda = 1$ and with the FRP extending to the base (starting point ratio above the base, $x_f/\lambda = 0$). The quantity of FRP is here characterised by the stiffness parameter α given by Eq. 4-8 ($\alpha = E_{f\theta}t_f/E_s t_s$).

Figure 5-9 shows the effect of changing the value of the stiffness parameter α on the load-axial shortening relationship, including the changing axial stress at bifurcation or collapse.

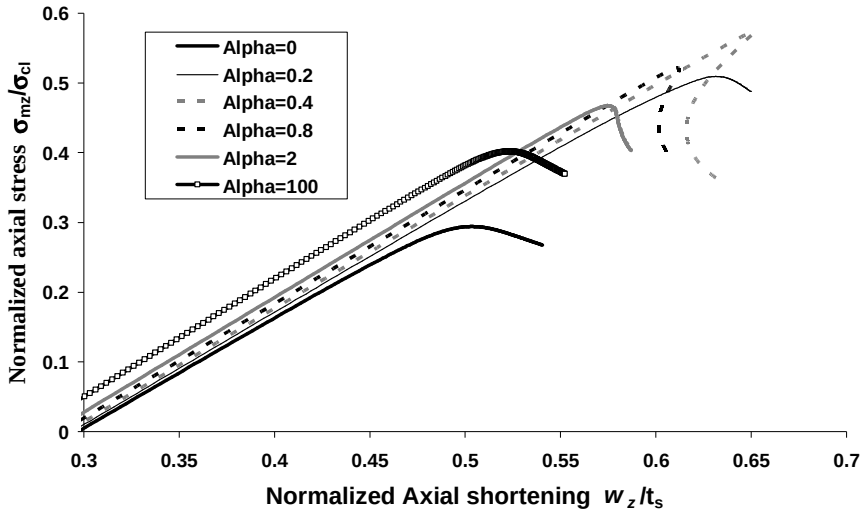

Fig. 5-9: Effect of FRP thickness on load- axial shortening curves ($h_f/\lambda = 1$ and $x_f/\lambda = 0$).

From Fig. 5-9, it can be seen that as α increases the strength increases. But the strengthening effect can be seen to be sensitive to the thickness of the FRP. Both too little and too much FRP thickness lead to a lower strength.

The effect of changing the strip height ratio, h_f/λ, is shown in Fig. 5-10 where $x_f/\lambda=0$ and the stiffness parameter $\alpha=0.4$. The value $\alpha=0.4$ was chosen because it appeared to be the optimal in Fig. 5-9.

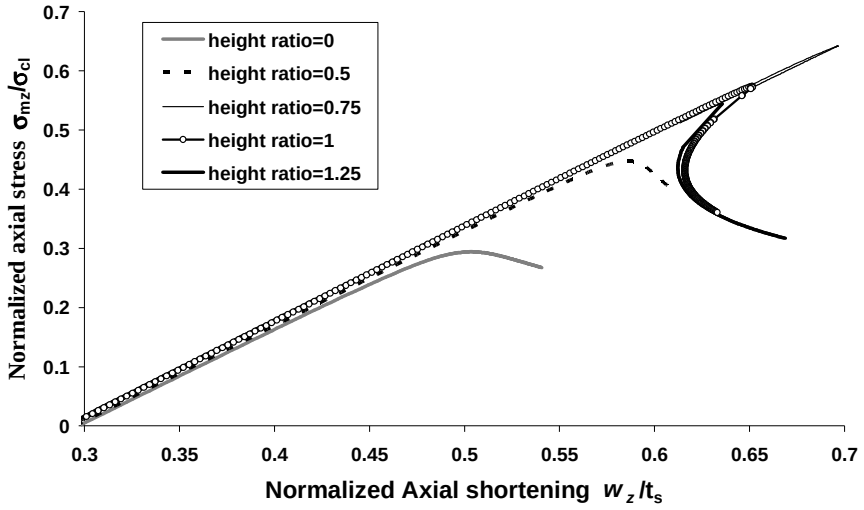

Fig. 5-10: Effect of height ratio on load –axial shortening curves (α = 0.4 and x_f/λ = 0).

Figure 5-10 also shows that the height ratio affects the strength. It is clear that if a larger or smaller height ratio than the optimal one is used, the strength is reduced. The effect of changing the starting point ratio of FRP, x_f/λ, was explored. The result is in Fig. 5-11 where the thickness ratio α and end point ratio $(x_f+h_f)/\lambda$ are fixed at 0.4 and 0.75 respectively, these being the optimal values from Fig. 5-10.

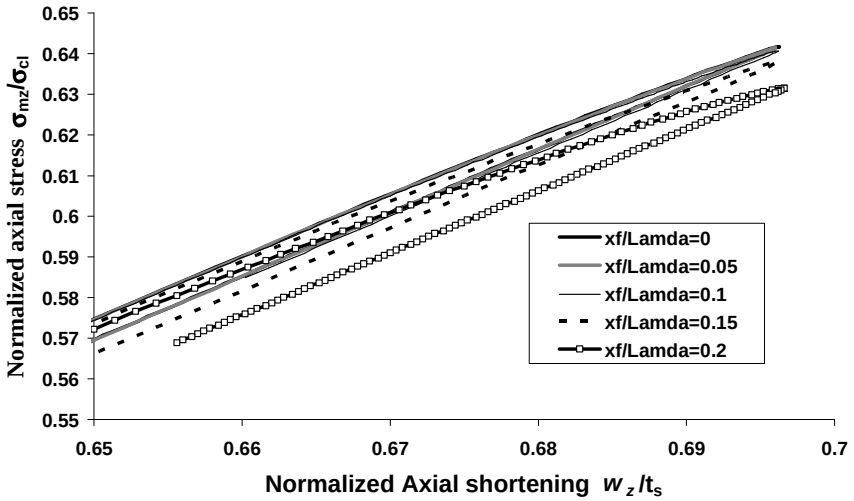

Fig. 5-11: Effect of starting point ratio on load-axial shortening curves (α = 0.4 and $(x_f+h_f)/\lambda$=0.75).

Figure 5-11 shows that the strength decreases when x_f is increased, but it is not as sensitive to this parameter as it is to t_f and h_f, as indicated by Figs 5-9 and 5-10 respectively.

5.5 Optimal dimensions of FRP sheet for strengthening a cylinder against elephant's foot collapse

Since the FRP sheet was added to function in circumferential tension in the zone of peak von Mises stress, it is natural that this critical zone should be the zone of elastic plastic collapse, as indicated in Fig. 5-1. Therefore, the principal aim of using FRP is to increase the axial load of an elastic-plastic collapse to the value that can be achieved by elastic buckling. That is to say, the FRP cannot be usefully deployed to increase the membrane yield resistance of the whole shell, since that would require it all to be treated. Therefore, the limiting maximum axial load to which the FRP can usefully enhance the strength is shown by the lines marked with circles in Fig. 5-12 for each fabrication quality class.

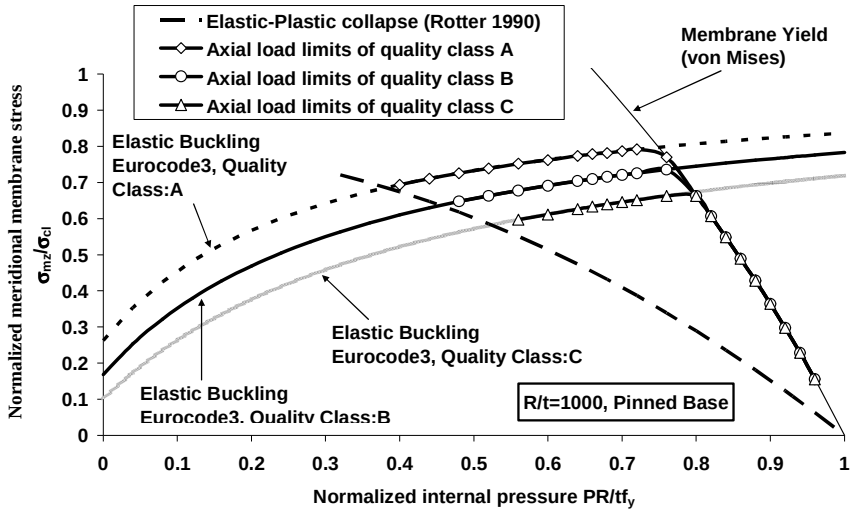

Fig. 5-12: Membrane axial stress limits by using FRP.

It is evident that changing the three parameters that determine the deployment of the FRP sheet t_f, h_f and x_f at the same time is very complicated. Therefore, the method chosen for this study was to fix two parameters and change the third one until an optimal value of each parameter was found.

For the same cylindrical shell (see Section 5.3) and FRP properties (see Section 5.4), different values of height ratio h_f/λ were explored, with stiffness parameter α=0.46 and starting point at the base, $x_f/\lambda = 0$. Figure 5-13 shows the changing of buckling strength as the height ratio changed.

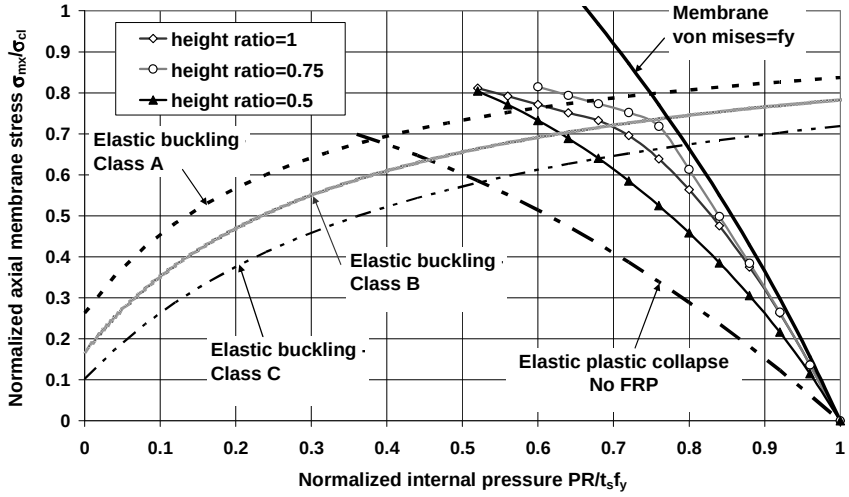

Fig. 5-13: Effect of height ratio on buckling strength (α = 0.46 and x_f/λ = 0).

The three values of height ratio used in Fig. 5-13 indicate that a height ratio of 0.75 is close to the value needed to obtain the maximum buckling strength.

Next, different values of the stiffness parameter α (Eq. 4-8) were explored, with the fixed height ratio of 0.75 and x_f/λ=0. The changing buckling strength is shown in Fig. 5-14 of the three values shown (α=0.23, 0.46 and 0.69). The highest buckling strength is found when α=0.46. This suggest that a value around α=0.5 may be optimal.

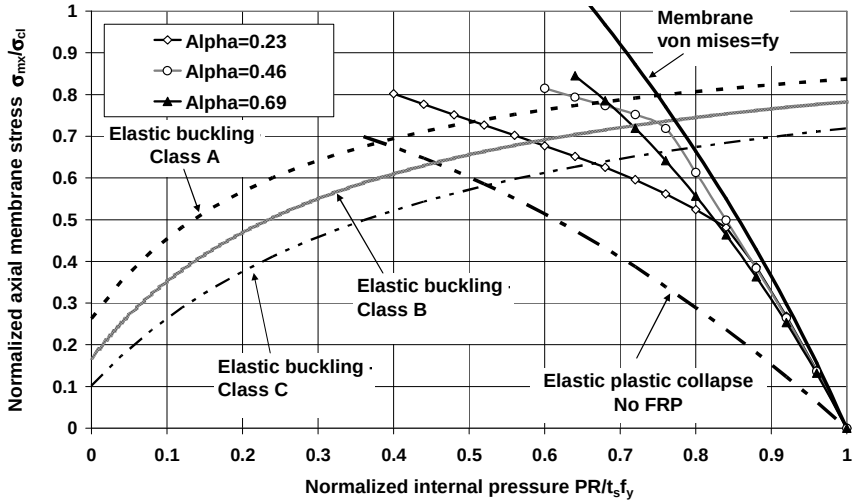

Fig. 5-14: Effect of FRP thickness on buckling strength (h_f/λ = 0.75 and x_f/λ = 0).

Finally, different values for the starting point ratio x_f/λ were chosen using the height ratio $(x_f+h_f)/\lambda=0.75$ and the stiffness ratio $\alpha=0.46$. The results are shown in Fig. 5-15, where it is clear that the starting value has little impact on the strength, within the range of values explored (x_f/λ =0, 0.065, 0.13 and 0.26).

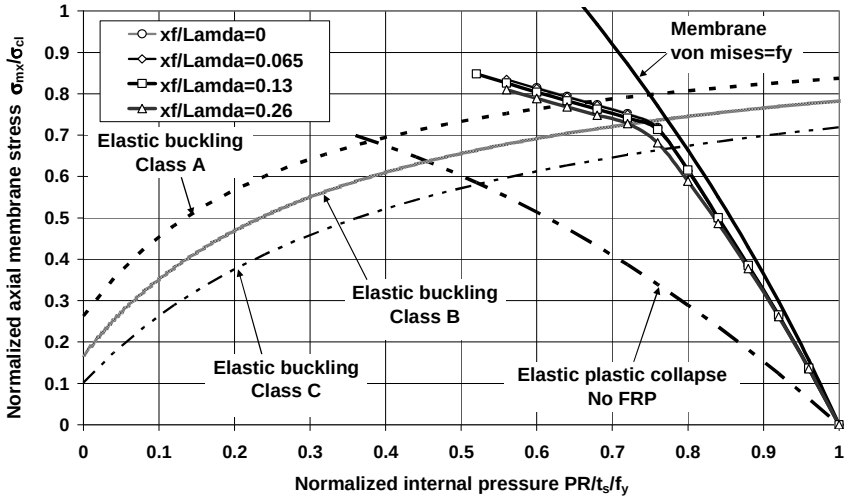

Fig. 5-15: Effect of starting point ratio on buckling strength (α = 0.46 and $(x_f+h_f)/\lambda=0.75$).

By following the same procedure described above, many examples were studied using the finite element analysis (e.g. Fig. 5-16). On the basis of these calculations, the optimal values were found for all three parameters, covering the FRP thickness, height, and starting point in relation to the internal pressure and axial force within the metal cylinder.

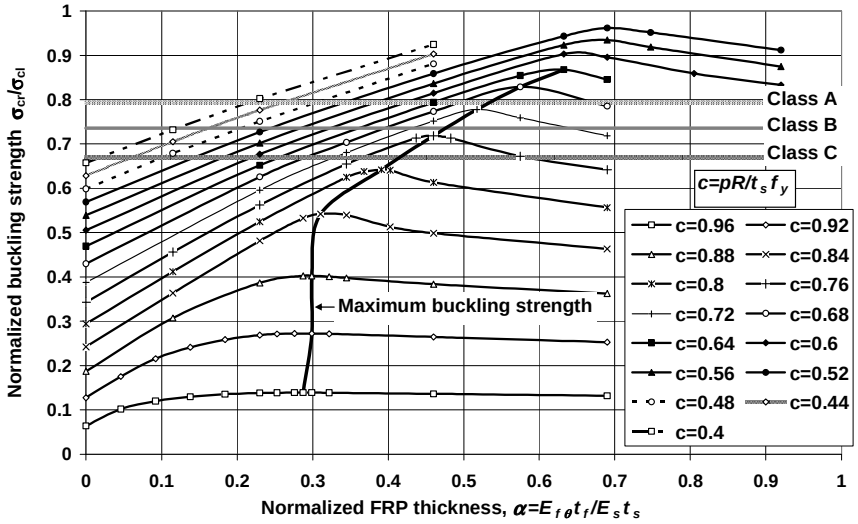

Fig. 5-16: Variation of buckling strength with h_f/λ = 0.75 and x_f/λ = 0.

The results of the optimisation process are shown in Figs 5-17, 5-18 and 5-19. For every design pressure and identified quality class, an optimum value of the three parameters of the normalized FRP thickness α (Eq. 4-8), height $\omega_b=\pi h_f/\lambda_b$ (Eq. 4-24e), and starting point $\omega_c=\pi x_f/\lambda$ (Eq. 4-28e) was found.

The internal pressure p was characteristic here in terms of the parameter:

$$P_n = \frac{pR}{t_s \sigma_{vM\,0}} \tag{5-9}$$

in which:

σ_{vM0} is the membrane von Mises stress (Section 5.2) and λ_b is the meridional bending half- wavelength for the section where the FRP was attached (Eq. 4-16a).

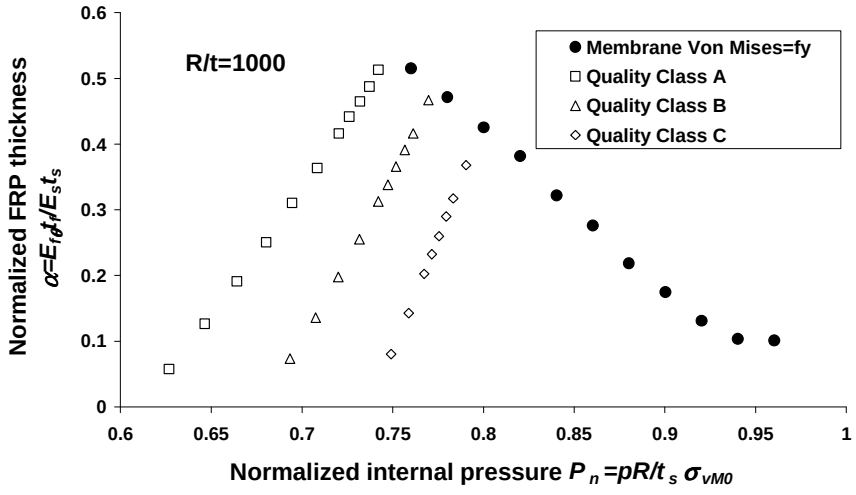

Fig. 5-17: Optimal FRP thickness, t_f.

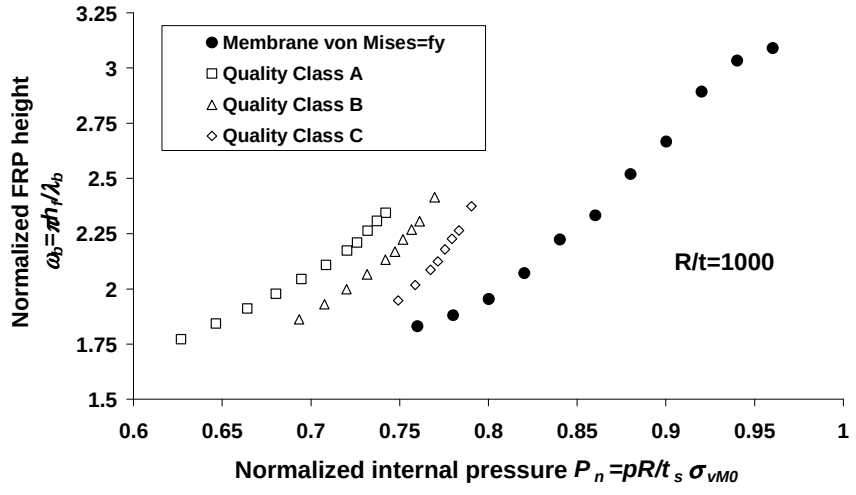

Fig. 5-18: Optimal FRP height, h_f.

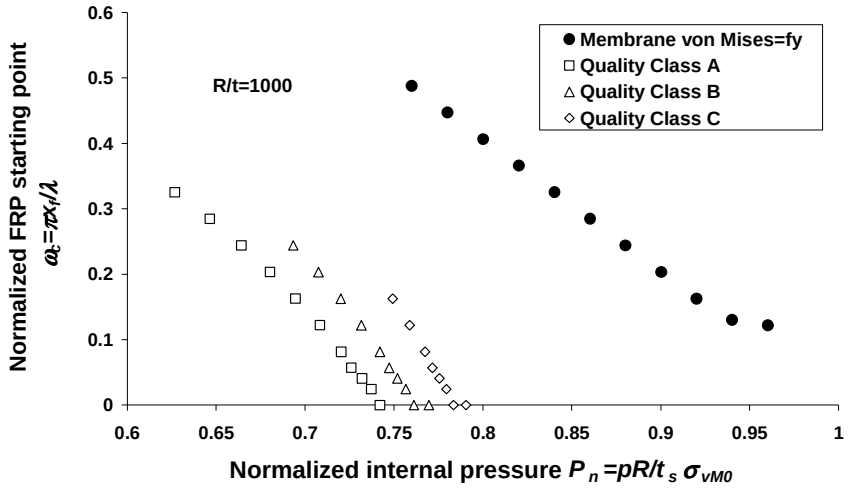

Fig. 5-19: Optimal FRP starting point, x_f.

This results show that the optimal height (Fig. 5-18) is relatively insensitive to the quality class and internal pressure, but that the optimum stiffness ratio α and starting point of ω_c both vary very strongly with internal pressure.

5.6 Empirical formulas for the optimal attached FRP

From the above optimisation, it can be seen clearly that there are two parts for each of the required parameters. The high pressure part is required to achieve the membrane yield strength, while the low pressure is required to ensure that the elastic imperfect buckling strength is reached (Fig. 5-12).

5.6.1 The required parameters for membrane yield

A roughly exponential relationship can be observed from Figs 5-17, 5-18 and 5-19 to obtain the parameters t_f, h_f and x_f for the membrane yield part, it is suggested that the following expression can give a good empirical match:

$$A + B\cos(cP_n)e^{cP_n} \tag{5-10}$$

in which the constants A, B and C take different values for each parameter. The dimensionless pressure parameter P_n is given in Eq. 5-9.

5.6.1.1 The required FRP thickness, t_f

The constant values of A, B and C for the FRP thickness can be as follows:

$$\alpha = \frac{E_f \theta^t f}{E_s t_s} = 0.66 - 0.00068\cos(7.39P_n)e^{7.39P_n} \quad (5\text{-}11)$$

5.6.1.2 The required FRP height, h_f

A, B and C for the FRP height are shown in Eq. 5-12:

$$\omega_b = \frac{\pi h_f}{\lambda_b} = 1.79 - 0.0000687\cos(10.5P_n)e^{10.5P_n} \quad (5\text{-}12)$$

5.6.1.3 The required FRP starting point, x_f

Deriving the constants A, B and C from Fig. 5-19 for the FRP starting point gives:

$$\omega_c = \frac{\pi x_f}{\lambda} = 0.591 - 0.00056\cos(7.33P_n)e^{7.33P_n} \quad (5\text{-}13)$$

5.6.2 The required parameters for elastic buckling part

For the elastic buckling part, the function for the FRP parameters can be formed as Eq. 5-14:

$$A + Be^{CP_n} \quad (5\text{-}14)$$

5.6.2.1 The required FRP thickness, t_f

Producing the constant values of A, B and C from Fig. 5-17 for each class, which obtain a good estimation gives:

$$\alpha = \frac{E_f \theta^t f}{E_s t_s} = -1.31 + 0.288e^{2.48P_n} \quad \text{for Class A} \quad (5\text{-}15a)$$

$$\alpha = \frac{E_f \theta^t f}{E_s t_s} = -1.09 + 0.083e^{3.81P_n} \quad \text{for Class B} \quad (5\text{-}15b)$$

$$\alpha = \frac{E_f \theta^t f}{E_s t_s} = -1.72 + 0.118e^{3.64P_n} \quad \text{for Class C} \quad (5\text{-}15c)$$

5.6.2.2 The required FRP height, h_f

Eq.(5-16) shows the constants required for the FRP height:

$$\omega_b = \frac{\pi h_f}{\lambda_b} = 1.47 + 0.00124e^{8.84P_n} \quad \text{for Class A} \quad (5\text{-}16a)$$

$$\omega_b = \frac{\pi h_f}{\lambda_b} = 1.59 + 0.0000165e^{14.0P_n} \quad \text{for Class B} \quad (5\text{-}16b)$$

$$\omega_b = \frac{\pi h_f}{\lambda_b} = 1.66 + 0.0000000229e^{21.8P_n} \quad \text{for Class C} \quad (5\text{-}16c)$$

5.6.2.3 The required FRP starting point, x_f

Eq.(5-17) provides the constant values for the FRP starting point:

$$\omega_c = \frac{\pi x_f}{\lambda} = 0.644 - 7.08e^{6.07P_n} \quad \text{for Class A} \quad (5\text{-}17a)$$

$$\omega_c = \frac{\pi x_f}{\lambda} = 0.655 - 0.00351e^{6.87P_n} \quad \text{for Class B} \quad (5\text{-}17b)$$

$$\omega_c = \frac{\pi x_f}{\lambda} = 1.02 - 0.019e^{5.07P_n} \quad \text{for Class C} \quad (5\text{-}17c)$$

Figures 5-20, 5-21 and 5-22 show the comparison between the FE analysis for the optimal FRP parameters and the fitted formulas given in this section.

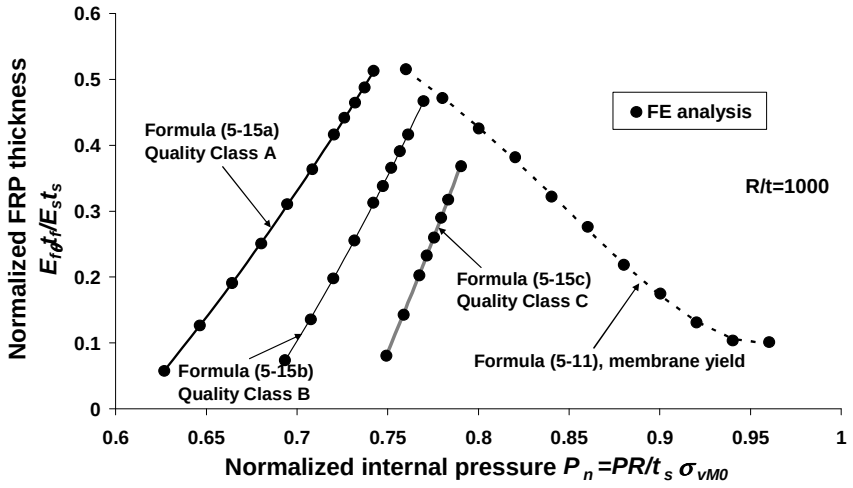

Fig. 5-20: t_f, the optimal thickness of attached FRP.

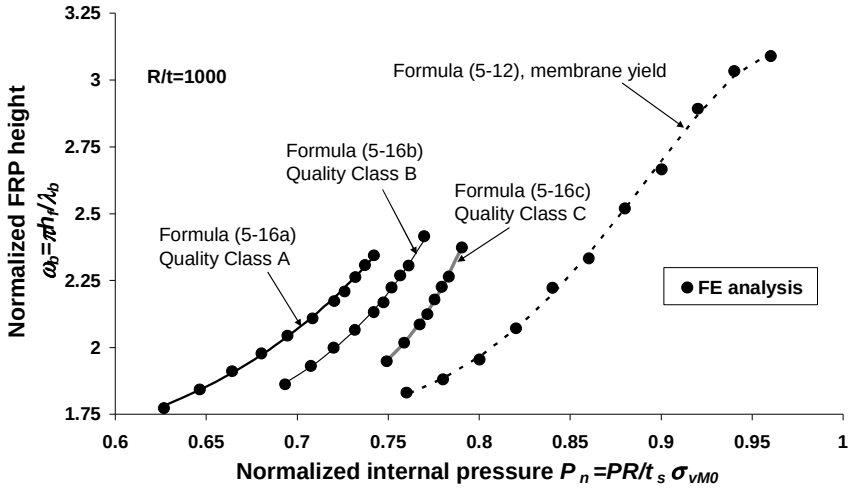

Fig. 5-21: h_f, the optimal height of the attached FRP.

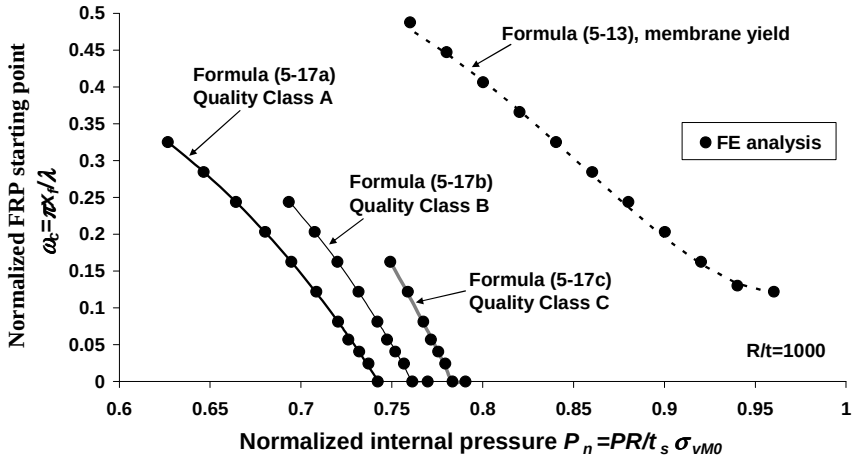

Fig. 5-22: h_f, the optimal starting point of the attached FRP.

The sensitivity of choosing FRP parameters different from the optimal ones is illustrated in Figs 5-23 and 5-24 for Quality Class A as an example.

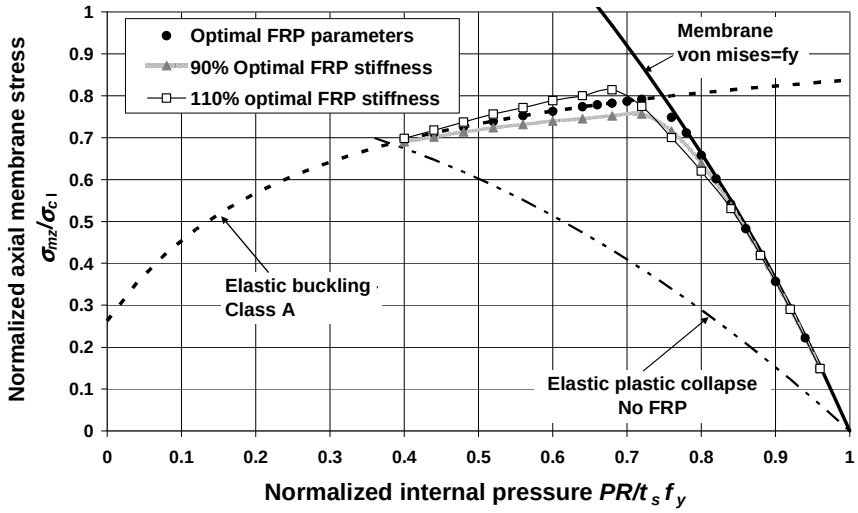

Fig. 5-23: The sensitivity of different FRP stiffness on the buckling strength.

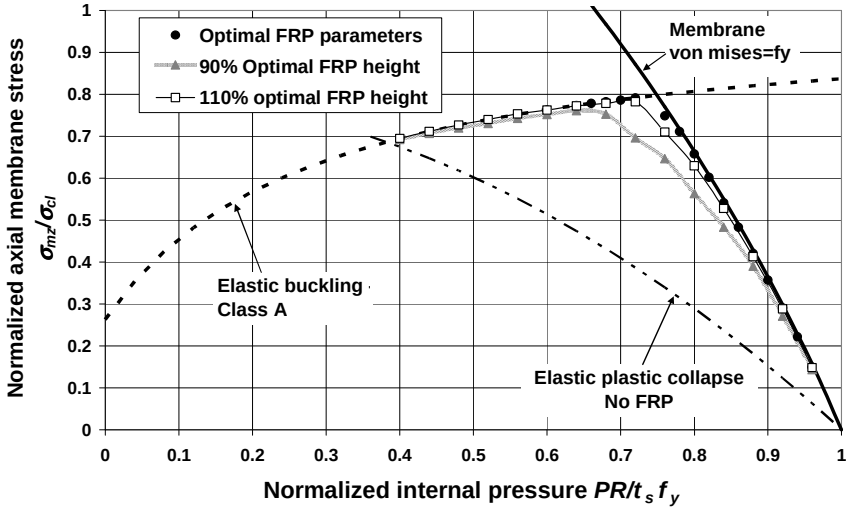

Fig. 5-24: The sensitivity of different FRP height on the buckling strength.

Even quite small changes from the optimal values lead to noticeable strength loss.

In the membrane yield zone of the curve, the buckling strength is more sensitive to the FRP height than FRP stiffness (Figs 5-23 and 5-24). For the elastic buckling part, the strength is more sensitive to the FRP stiffness α.

5.7 Summary

This chapter has studied the use of FRP to strengthen a cylindrical shell under internal pressure accompanied by vertical load. Geometrically and Materially Non linear Analysis (GMNA) has been used to explore the gain in buckling strength for an FRP-strengthened steel cylindrical shell. Moreover, the optimal FRP sheet required to prevent elephant's foot buckling for a cylindrical shell of radius to thickness ratio of 1000 as an example has been obtained. The fabrication quality classes were used, and empirical formulas were produced to identify the optimal strengthening condition.

Chapter 6

Elastic buckling of FRP-strengthened cylinders with axisymmetric imperfections

6.1 Introduction

The susceptibility of axially compressed cylinders to geometric imperfections when buckling in the elastic range has been recognized for over 50 years. One of the most damaging imperfection forms is a local axisymmetric imperfection. This chapter explores the possibility of enhancing the cylinder buckling strength by local application of an FRP repair.

Local axisymmetric imperfections are commonly present at welding joints. Geometrically Nonlinear Analysis with Imperfection (GNIA) is undertaken in this chapter to investigate the elastic bifurcation buckling under axial loads of an FRP-strengthened cylindrical shell with axisymmetric inward imperfections.

The chapter begins with a description of previous research on the buckling of unpressurized axisymmetric-imperfect cylinders.

Next, a finite element analysis using Geometrically Nonlinear Analysis with Imperfections (GNIA) is used to obtain the bifurcation buckling strength predictions.

Then, the effect of FRP strengthening on the buckling strength of a cylindrical shell with an axisymmetric imperfection is explored.

Finally, a summary of the work done in this chapter is presented.

6.2 Bifurcation buckling stress of a cylinder with a local axisymmetric imperfection

Axisymmetric or nearly axisymmetric imperfections in cylindrical shells are commonly present at welded joints where rolled steel plates are jointed together through a circumferential weld, or a ring stiffener is attached either at both ends of the shell or in between through welding. The heating and cooling process results in a circumferential depression at each circumferential joint. Rotter (1996, 2004) and Rotter and Teng (1989) showed that a local axisymmetric imperfection leads to a dramatic reduction in buckling strength, generally more than non-symmetric imperfection forms, and the highest amplitude of imperfection gives the lowest buckling strength.

The shape function to describe the circumferential weld depression is given by Eq. 6-1 (Rotter and Teng, 1989; Rotter, 1996, 2004; Pircher and Bridge, 2001):

$$\delta = \delta_0 e^{-\pi z/\lambda_0} (\sin\frac{\pi z}{\lambda_0} + K\cos\frac{\pi z}{\lambda_0}) \qquad (6\text{-}1)$$

in which δ_0 is the amplitude of the imperfection, λ_0 is the half wavelength for the adopted shape of imperfection, z is the axial coordinate from the middle of the imperfection and K takes the values 1 or 0, in order to define the type of the imperfection, whether it is A or B respectively (Fig. 6-1).

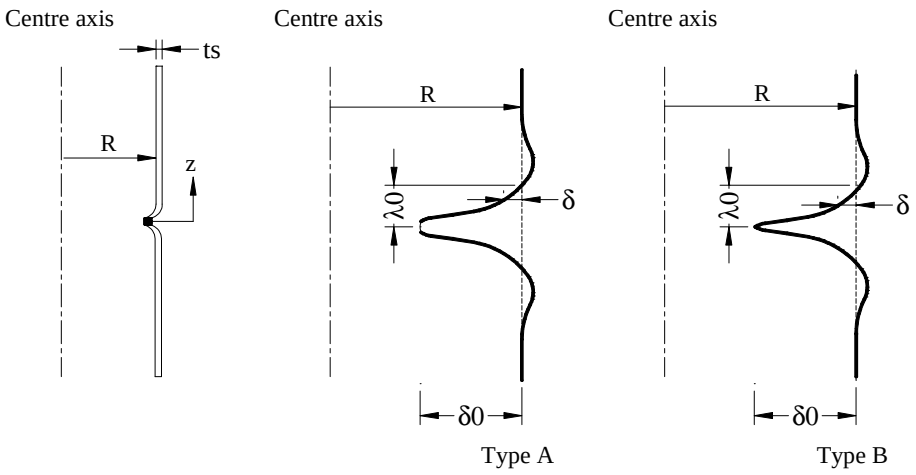

Fig. 6-1: The assumed shape types for the weld depression at the circumference.

Type A (K=1) was assumed to resist flexural yielding completely during cooling, whereas Type B (K=0) was assumed to be completely flexible during cooling (Rotter and Teng 1989). This local imperfection decays very rapidly away from the weld joint, as shown in Fig. 6-1. However, it was shown that Type A provides considerably less buckling strength than Type B, so the former is more commonly used (Rotter and Zhang 1990; Teng and Rotter, 1992; Rotter, 1997; Pircher and Bridge, 2001). Moreover, Pircher and Bridge (2001) studied the effect of changing of both K and λ_0 in Eq. 6-1 on the buckling strength of the imperfect cylinder. Their study found that K=1 and $\lambda_0=\lambda$, the bending half wavelength (Eq. 2-3), produce the lowest buckling strength for both the short cylinder and the long cylinder. This result confirms the work done by Rotter (1997), where the half wavelength for the imperfection equal to the bending half wavelength was found to produce a situation close to the worst case scenario when elastic buckling occurs.

The interaction between the adjacent imperfect joints (Fig. 6-2) has been explored by Rotter (1996) and Pircher and Bridge (2001).

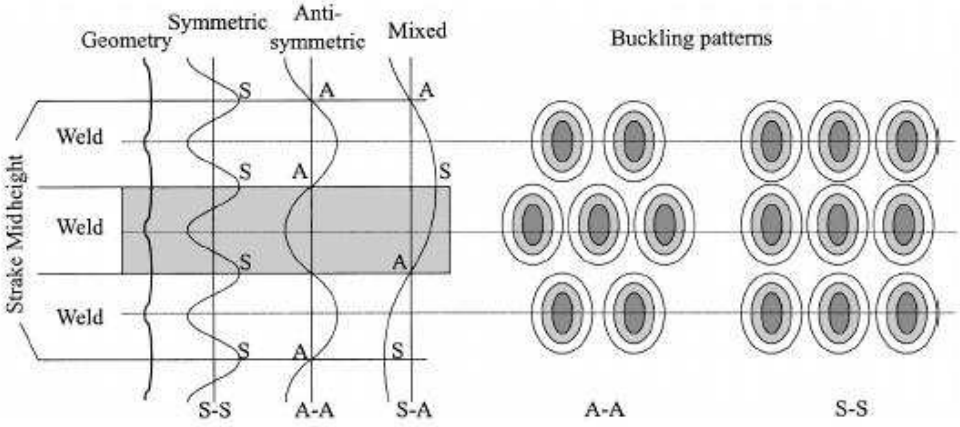

Fig. 6-2: Buckling modes and boundary conditions (Pircher and Bridge, 2001).

Rotter (1996) showed that the boundary conditions of A-A leads to much lower buckling loads than the repeated S-S weld. Further, Pircher and Bridge (2001) observed that the influence of the boundary conditions becomes insignificant with a large half-strake height. For instance, no difference in buckling strength between S-S and A-A was obtained with a half-strake height of 6λ for an imperfection amplitude δ_0 equal to t_s, the thickness of the strake.

6.3 Finite element analysis procedures

6.3.1 Geometry, boundary conditions, material properties and loading

A cylindrical shell with a height *h* of 3000mm, a radius *R* of 1000mm and a thickness t_s of 1mm was considered in this study. The shell had a radius to thickness ratio of 1000, and corresponds to a medium length cylinder according to Eurocode 3 Part 1.6 (2007). The wall thickness of the cylindrical shell was assumed to be constant over the whole structure. The boundary conditions at both ends are free in all directions except for rotations about the circumferential axis and the tangential displacement. The shell was made of a metal with Young's modulus E_s=200GPa and Poisson's ratio ν_s= 0.3 respectively. A uniform axial load N was applied at the top of the shell (Fig. 6-3).

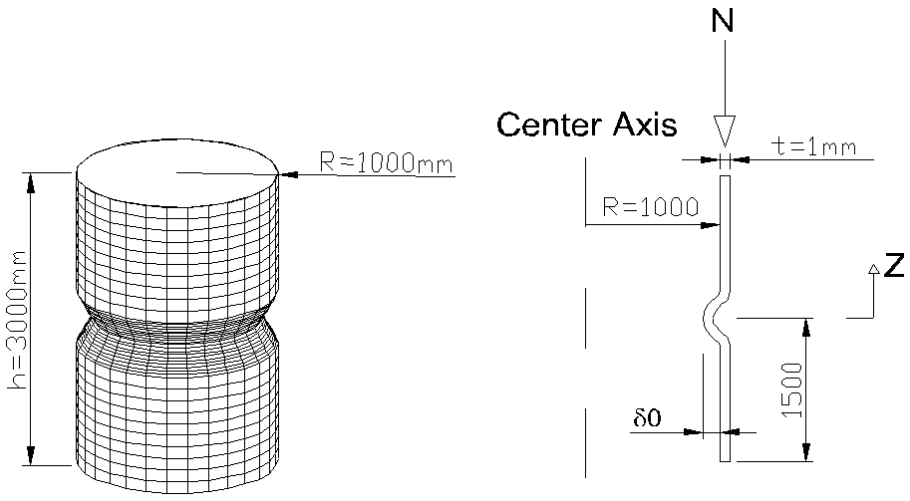

Fig. 6-3: The cylindrical shell.

The cylindrical shell was assumed to have an axisymmetric inward imperfection at the mid-height (Fig. 6-3). The shape of imperfection was chosen to be Type A as described by Rotter and Teng (1989):

$$\delta = \delta_0 e^{-\pi z/\lambda}(\sin\frac{\pi z}{\lambda} + \cos\frac{\pi z}{\lambda})(1+\rho\cos(n\theta)) \tag{6-2}$$

in which:

ρ is a parameter which leads to a non-symmetric imperfection shape around the circumference (Table 6-1).

n is the circumferential mode number at the bifurcation load (Table 6-1).

θ is the circumferential coordinate.

Table 6-1: The parameter r and the mode number for each imperfection amplitude.

Normalized initial dent depth, δ_0/t_s	ρ	n
0.1	0.002	26
0.25	0.002	24
0.5	0.002	22
1	0.005	18
1.5	0.02	14
2	0.06	12

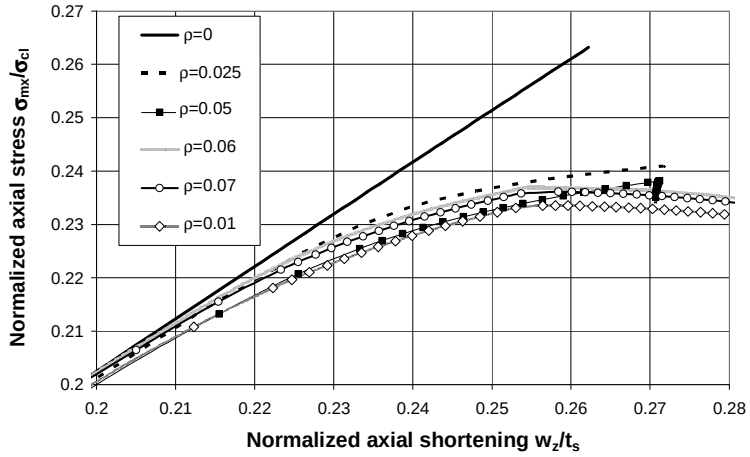

a) Axial stress- axial shortening curves.

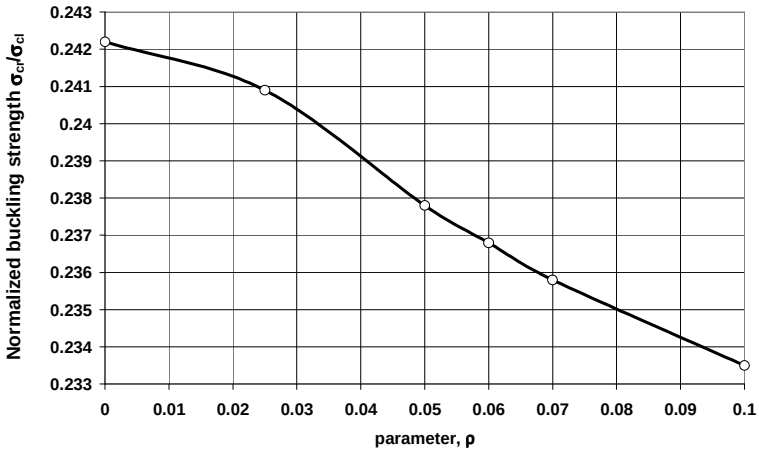

b) The parameter ρ against the normalized buckling strength.

Fig. 6-4: The effect of the parameter ρ on the buckling behaviour (δ_0/t_s=2).

The value of the parameter ρ was chosen as the minimum value which provides clear bifurcation point for the studied imperfection amplitude (Fig. 6-4).

Figure 6-4a shows the axial stress-axial shortening curves using different value of the parameter ρ for the imperfection amplitude δ_0 of $2t_s$. It is clear that no clear bifurcation load obtains when the parameter ρ is zero. The reduction in the axial load required after the bifurcation load (Fig. 6-4b) is not obvious until the parameter ρ takes a value of 0.06 for the imperfection amplitude of twice the wall thickness (δ_0/t_s=2).

This imperfection shape function provides the lowest buckling stress, as explored in Section 6.2. In addition, the half-strake height is around 20λ, where λ is the bending half wavelength (Eq. 2-3). Therefore, the effect of any interaction between neighbouring imperfections is ignored in this study.

6.3.2 FE analysis and modelling

Geometrically Non-linear Analysis with Imperfections (GNIA) was performed in this study using the finite element package ABAQUS (Version 6.5-4) and modified Riks method described in Section 5.3. The cylindrical shell was modelled using the 4-node doubly curved thin shell element S4R, as defined in Section 5.4.

The shell was assumed to behave elastically, and bifurcation buckling controls the ultimate strength of the shell. It may be noted that, however, cylinders with radius to thickness ratios bigger than 400 always buckle elastically (Rotter, 1997), although bifurcation may not always limit the strength of a cylindrical shell with very large imperfections, and plastic deformation may occur very soon after bifurcation (Rotter and Teng, 1989). Berry *et al.*, (2000) showed that plastic collapse failures can occur when the imperfection is large ($\delta_0/t_s > 3.5$) and the radius to thickness ratio is less than 500. For the example thin shell with moderate imperfections up to δ_0/t_s= 3.5, the bifurcation load is a reasonable limit.

A mesh convergence study was performed for a case with an imperfection amplitude of δ_0/t_s=2. To minimise the computational cost, a segment of 30 degrees of the circumference was modelled, as shown in Fig. 6-5, with symmetry conditions down the edges. Although this constrains the buckling mode a little, the effect is

small because this thin shell buckles with very many waves around the circumference (Rotter, 2004).

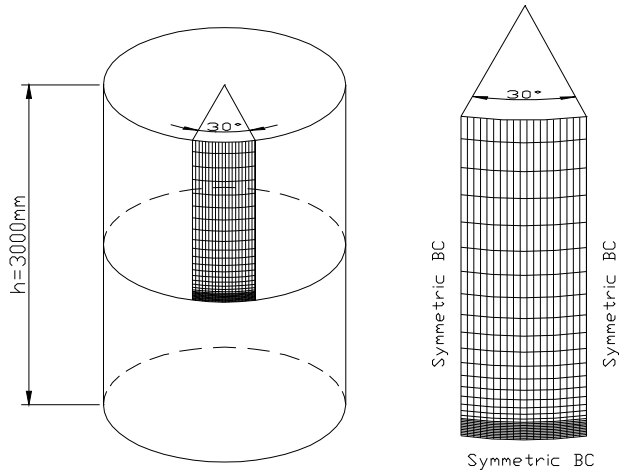

Fig. 6-5: The modelled part.

The mesh convergence was adopted in two directions: circumferentially and meridionally. In order to find the finest circumferential mesh, a constant number of 50 rows was assumed and the number of the circumferential columns was increased gradually. The change in the bifurcation stress on increasing the number of circumferential columns is shown in Fig. 6-6. It can be seen that a mesh of 80 columns in the circumferential direction is accurate enough for this study. Then, the number of rows was increased (Fig. 6-7) for a mesh with 80 columns around the 30^o circumference. The BIAS command of ABAQUS for rows was used. This command allows the nodes to be more concentrated near the imperfect edge and more widely spaced near the top of the cylinder.

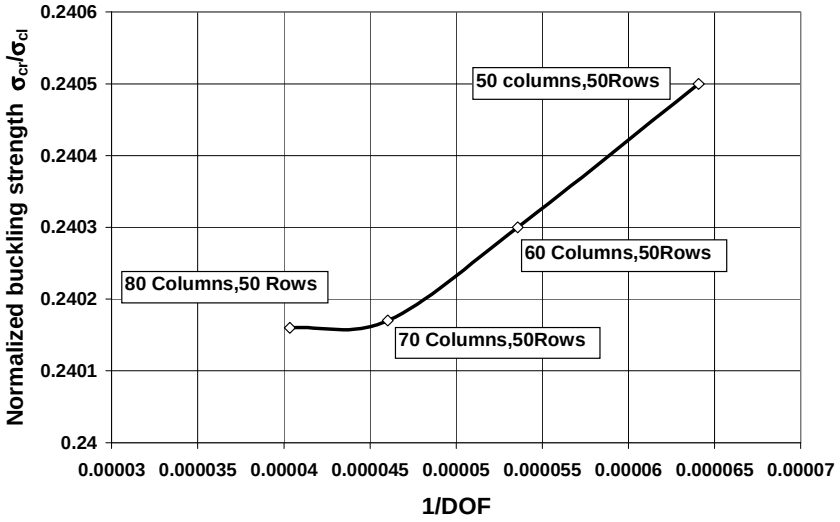

Fig. 6-6: Mesh convergence study for the imperfect shell in circumference.

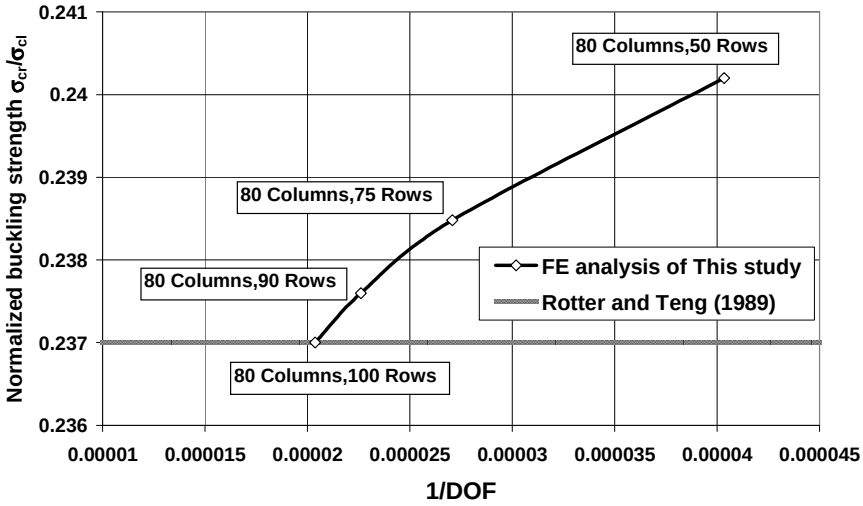

Fig. 6-7: Mesh convergence study for the imperfect shell in meridian.

The procedure above gives a very fine finite element mesh in the neighbourhood of the weld depression, as displayed in Fig. 6-5. By comparison with the model of Rotter and Teng (1989) (Fig. 6-7), it can be seen that a mesh of 100 rows down the meridian and 80 columns in circumference is adequate for this study. As a result, it is concluded that an element size of $0.2\sqrt{Rt_s}$ in both the circumferential and meridional directions near the weld depression is sufficient to give converged results. It may be noted that Rotter and Teng (1989) used an element size of $0.25\sqrt{Rt_s}$ in the meridional direction, but they used cubic elements. Berry *et al*. (2000) used 40 elements in each half wavelength λ for a cylinder with clamped

base, making a very fine mesh with element size of $0.06\sqrt{Rt_s}$ in the meridional direction.

6.3.3 Buckling stress of unpressurised imperfect cylinder

The buckling stress for a cylindrical shell under axial compressive loads is usually related to the classical buckling stress σ_{cl} given by Eq. 2-1.

Geometric imperfections are the main cause of strength reductions. Figure 6-8 shows the buckling modes at the bifurcation point within the circumferential segment studied for each imperfection amplitude. It is clear from Fig. 6-8 that the circumferential buckling mode number within the circumferential segment modelled for each imperfection amplitude complies with the full mode number (Table 6-1) within the full circle (360^o). This mode number provides the lowest buckling strength. On other hand, the meridional mode is very localized in the thin shells with shallow imperfection amplitude (e.g. $\delta_0/t_s=0.1$), but the whole shell is involved with deep imperfection amplitude (e.g. $\delta_0/t_s=2$) (Fig. 6-8).

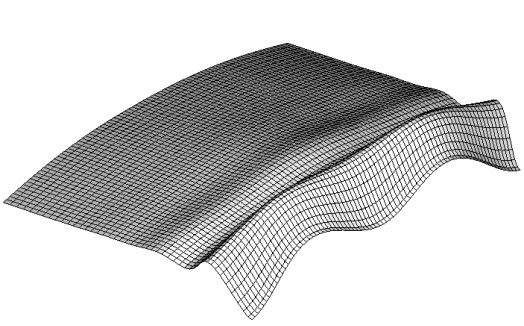

(2 circumferential modes within 27.7^o)

$\delta_0/t_s=0.1$

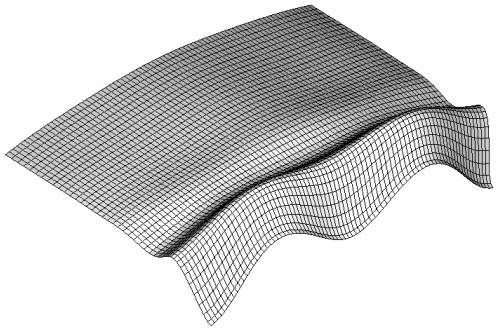

(2 circumferential modes within 30^o)

$\delta_0/t_s=0.25$

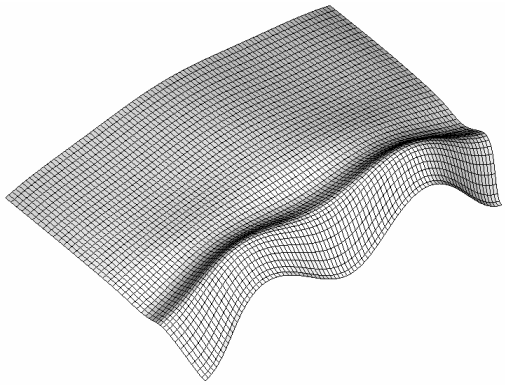

(2 circumferential modes within 32.7^o)

$\delta_0/t_s=0.5$

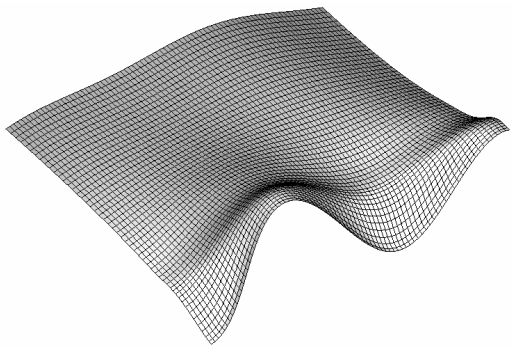

(1.5 circumferential modes within 30^o)

$\delta_0/t_s=1$

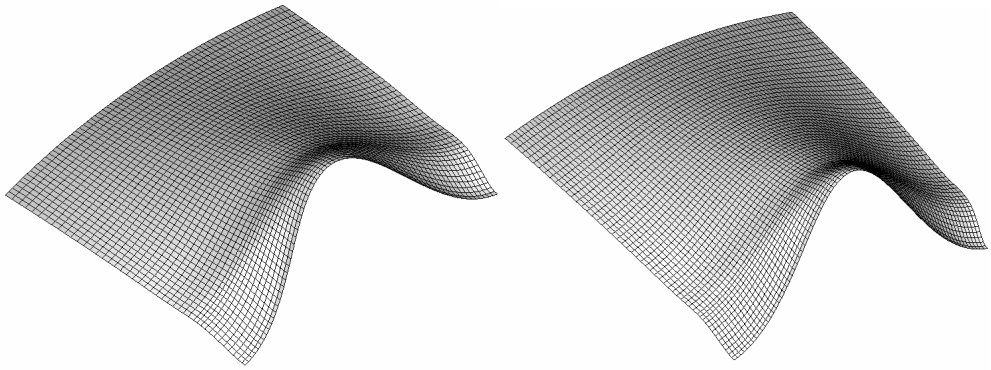

(1 circumferential mode within 25.7°) (1 circumferential mode within 30°)

δ_0/t_s=1.5 δ_0/t_s=2

Fig. 6-8: The deformation shape at the bifurcation point for different imperfection amplitudes.

The effect of the imperfection amplitude on the bifurcation buckling strength for the example cylinder under axial loads is shown in Fig. 6-9. It shows that the present FE study is in excellent agreement with the results obtained by Rotter and Teng (1989).

From Fig. 6-9, it may be noted that the clamped base investigated by Berry *et al*. (2000) provides a slight increase in buckling strength. This was also noted by Rotter (1990) for axially compressed and pressurized very thin cylinders with R/t>1000.

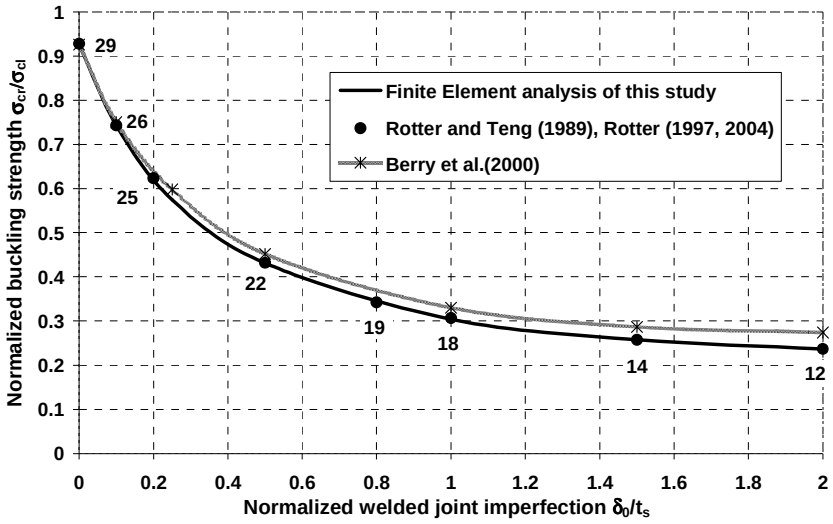

Fig. 6-9: Effect of imperfection on buckling strength and circumferentially buckling mode number.

6.4 Buckling stress of FRP strengthened imperfect cylindrical shell

It is proposed that FRP composites should be externally bonded to the area with imperfection on the example shell, as described earlier in Section 6.3.1. The FRP sheet is proposed to be centred at the mid-height of the imperfection and have a height h_f. Its moduli in the circumferential and meridional directions are $E_{f\theta}$ and E_{fz} respectively with a Poisson's ratio in the circumferential direction of $\nu_{f\theta}$. The FRP is bonded to the metal shell with an adhesive layer, which is treated as an isotropic material with Young's modulus E_a and Poisson's ratio ν_a. Both the FRP sheet and adhesive layer are modelled using the S4R element defined in Section 5.4.

To verify the model with FRP, a comparison with the work of Teng and Hu (2007) described in Section 5.4 was undertaken as shown in Fig. 6-10. The added adhesive elements in this study are considered to have a 1mm thick, 3GPa Young's modulus and Poisson's ratio of 0.35. Further, the meridional stiffness of the FRP sheet in this chapter is assumed to have a Young's modulus E_{fz} of 3GPa.

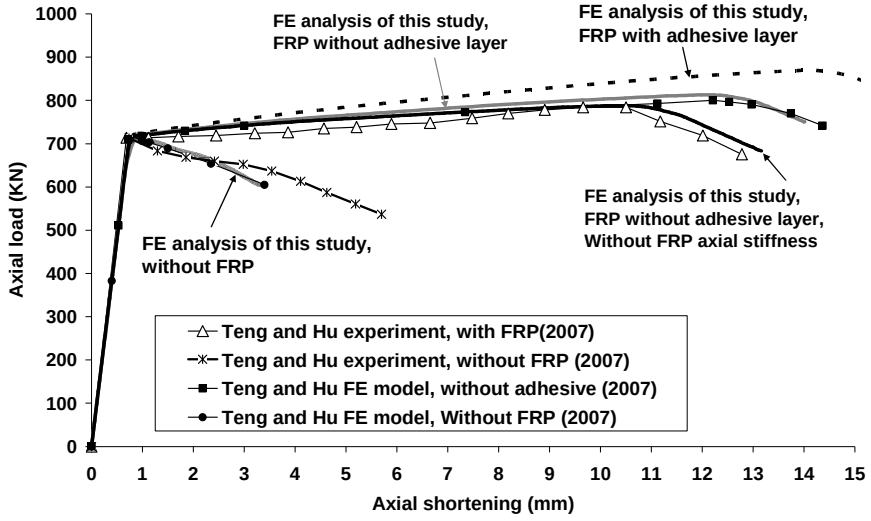

Fig. 6-10: Load-axial shortening curves.

The predictions shown in Fig. 6-10 are found by using the S4R shell element. The result is very similar to that obtained using the SAX1 axisymmetric shell element which was shown in Fig. 5-8. Again the collapse load is much closer to the one obtained by the experiment than that in the FE study of Teng and Hu. Moreover,

a small increase in the buckling load is evident when the FRP is separated from the shell. The predicted change that a significant adhesive layer would make to the experiment of Teng and Hu (2007) can be seen in Fig. 6-10. The extra adhesive thickness clearly has a slightly beneficial effect.

To demonstrate the strengthening effect of FRP on a thin cylindrical shell, the cylindrical shell of Section 6.3.1 with externally attached FRP was analysed. It had a Young's modulus in the circumferential direction, $E_{f\theta}$, of 230 GPa, and in the meridional direction, E_{fz}, of 3GPa, with a Poisson's ratio in the circumferential direction, $\nu_{f\theta}$, of 0.35. The results, shown in Figs 6-11 and 6-12, are compared with FRP with Young's modulus in the circumferential direction of 100GPa in terms of FRP dimensionless extensional stiffness ($E_{f\theta}t_f/E_st_s$) and FRP dimensionless bending stiffness ($E_{f\theta}t_f^3/E_st_s^3$). An imperfection with amplitude δ_0/t_s= 2 was assumed and the FRP height ratio of h_f/λ=2 was used in these calculations.

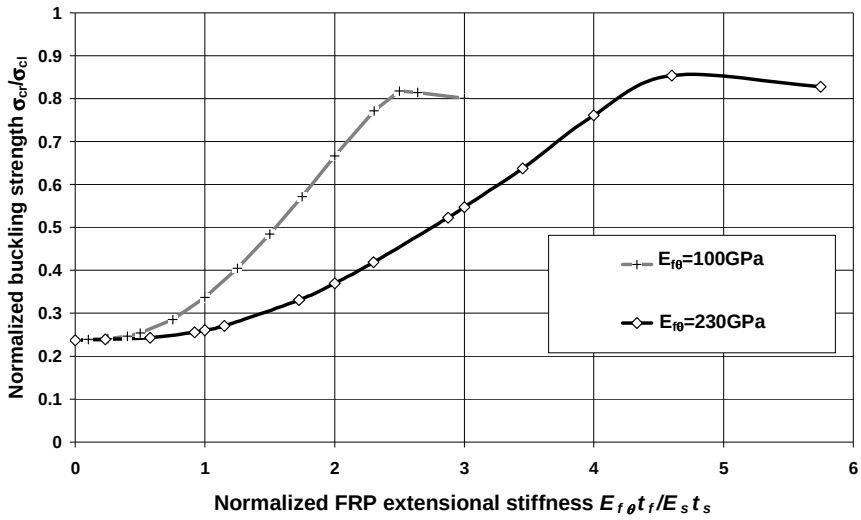

Fig. 6-11: Effect of the FRP extensional stiffness on the buckling strength of an imperfect shell (h_f/λ =2 and δ_0/t_s = 2).

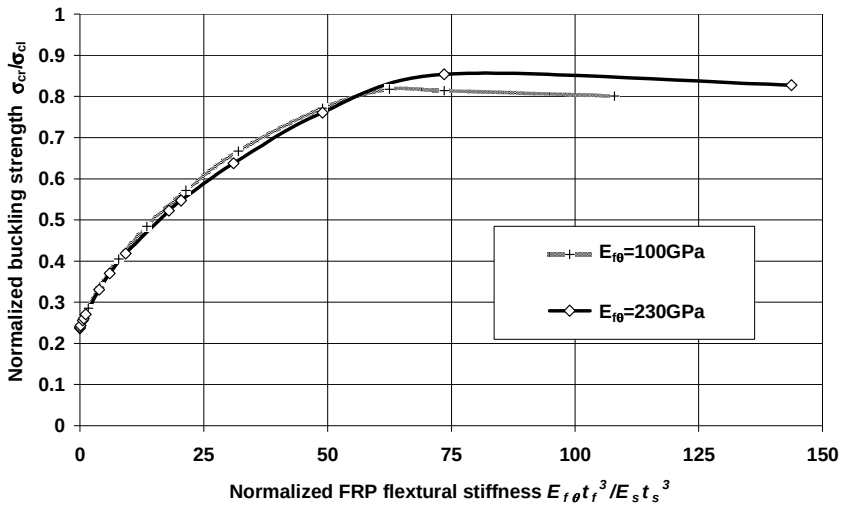

Fig. 6-12: Effect of the FRP flexural stiffness on buckling strength of an imperfect shell ($h_f/\lambda = 2$ and $\delta_0/t_s = 2$).

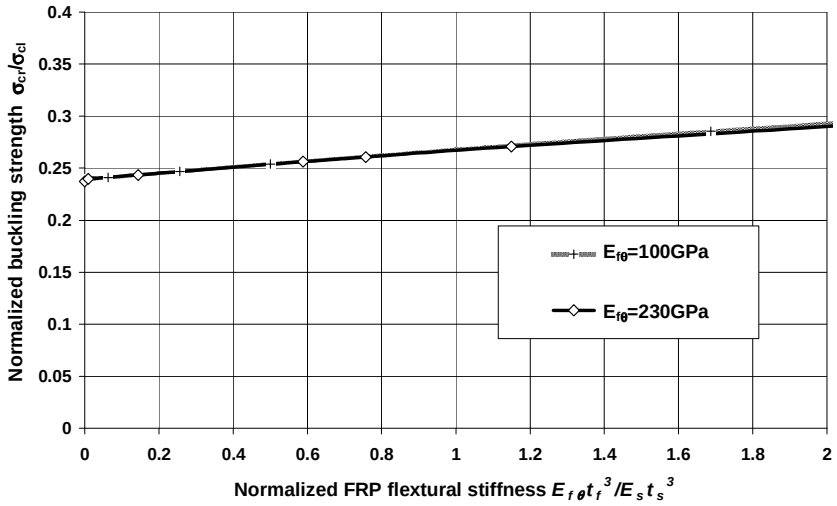

Fig. 6-13: Effect of the FRP flexural stiffness on buckling strength of an imperfect shell ($h_f/\lambda = 2$ and $\delta_0/t_s = 2$).

It is clear that the buckling load can be significantly enhanced by FRP strengthening, and this enhancement increases with the increase of the FRP stiffness. The effect of changing flexural stiffness is independent of the FRP modulus if the flexural stiffness is expressed in dimensionless form (Fig. 6-12), but this is not the case if the extensional stiffness is used. It can be concluded that the flexural stiffness governs this problem. This conclusion is natural, since the buckling phenomenon involves transfer of energy from membrane to bending in elastic buckling. In

contrast, the circumferential membrane stress resultants play a big role in the plastic collapse (Chapter 5).

The effect of the adhesive stiffness on the bifurcation buckling strength is explored in Fig. 6-14 for two adhesive Young's moduli: 1GPa and 3GPa. It is clear from Fig. 6-14 that there is a considerable increase in strength when the thickness of adhesive is increased, but this is only the case for unrealistic thicknesses (Fig. 6-14). If the gains due to changes in the normalized adhesive stiffness (Fig. 6-14) are compared with those due to changes in the FRP normalized stiffness (Fig. 6-12), it is clear that an increase in adhesive thickness is much effective in increasing the buckling strength than an increase in the quantity or stiffness of FRP. This result is to be expected, as the adhesive thickness separates the FRP from the shell and this greatly enhances the flexural stiffness of the composite shell. This phenomenon is very important in the use of FRP to enhance the buckling strength of a structure. Most studies of the use of FRP to achieve strengthening were concerned with material failure (Chapter 2), and for these conditions, effective confinement of the concrete, for example, required a thin adhesive layer between the FRP and the parent structure. Here, by contrast, a thick layer of FRP is extremely beneficial, and may be necessary for the strengthening measures to be effective.

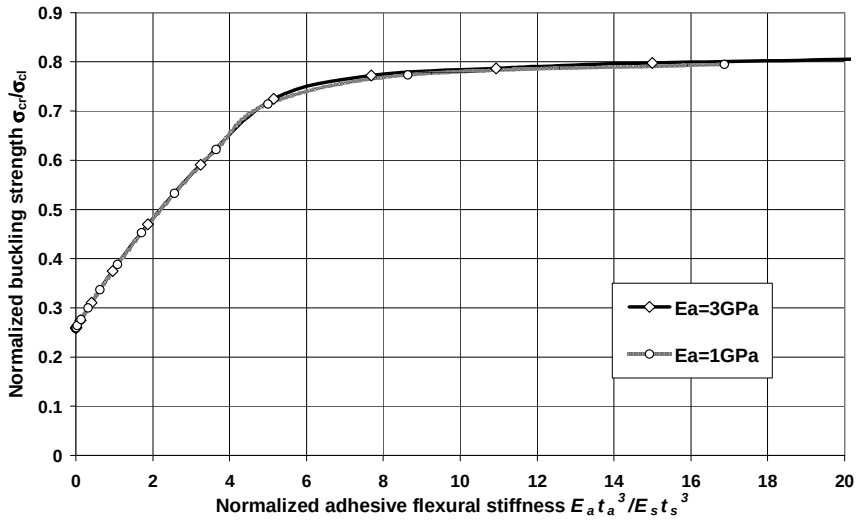

Fig. 6-14: Effect of adhesive flexural stiffness enhancement on buckling strength ($h_f/\lambda = 2$, $E_{f\theta}t_f^3/E_s t_s^3=0.76$ and $\delta_0/t_s = 2$).

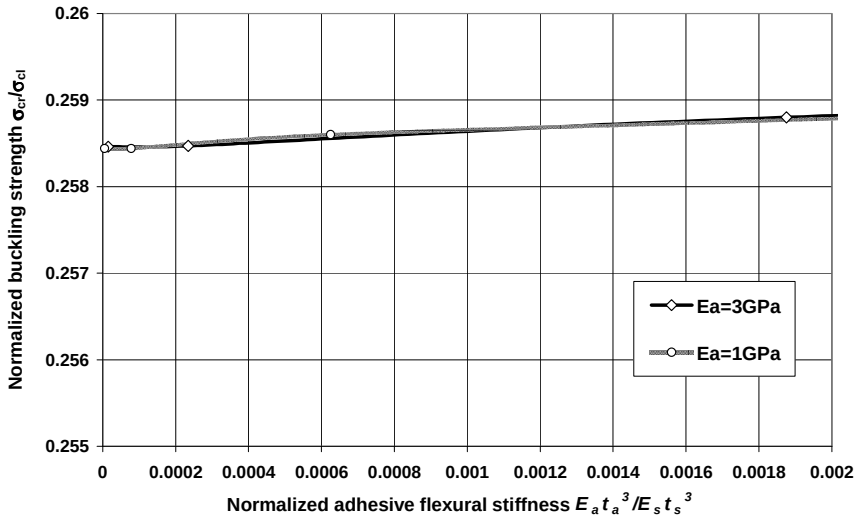

Fig. 6-15: Effect of adhesive flexural stiffness enhancement on buckling strength (h_f/λ = 2, $E_{f\theta}t_f^3/E_st_s^3$=0.76 and δ_0/t_s = 2).

The axial stress-axial shortening curves for the example shell with and without FRP strengthening are shown in Fig. 6-16 for three different FRP normalized flexural stiffnesses with the height ratio of h_f/λ=2. The moduli $E_{f\theta}$ and E_{fz}, and $\nu_{f\theta}$ for the unidirectional FRP were taken as 230GPa, 3GPa and 0.35 respectively. In addition, the adhesive had a thickness t_a of 1mm with Young's modulus E_a=3GPa and Poisson's ratio ν_a=0.35. As presented earlier, Fig. 6-16 shows a considerable increase in buckling strength by increasing the FRP normalized flexural stiffness.

If the value of the FRP normalized flexural stiffness is fixed at $E_{f\theta}t_f^3/E_st_s^3$=6, the buckling strength is increased when the FRP height of FRP is increased up to a height ratio of 10, as shown in Fig. 6-17.

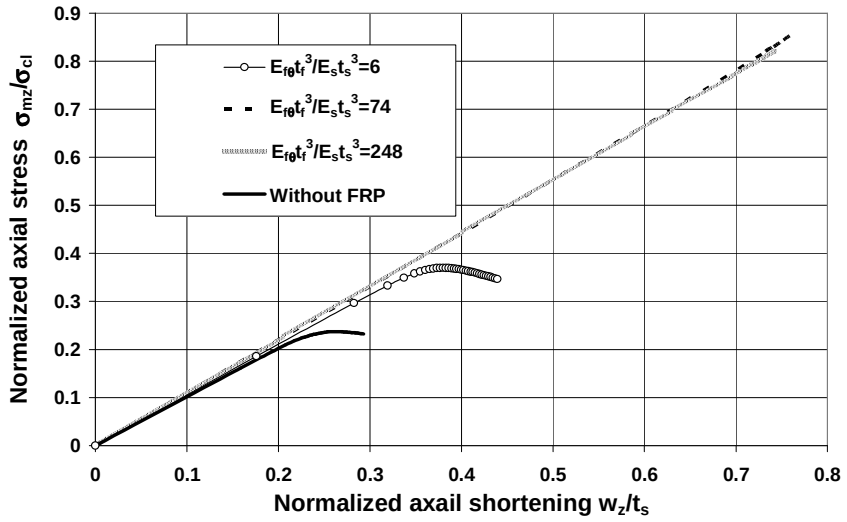

Fig. 6-16: Effect of FRP normalized flexural stiffness on axial stress- axial shortening curves (h_f/λ=2, δ_0/t_s=2).

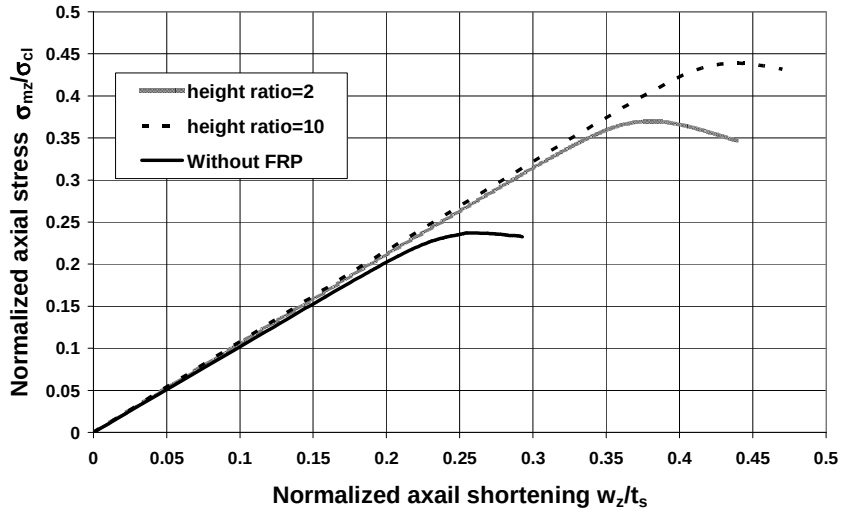

Fig. 6-17: Effect of FRP height ratio on axial stress- axial shortening curves ($E_{f\theta}t_f^3/E_st_s^3$=6 and δ_0/t_s=2).

The effect of the FRP flexural stiffness on shells with different imperfection amplitudes is shown in Figs 6-18 and 6-19. Here, the FRP height h_f has been fixed at twice the bending half wavelength λ. The normalized flexural stiffness ($E_{f\theta}t_f^3/E_st_s^3$) has a strong effect on the buckling strength of the shell (Fig. 6-18). When the stiffness increases from zero, the buckling strength increases very fast initially and approaches the upper limit value for the given imperfection. Because the FRP is applied within the vicinity of the local imperfection, the overall buckling strength of the shell cannot exceed the buckling stress of a perfect shell, irrespective of the FRP

stiffness. Therefore, when the vertical dimensionless coordinate takes the value of 1.0 in Fig. 6-19, the upper limit of the buckling strength is reached. The peak achievable strength is lower than 1.0 because of the prebuckling deformations, which were explored in Section 2.2 for different boundary conditions (Fig. 2-3) (Yamaki, 1984). This peak value reduces as the imperfection amplitude increases. This effect may be explained using Fig. 6-20 which shows the imperfect shape of the shell based on Eq. 6-2 for different amplitudes. When the FRP height h_f is fixed at 2λ, as in this example, it terminates at a distance of λ on each side of the middle of the imperfection; (i.e. the FRP terminates at a vertical coordinate of 1.0 in Fig.6-20). Clearly the imperfection extends a little beyond the FRP, and the imperfection outside the FRP reduces the buckling strength even if the FRP is very stiff.

The gain in the bifurcation buckling strength shown in Fig. 6-18 and 6-19 deserve careful examinations. Each curve, for a different imperfection amplitude, begins at a different normalized buckling strength when no FRP is used. This is the consequence of the imperfection sensitivity curve shown in Fig. 6-9. However, the rate of gain in strength when FRP is attached to the shell is also very sensitive to the imperfection amplitude. If the imperfection amplitude is small (low amplitude), the shell is already strong, but a small amount of FRP further increases the strength significantly. By contrast, when the shell is very imperfect (large amplitude), much larger quantities of FRP are needed even to achieve a moderate strength gain. This suggest that the use of FRP to repair shells that fail to meet the tolerance requirements of the Eurocode on shells (Eurocode 3 Part 1.6, 2007) must be undertaken with great care to ensure that the amplitudes on the shell are not underestimated.

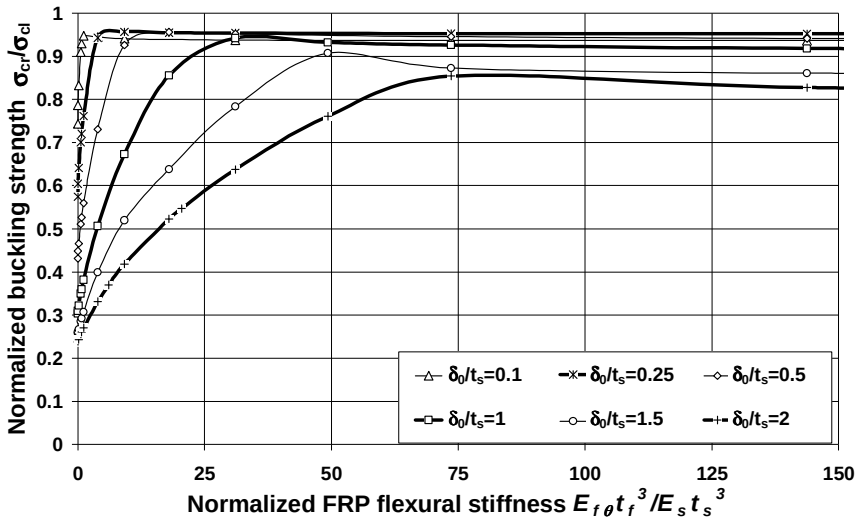

Fig. 6-18: Effect of FRP flexural stiffness on the buckling stress ($h_f/\lambda = 2$).

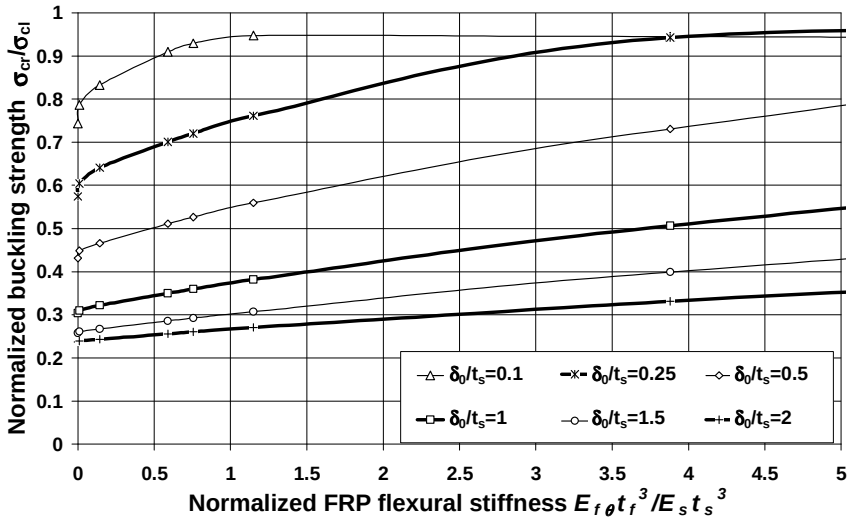

Fig. 6-19: Effect of FRP flexural stiffness on the buckling stress ($h_f/\lambda = 2$).

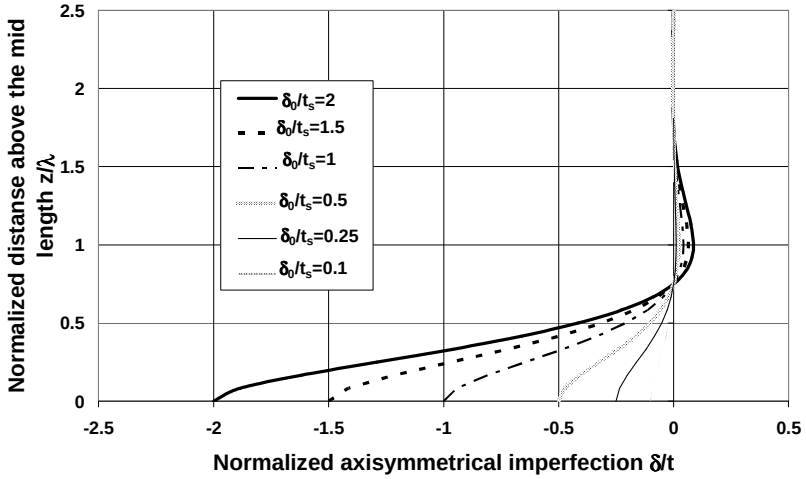

Fig. 6-20: Type A welded joint imperfection shapes.

Figure 6-21 demonstrates the buckling mode for FRP-strengthened example shell with imperfection amplitude $\delta_0/t_s=2$ as an example. Different normalized FRP flexural stiffness are shown in Fig. 6-21.

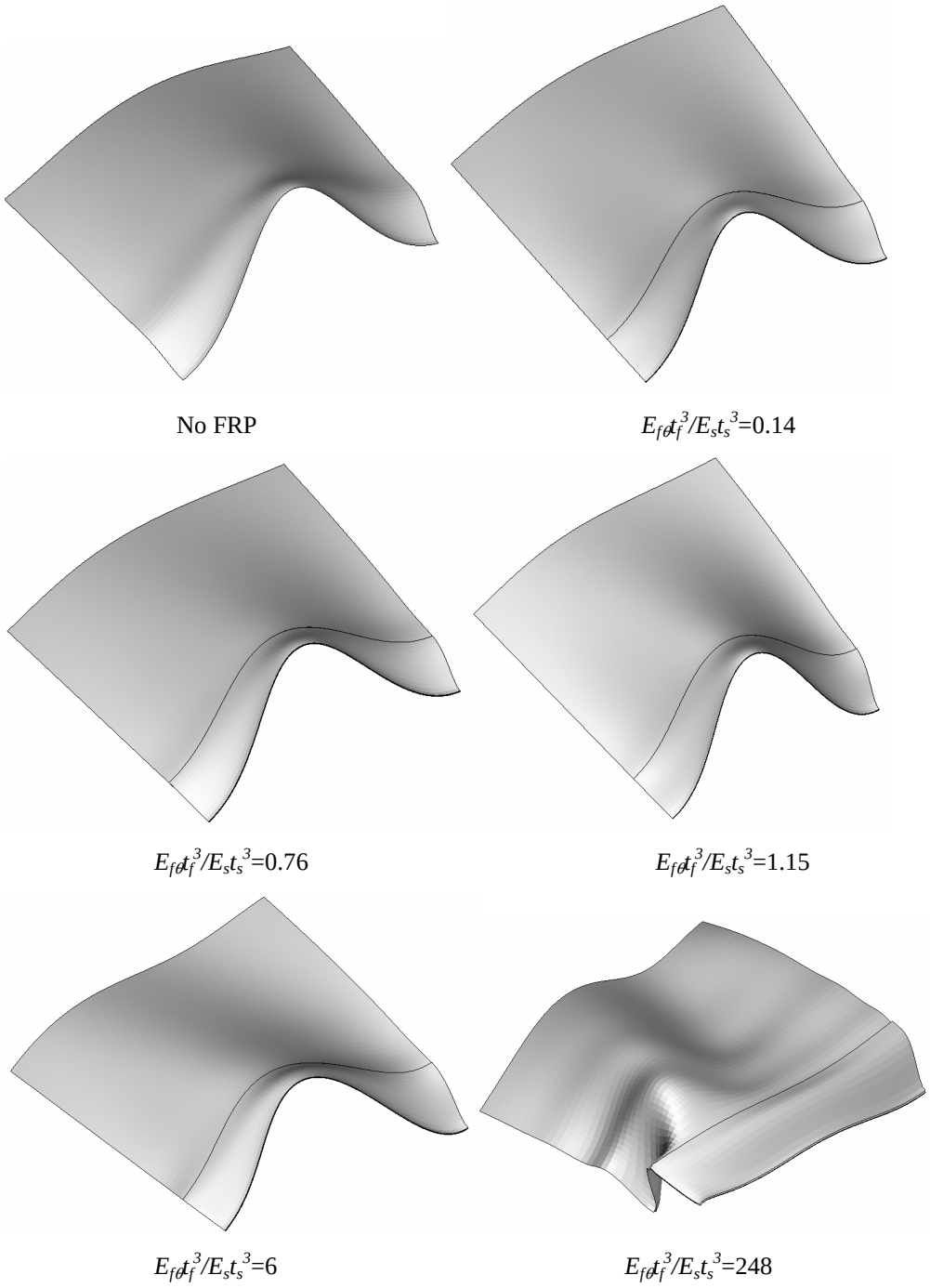

Fig. 6-21: Buckling mode for FRP-strengthened cylindrical shell ($\delta_0/t_s=2$, $h_f/\lambda = 2$)

Figure 6-21 shows that the FRP strengthened shell doesn't registered different mode from the one without FRP, but it is not the situation with a very stiff FRP strengthening (e.g. $E_{f\theta}t_f^3/E_st_s^3$=248). This result is expected since the buckling is very localized in the zone beyond the FRP sheet when the FRP flexural stiffness is too high. The meridional buckling mode is shown in Fig. 6-22.

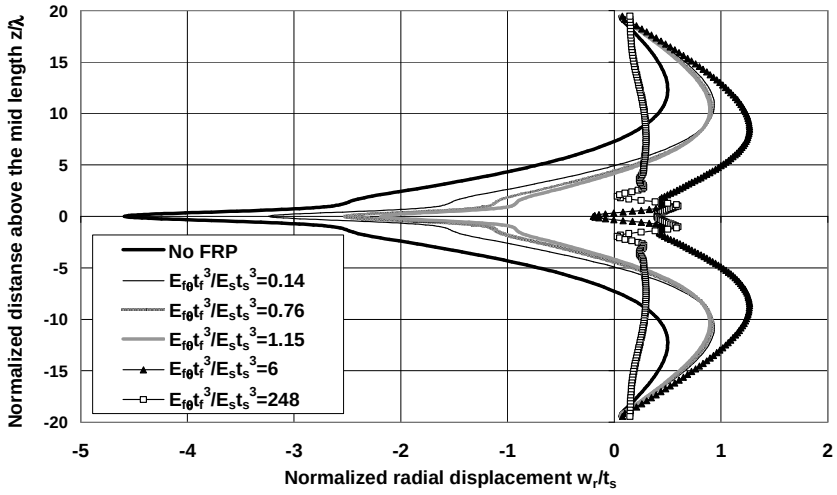

Fig. 6-22: Buckling displacements for different FRP flexural stiffness (δ_0/t_s=2, h_f/λ = 2, θ=0)

Figure 6-22 demonstrates that the buckling involves the whole shell with small FRP flexural stiffness, whereas a very localized zone above the FRP sheet is involved when a high FRP flexural stiffness is used.

To confirm the buckling mode for the strengthened cylindrical shell, the buckling strength was produced for four different normalized FRP flexural stiffness (Fig. 6-23). Figure 6-23 shows the buckling strength related to three different segments: a segment of 32.7 degrees, a segment of 30 degrees and a segment of 27.7 degrees. It is clear from Fig. 6-23b that 30^o segment produces the lowest buckling strength when the FRP sheet is not very stiff. The results shown in Fig. 6-23b confirm the conclusion noted in Fig. 6-21. Therefore, a segment of 30^o provides a good estimation about the buckling of strengthened cylindrical shell with normalized imperfection amplitude δ_0/t_s=2. Figure 6-23a demonstrates that the buckling mode changes with very stiff FRP sheet. This is reasonable since the buckling occurs in the zone beyond the FRP (Fig. 6-21). It is important to be noted that 30^o segment complies to 12 buckling mode for the full circle.

a)

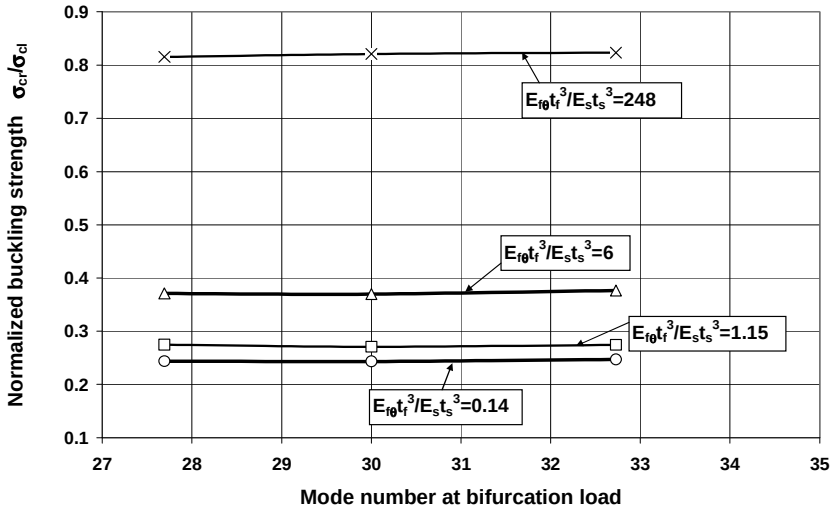

b)

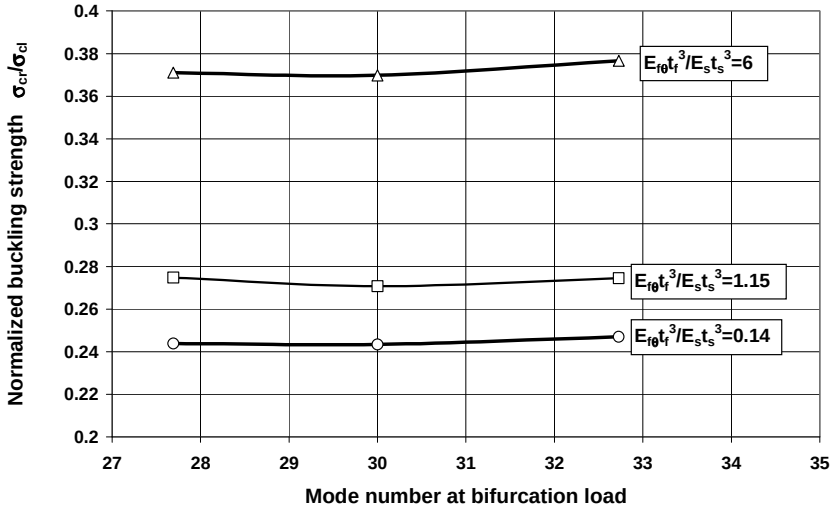

Fig. 6-23: The normalized buckling strength against the buckling mode (δ_0/t_s=2, h_f/λ = 2).

The effect of the normalised height h_f/λ of the FRP on the buckling strength of the example shell is shown in Figs 6-24 and 6-25 for an imperfection amplitude of δ_0/t_s=2.

The height ratio clearly has a remarkably strong effect on the buckling strength, even at relatively low FRP flexural stiffness values. When the FRP extends far beyond the imperfection (e.g. a height ratio of 10), an increase in height still increases the buckling strength. The reason is not immediately obvious, but a study of the axial mode with changing imperfection amplitude (Rotter, 2004) shows that

deep imperfection (here δ_0/t_s=2) lead to very large buckles in the axial direction. As a result, although the imperfection is local, if it is deep the repair may need to extend over a much greater zone than the imperfection itself.

As the height of the FRP is increased, once again peak strength is reached for a finite amount of FRP. The reason for the limitation was given earlier. However, it is interesting to note that increasing the amount of FRP beyond the optimum value leads to a reduction in strength, though not to the dramatic effect seen for elephant's foot buckling in Chapter 5.

The imperfection sensitivity of FRP strengthening shells with a fixed amount of FRP was explored next. The normalised FRP flexural stiffness was fixed to a practical value of $E_{f\theta}t_f^3/E_st_s^3$=0.76. The result is shown in Figs 6-26 and 6-27. Little gain in buckling strength can be achieved by increasing the FRP height ratio beyond 4, especially when the imperfection amplitude is small. This finding matches the previous description which related the FRP height to the buckle size.

If a large quantity of FRP is used, the buckling strength reaches, and passes, a peak value. The reason for the decline in strength for higher FRP flexural stiffnesses is that the termination of the FRP causes a more serious imperfection than the repaired one, as was seen in Chapter 4. This effect is demonstrated in Fig. 6-28 where large heights of FRP lead to axisymmetric buckling beyond the repaired zone.

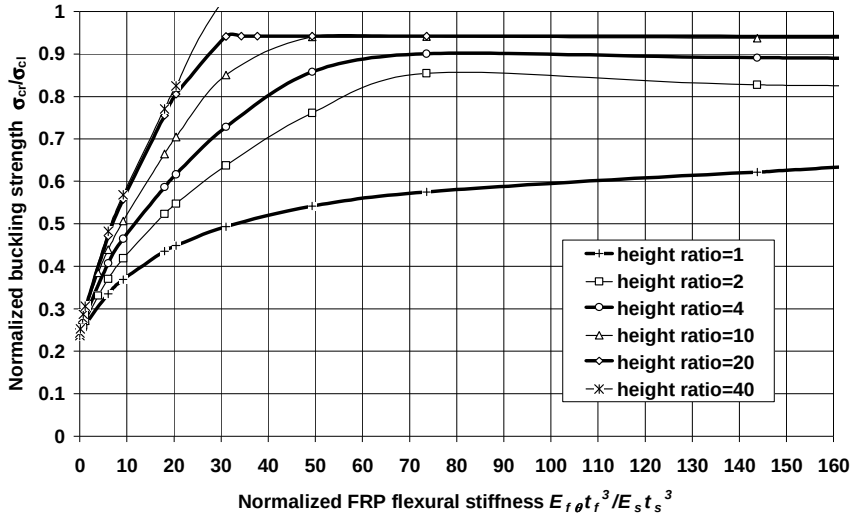

Fig. 6-24: Buckling strength for different FRP height and flexural stiffness values (δ_0/t_s = 2).

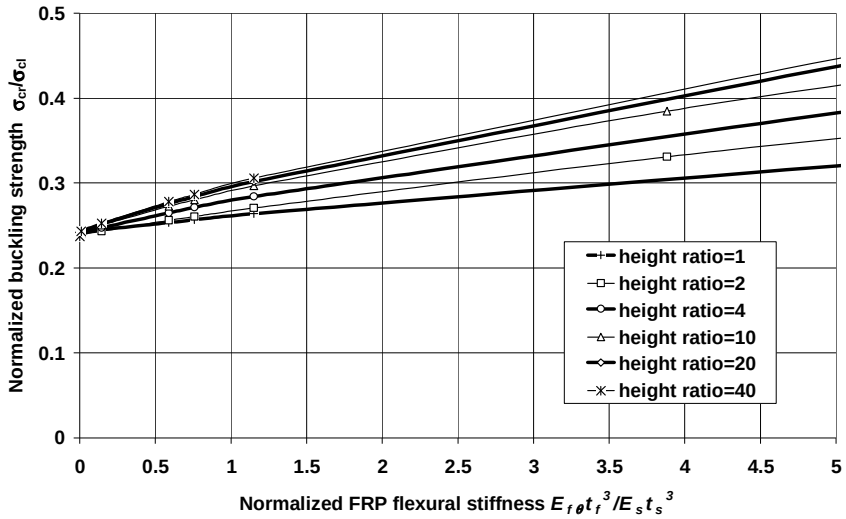

Fig. 6-25: Buckling strength for different FRP height and flexural stiffness values ($\delta_0/t_s = 2$).

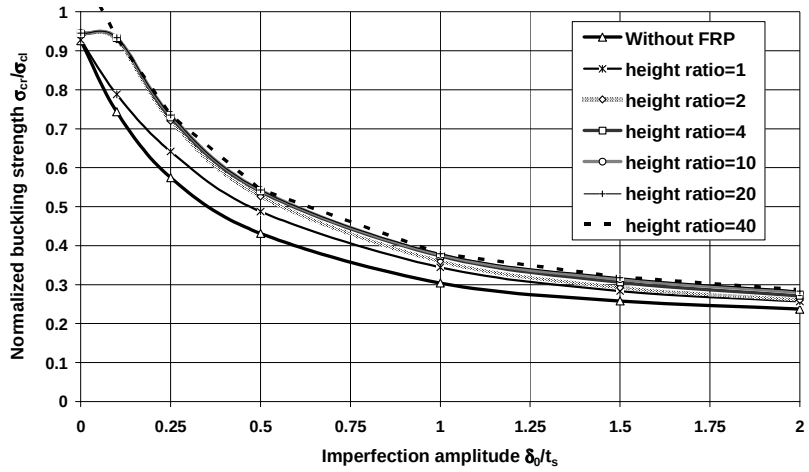

Fig. 6-26: Effect of imperfection amplitude on buckling strength for different FRP heights ($E_{f\theta}t_f^3/E_st_s^3=0.76$).

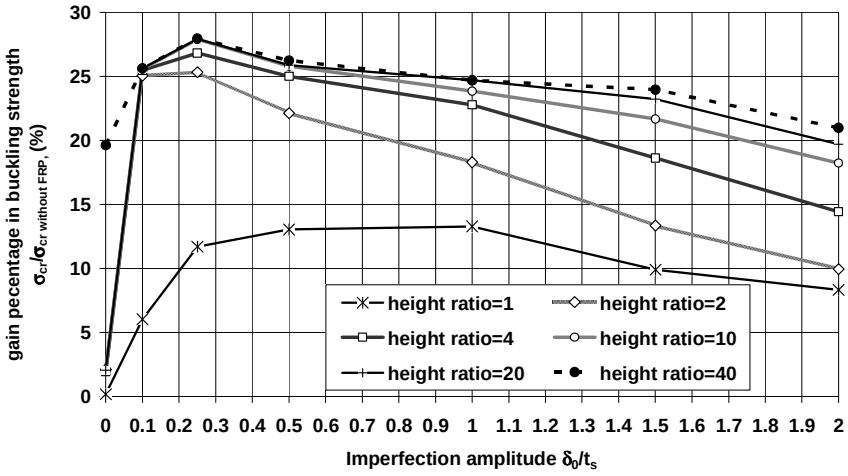

Figure 6.27: The gain percentage in buckling strength ($E_{f\theta}t_f^3/E_st_s^3=0.76$).

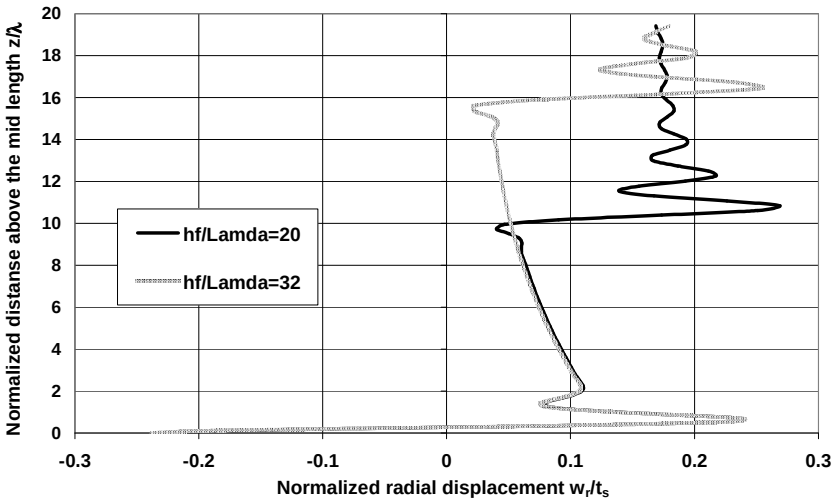

Figure 6.28: Buckling displacements for different height ratio ($E_f t_f^3/E_s t_s^3$=73.6 and δ_0/t_s=2).

6.5 Summary

This chapter has presented an initial study of the elastic buckling of FRP-strengthened cylindrical shells with an axisymmetric local inward imperfection. The buckling strength was calculated Using Geometrically Nonlinear Analysis with Imperfections (GNIA). The effects of the amplitude of the imperfection, the FRP stiffness and the FRP height were investigated. The results have shown that the buckling strength can be significantly increased by bonding FRP within a zone that relates to the size of the potential buckles, rather than to the zone of the imperfection. It has shown that the thickness of the adhesive layer plays a more important role than the amount of FRP and that an extensive zone of strengthening may be needed if the local imperfection has a large amplitude. Nevertheless, the proposed technique could be a very effective and economical method of strengthening shells that are too imperfect to meet the tolerance limits required by EN 1993-1-6 (2007).

Chapter 7

Using FRP in strengthening the elastic buckling of thin metallic cylinders with a single local dent

7.1 Introduction

The greatest cause of concern in a thin metal cylinder is often the presence of a single local deep dent. A single dent of this kind can cause the tolerance requirements to be missed, even though most of the shell is of good quality. Thus strengthening a single dent by using FRP is potentially an extremely valuable and cost-effective remedial measure.

This chapter addresses the strengthening of a cylindrical shell with a single local dent against elastic buckling. Very few studies have explored the effect of a single local dent in a cylinder, though such an imperfection may easily be produced either during construction or in service as a result of an accidental impact.

The problem is explored using a Geometrically Nonlinear Analysis with Imperfections (GNIA).

An extended detailed study is performed of the strength of thin cylindrical shells with local dents of different sizes, shapes and depths. This study of the buckling of unstrengthened isotropic cylinders is believed to be the first of its kind, and is performed to identify the most damaging forms of local dents. This study has implications for tolerance measurement methods as well as for repair requirements.

The use of FRP to enhance the strength of a cylinder with a local dent is then explored, with a focus on the use of small quantities of FRP placed strategically to achieve the best results.

Finally, a summary of the work of this chapter is given.

7.2 Finite element analysis procedures

7.2.1 Geometry, boundary conditions, material properties and loading

An example cylindrical shell with the following properties was used in this study. The shell had a height h=3000mm, radius R=1000mm and constant thickness t_s=1mm. This gives a radius to thickness ratio of R/t=1000, and corresponds to a medium length cylinder according to Eurocode 3 Part 1.6 (2007). The shell was assumed to be made of an isotropic metal with Young's modulus E_s=200 GPa and Poisson's ratio ν_s = 0.3. The shell was subjected to a uniform axial load, resulting in a uniform compressive membrane stress σ_z throughout the shell. The boundary conditions at both ends were free in all directions except for both rotation about the circumference and the circumferential displacement. These boundary conditions correspond to a shell that continues far beyond the boundary.

To define the assumed imperfection, the vertical coordinate z was taken with its origin at the mid-height of the shell. The imperfection was taken as a single rectangular inward dent centred at the origin and of the form:

$$\delta = \delta_0[e^{-\pi z / L_z}\cos(\pi z / L_z)][e^{-\pi y / L_\theta}\cos(\pi y / L_\theta)] \qquad (7\text{-}1)$$

in which δ is the local radial deviation from the perfect cylindrical shape at (θ, z), δ_0 is the characterising amplitude of the imperfection (value at the centre of the dent), y is the circumferential coordinate from the centre of the dent with $y=R\theta$, L_z is the half wavelength characterising the height and L_θ the half wavelength characterising the width of the rectangular dent. The dent of Eq. 7-1 extends indefinitely, leading to smooth transitions between the local dent and the remaining perfect shell.

7.2.2 FE modelling

One half of the complete shell ($0 \leq \theta \leq 180°$) was modelled in ABAQUS (Version 6.5-4) using shell elements S4R, as described in Section 5.4. The analysis included geometric nonlinearity but assumed perfectly elastic behaviour since the stress levels at buckling are very low. Thus the analysis was a Geometrically Nonlinear elastic Analysis with explicit modelling of Imperfections, known as GNIA in Eurocode 3 (EN 1993-1-6, 2007). The bifurcation load was considered a reasonable limit for this problem, for the reasons identified in Section 6.3.2.

A mesh convergence study was conducted for an example shell with a square dent $L_z=L_\theta=5\lambda$ and a dent amplitude $\delta_0/t_s=2$, where λ is the linear bending half wavelength (Eq. 2-3). In order to determine the required circumferential refinement, a constant number of 50 rows was assumed and the number of the circumferential columns was increased gradually. The change in the bifurcation stress caused by increasing the number of circumferential columns is shown in Fig. 7-1.

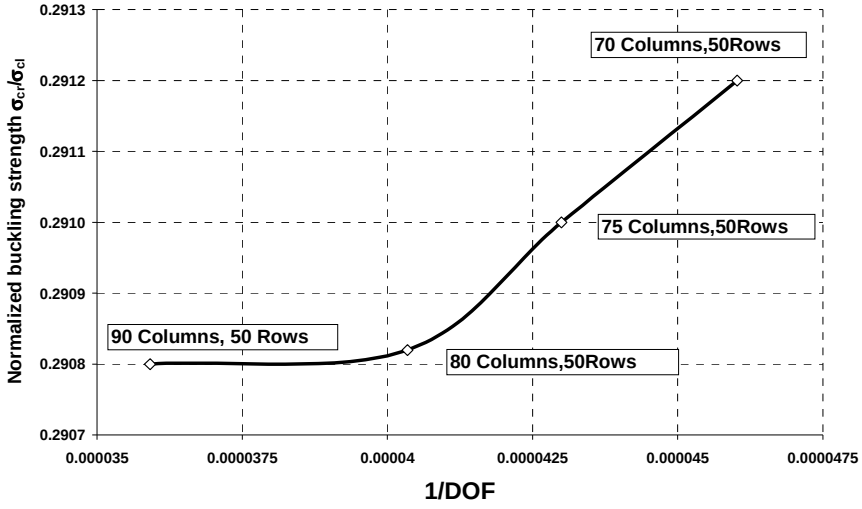

Fig. 7-1: Circumferential mesh convergence study for the imperfect shell.

From Fig. 7-1, it can be seen that the mesh of 80 elements around the half circumference is sufficiently accurate for this study. The second step is to find an adequate mesh down the meridian. For this study, a mesh of 80 columns was fixed and the number of rows was changed (Fig. 7-2). Both the rows and columns were generated by using the BIAS command of ABAQUS. This command allows the

nodes to be more concentrated towards one edge, so that a very fine finite element mesh in the neighbourhood of the initial dent can be obtained.

Based on the convergence study, a mesh of 100 rows down the meridian and 80 columns around the half circumference was chosen as adequate. This means that element sizes of $0.16\sqrt{Rt_s}$ in the circumferential direction and $0.2\sqrt{Rt_s}$ in the meridional direction within and near the dent were adopted for good predictions. It may be noted that Rotter and Teng (1989) used an element size of $0.25\sqrt{Rt_s}$ for their cubic isoparametric element. Further, Gavrilenko and Krasovskii (2004) used a mesh size of $\sqrt{Rt}$ in the circumferential and $0.53\sqrt{Rt}$ in the meridional direction for their Finite Difference Method (FDM) study of a cylinder with a square dent. Later, Gavrylenko (2007) reduced the circumferential mesh size to only $0.52\sqrt{Rt}$.

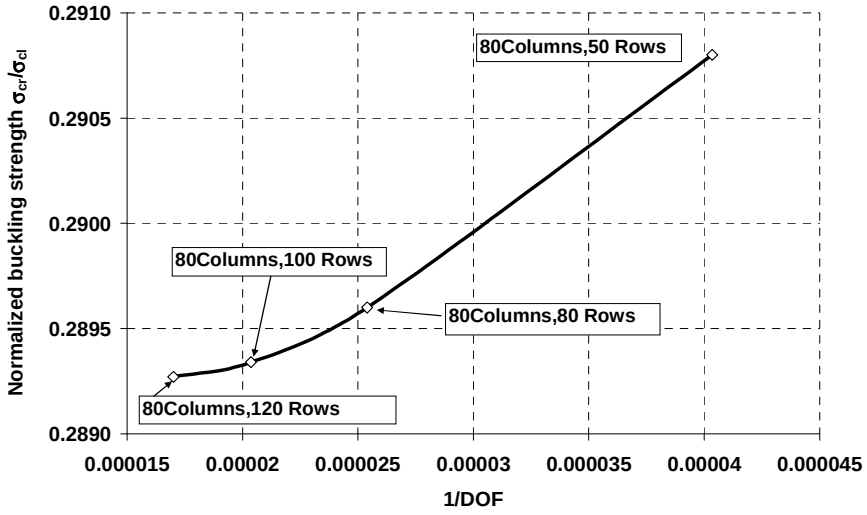

Fig. 7-2: Mesh convergence study for the imperfect shell in meridian.

7.3 Previous experimental study and comparison

Gavrilenko and Krasovskii (2004) recently examined the stability of a thin cylindrical shell with a single square local dent. Experimental work and numerical calculations were performed for three different radius to thickness ratios, *R/t*=150, 260 and 360.

To verify the model of the present study, a comparison with the investigations conducted in Gavrilenko and Krasovskii (2004) was undertaken for a radius to

thickness ratio of 360. A cylindrical metal shell with radius R of 1000 mm and thickness t_s of 2.78 mm was studied with Young's modulus E_s of 191GPa and Poisson's ratio ν_s of 0.32 (these were the values reported by Gavrilenko and Krasovskii (2004)). The boundary conditions at both ends were chosen as simple supports, except for free displacement in the axial direction. Different square dent dimensions, L_{sq}, were considered as shown in Table 7-1. The bifurcation buckling strength of the cylindrical shell was calculated for four different imperfection forms identified here by 2D-A for the 2D Type A form (Eq. 7-2), HC for the bi-directional half cosine form (Eq. 7-3), CB for the complete chequerboard square pattern all over the shell (Eq. 7-4) and Gav for the pattern chosen by Gavrylenko (2007) (Eq. 7-5).

$$\delta = \delta_0 [e^{-\pi z / L_{sq}} \cos(\pi z / L_{sq})][e^{-\pi y / L_{sq}} \cos(\pi y / L_{sq})] \tag{7-2}$$

$$\delta = \delta_0 \cos(\pi z / L_{sq}) \cos(\pi y / L_{sq}) \text{ with } \begin{cases} -\frac{L_{sq}}{2} \le z \le \frac{L_{sq}}{2} \\ -\frac{L_{sq}}{2} \le y \le \frac{L_{sq}}{2} \end{cases} \tag{7-3}$$

$$\delta = \delta_0 \cos(\pi z / L_{sq}) \cos(\pi y / L_{sq}) \tag{7-4}$$

$$\delta = \delta_0 \cos(\pi z / L_{sq}) \left[\cos(\pi y / L_{sq}) - \cos(3\pi y / L_{sq})\right] \text{with} \begin{cases} -\frac{L_{sq}}{2} \le z \le \frac{L_{sq}}{2} \\ -\frac{L_{sq}}{2} \le y \le \frac{L_{sq}}{2} \end{cases} \tag{7-5}$$

Table 7-1: The dimensions of the local single square dent

Normalized initial dent depth, δ_0/t_s	Normalized dent dimension, L_{sq}/λ
0.2	2.15
0.3	2.15
0.4	2.15
0.8	2.15
2	3

The buckling strengths calculated as part of this verification are shown in Fig. 7-3, where σ_{cl} is the classical buckling stress (Eq. 2-1).

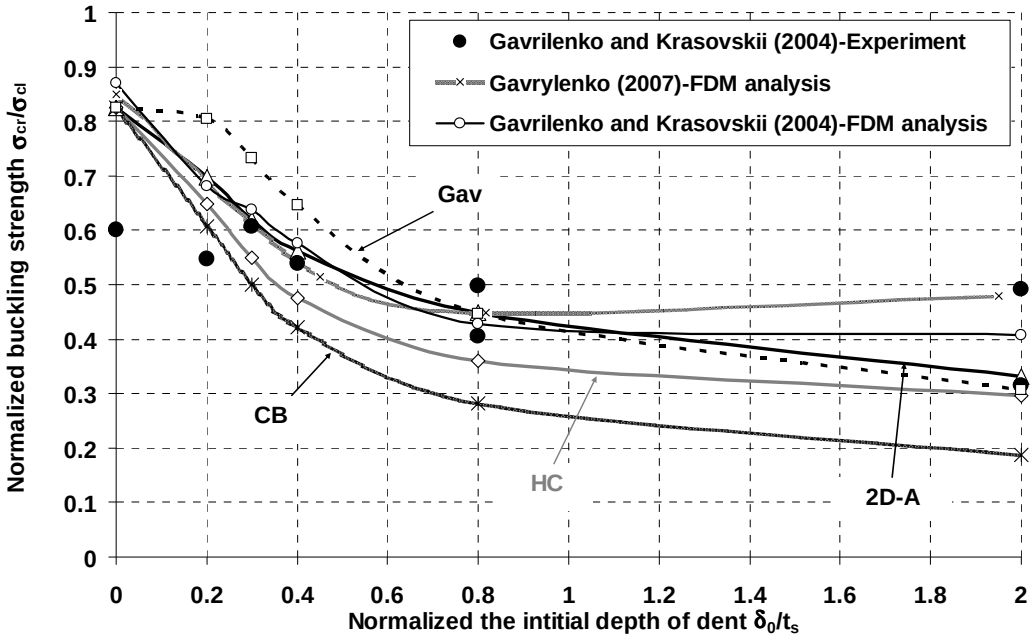

Fig. 7-3: Variation of buckling strength with different dent dimensions.

No single analysis gives a good match to the experiments, especially at small imperfection amplitudes: this suggests that either the tests were affected by other imperfections (e.g. non-uniform loading on the boundary) or that the description of the imperfection is incomplete.

The two finite difference calculation of Gavrilenko and Krasovskii (2004) and Gavrylenko (2007) are quite different, and neither match the current finite element predictions using their imperfection form. It may be that their finite element difference meshes were not sufficiently refined, but it is difficult to verify this idea.

As may be expected, the chequerboard imperfection CB all over the shell gives the lowest strengths. The half cosine HC gives lower strength than the two dimensional weld depression 2D-A, and this may be caused by the extended zone of deep dent given by a cos curve, coupled with the abrupt changes of slope (discontinuities) at its edges. It is unclear whether this can be as a realistic imperfection form.

The buckling strength of the FE analysis of the present study using the 2D-A dent shape is in much closer agreement with the test results than the three others. Although the shell strength of HC and CB forms is lower than the 2D-A form, it appears that these two dent forms probably cannot easily occur in practical

structures. Teng and Rotter (1992) stressed that the transition from the imperfect to the perfect shell must be accomplished smoothly, as the function given by Eq. 7-2. Moreover, the FE analysis using the 2D-A form provides a buckling strength which is very similar to a lower bound on the experiment for δ_0/t_s=2. Thus the 2D-A form by Eq. 7-2 provides a dent form which fits the experiments and is adopted for the remainder of this study.

7.4 Buckling of unstrengthened cylinders with a Dent

Since the problem of shell buckling in the presence of a local dent has not previously been explored in depth, the unstrengthened imperfect isotropic elastic cylinder was investigated first using the 2D-A dent form. Two shapes of dent zone were considered: square and rectangular.

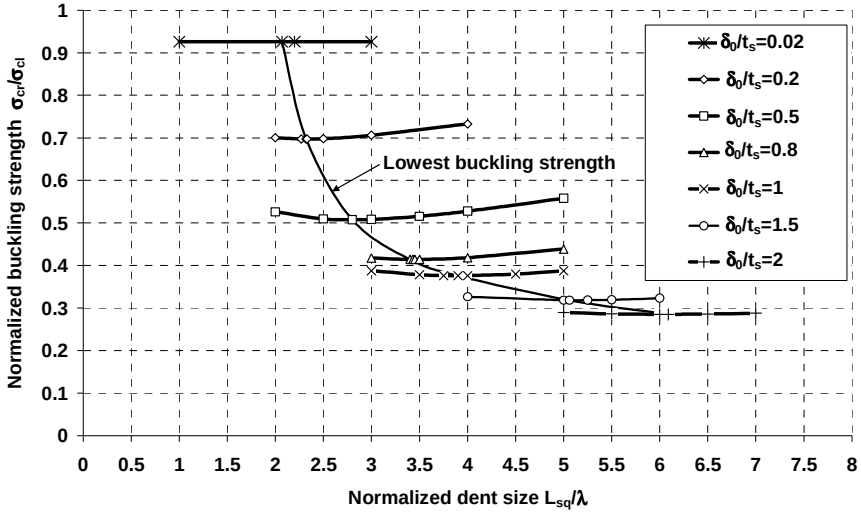

Fig. 7-4: Effect of square dent dimension on buckling strength.

First the effect of dent size, for a given dent depth, was explored for square dents. The effect of the size L_{sq} of a square dent on the elastic buckling strength is shown in Fig. 7-4.

For any given imperfection amplitude (dent depth), the buckling strength is weakly dependent on the size of the dent, with a shallow minimum strength for a well-defined size. This size at the minimum strength increases as the imperfection amplitude increases, in the same manner as was found for axisymmetric imperfections by Rotter (2004).

The critical dent size L_{sq} for each amplitude may be expressed approximately as:

$$\frac{L_{sqm}}{\lambda} = 0.7 + 1.34e^{\delta_0 / t_s} \cos(\frac{\delta_0}{2t_s}) \tag{7-6}$$

The values derived from the FE analysis and the fitted curve of Eq. 7-6 are both shown in Fig. 7-5.

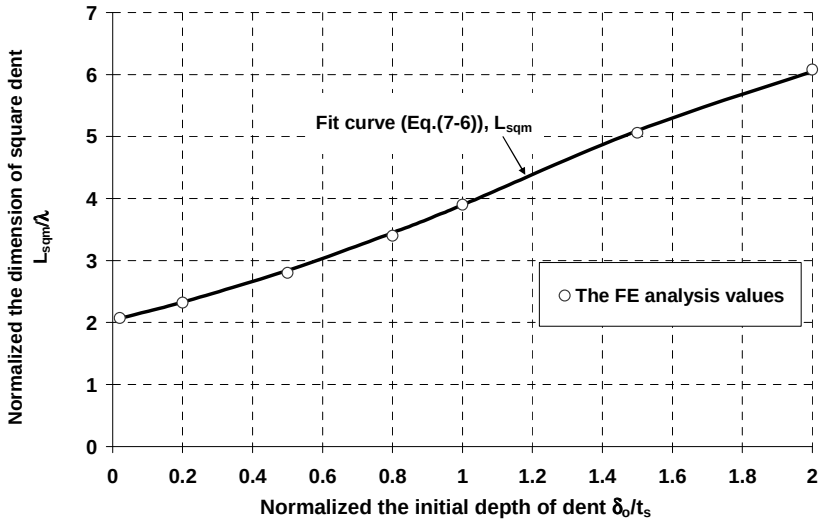

Fig. 7-5: Variation of square dent dimension with initial dent.

The effects of rectangular dents of various sizes and aspect ratios were investigated next. The characterising dimension of the dent in the circumferential direction L_θ was fixed to be equal to the dimension of the critical square dent L_{sqm} (Eq. 7-6), while the dimension down the meridian L_z was changed gradually. The variation of the buckling strength for different dent amplitudes, δ_0, and heights L_z are shown in Fig. 7-6. The same procedure was repeated in Figs. 7-7 and 7-8 for dent width, L_θ, of $2L_{sqm}$ and $3L_{sqm}$ respectively. The same conclusion was reached as for the square dent: a critical dent height L_z was found for each amplitude which minimises the buckling strength for each of the three different dent widths, L_θ. Empirical formulas for the dent height which leads to the lowest buckling strength for a specified dent width are given by Eqs. 7-7, 7-8 and 7-9.

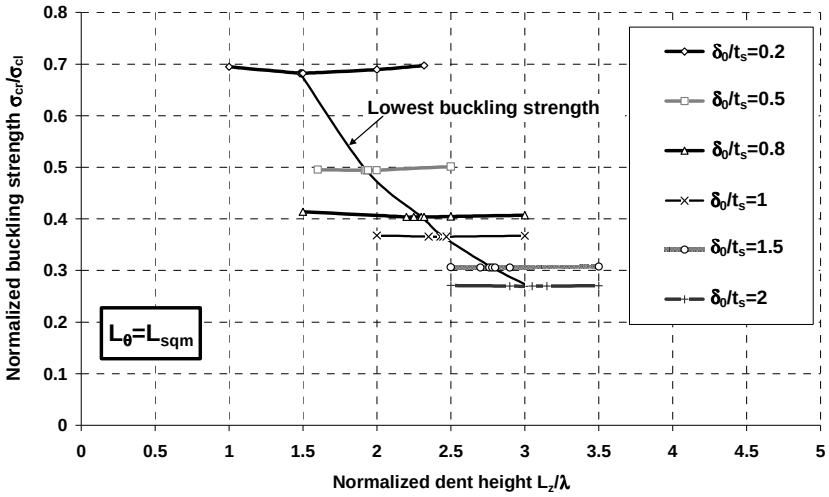

Fig. 7-6: Effect of rectangular dent height on buckling strength (L_θ=L_{sqm}).

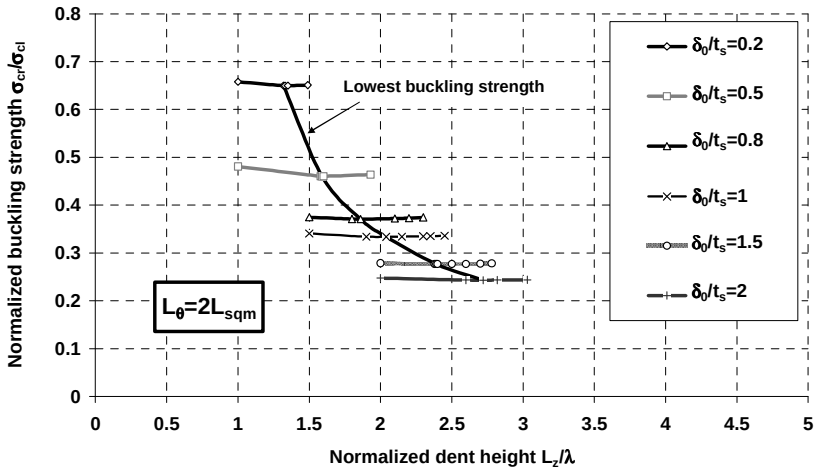

Fig. 7-7: Effect of rectangular dent height on buckling strength (L_θ=2L_{sqm}).

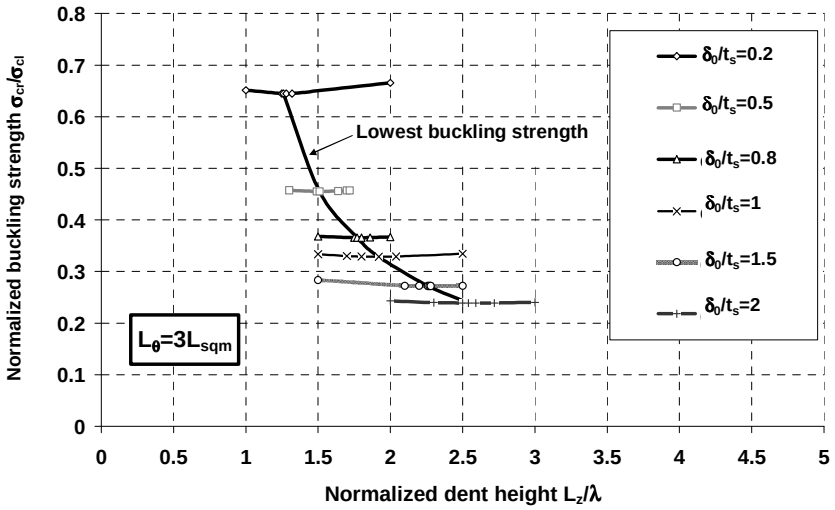

Fig. 7-8: Effect of rectangular dent height on buckling strength (L_θ=3L_{sqm}).

$$\frac{L_z}{\lambda} = 3.4 - 2.3e^{-0.9\frac{\delta_0}{t_s}} \qquad \text{For } L_\theta = L_{sqm} \tag{7-7}$$

$$\frac{L_z}{\lambda} = 4.7 - 3.6e^{-0.3\frac{\delta_0}{t_s}} \qquad \text{For } L_\theta = 2L_{sqm} \tag{7-8}$$

$$\frac{L_z}{\lambda} = 4.36 - 3.3e^{-0.3\frac{\delta_0}{t_s}} \qquad \text{For } L_\theta = 3L_{sqm} \tag{7-9}$$

The critical dent dimensions given by Eqs 7-7, 7-8 and 7-9 lead to buckling modes corresponding to the Koiter circle (Fig. 7-9), (Koiter, 1945; Calladine, 1983; Spagnoli, 2003).

Both the FE analysis values and the empirical fit curves of Eqs 7-7, 7-8 and 7-9 are shown in Fig. 7-10. In addition, the minimum buckling strength for each case of changing L_θ is demonstrated in Fig. 7-11.

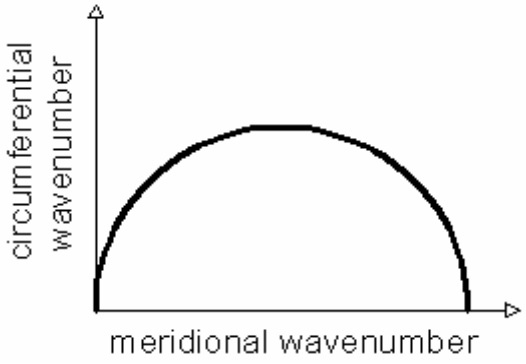

Fig. 7-9: Koiter circle for axially compressed cylindrical shell (Spagnoli, 2003).

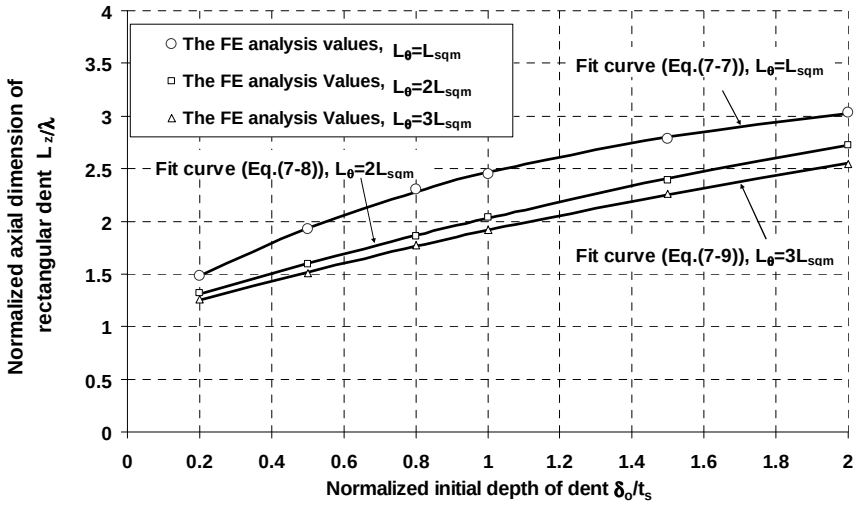

Fig. 7-10: Variation of axial dimension of dent with initial depth.

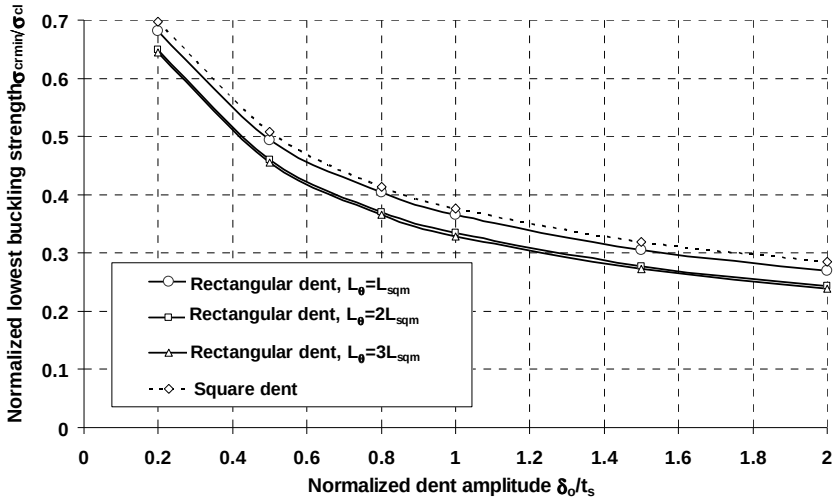

Fig. 7-11: Variation of lowest buckling strength with initial depth.

Although the effect is not very strong, it is clear from Fig. 7-11 that rectangular imperfections that are wider than their height lead to lower strength than are found for square dent. For more detail, a study was conducted to investigate the effects of both the width L_θ and the height L_z of a dent on the buckling strength when the amplitude δ_0 is equal to the shell thickness t_s (Fig. 7-12).

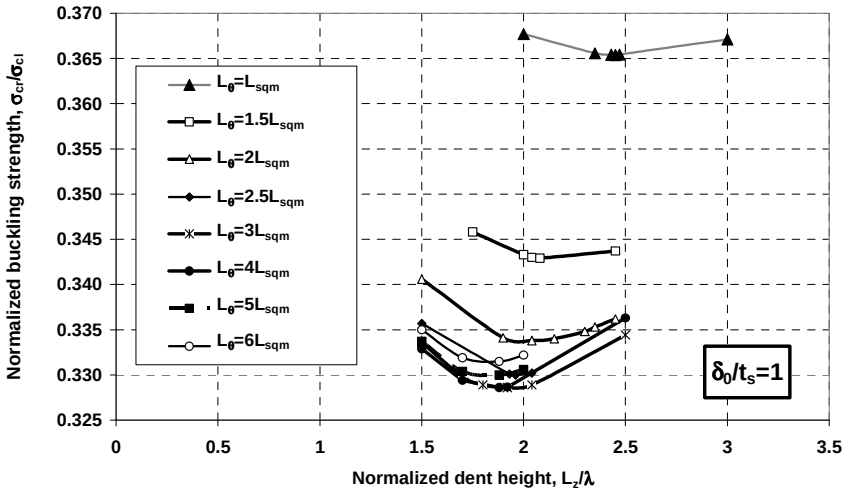

Fig. 7-12: Effect of rectangular dent dimensions on buckling strength (δ_0/t_s=1).

For each dent width L_θ, there is a clear but weak minimum in the buckling strength for a particular dent height L_z. This critical height is greater when the dent is square and reduces slightly as the dent becomes wider ($L_\theta > L_{sqm}$). The lowest

strengths of all are found when the width is about $L_\theta=3L_{sqm}$ and the height about $L_z=1.9\lambda$ or $L_z=0.5L_{sqm}$. This minimum is clearly only valid for $\delta_0/t_s=1.0$. The width $L_\theta=3L_{sqm}$ is used in the remainder of the study as a critical width.

To verify the critical dimensions obtained above, comparison with the studies of Jamal *et al.* (1999, 2003) and Wullschleger (2006) were made.

Jamal *et al.* (1999, 2003) assumed a dent shape as follows:

$$\delta = \delta_0 e^{-(2z/L_z)^2}\begin{bmatrix} d_a\cos(\gamma z)\cos(\beta\gamma y) + d_b\cos(\gamma(1+\beta^2)z) \\ + d_c\cos(\gamma\beta^2 z)\cos(\beta\gamma y)\end{bmatrix} \tag{7-10}$$

in which:

β is the modal aspect ratio (axial wavelength to circumferential wavelength).

$\gamma=n/(R\beta)$, where R and n are the cylinder radius and the number of waves in the circumferential direction repectively.

d_a, d_b and d_c are coefficients linked by a relation of :

$$d_a+d_b+d_c=1 \tag{7-11}$$

This imperfection shape was used to calculate imperfection sensitivity curves for different values of d_a, d_b and d_c satisfying Eq. 7-11.

The buckling strengths for different dent amplitudes are shown in Fig. 7-13 where they are compared with the critical shape for 2D-A imperfection found in the present study (Eq. 7-1). The dent dimensions used for both the 2D-A imperfection (Eq. 7-1) and Jamal *et al*. (1999, 2003) dent form (Eq. 7-10) were the critical values ($L_\theta=3L_{sqm}$, L_z=Eq. 7-9). The parameters β and γ were chosen to correspond to a circumferential wave number of 29 for the buckling mode of the perfect cylinder given by Eq. 7-12, (Yamaki, 1983; Rotter, 2004):

$$n_{cl} \approx 0.909\sqrt{\frac{R}{t}} \tag{7-12}$$

where R and t are the radius and thickness for the cylinder respectively.

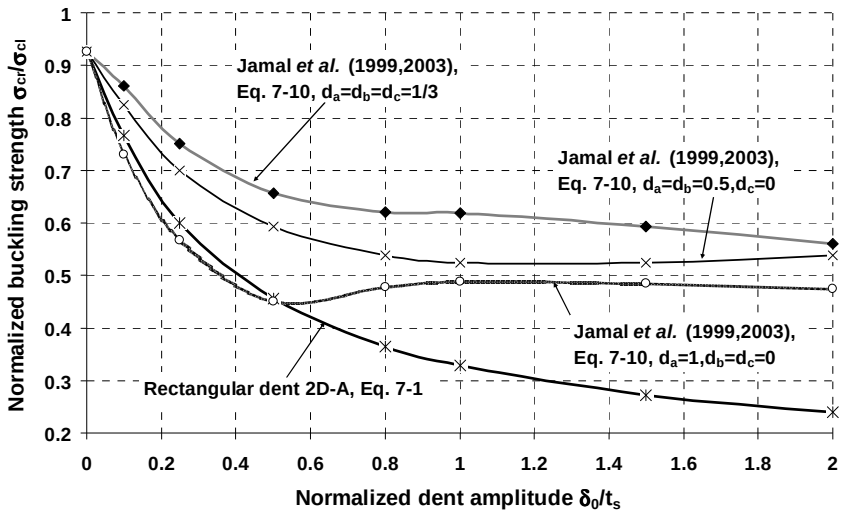

Fig. 7-13: Buckling strength for different dent amplitudes (results calculated by this study), (L_θ=$3L_{sqm}$, L_z=Eq. 7-9)

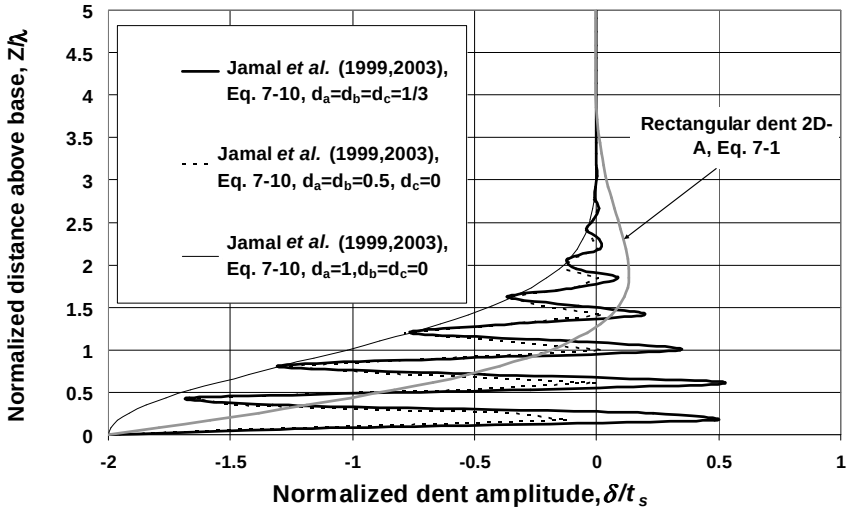

Fig. 7-14: Different dent shape in meridional direction for δ_0/t_s=2, (L_θ=$3L_{sqm}$, L_z=Eq. 7-9)

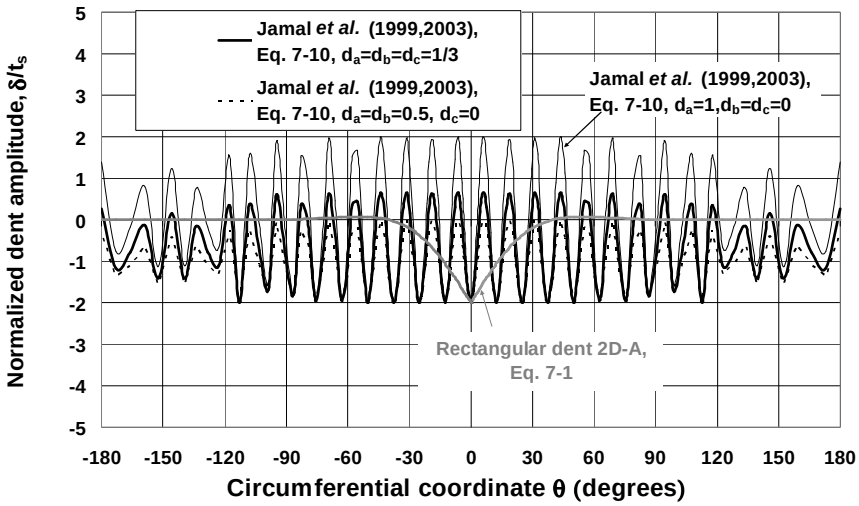

Fig. 7-15: Different dent shape in circumferential direction for $\delta_0/t_s=2$, ($L_\theta=3L_{sqm}$, L_z=Eq. 7-9)

The imperfection sensitivity curve using Eq. 7-10 varies dramatically as the coefficients d_a, d_b and d_c are changed (Fig. 7-13) to obtain different dent shapes as seen in Fig. 7-14. By examining the dent shapes shown in Fig. 7-14, it is evident that non-zero values for the parameters d_b and d_c in Eq. 7-10 produce shapes in meridional direction that are far from a realistic dent shape. In circumferential direction, using Eq. 7-10 always gives non-realistic dent shape (Fig. 7-15). However, the dent shape of the present study (Eq. 7-1) produces much lower buckling strengths than those of Jamal *et al*. (1999, 2003) for the dents of practical depth ($\delta_0/t_s>0.5$), as shown in Fig. 7-13.

Wullschleger (2006) used a dent shape given by:

$$\delta = \delta_0 \cos^2(\pi z / L_z)\cos^2(\pi y / L_\theta) \text{ with} \begin{cases} -\frac{L_z}{2} \le z \le \frac{L_z}{2} \\ -\frac{L_\theta}{2} \le y \le \frac{L_\theta}{2} \end{cases} \tag{7-13}$$

Wullschleger (2006) provided two empirical formulas for the critical dent dimensions (Eqs 7-14 and 7-15), but these formulas are only expected to be valid when the dent is shallow.

$$\frac{L_{zw}}{2\lambda_c} = 1 + 1.5\left(\frac{\delta_0}{t_s}\right)^2 \qquad \text{for} \quad 0 < \delta_0 < \delta_0^* \tag{7-14}$$

$$\frac{L_{\theta w}}{2\lambda_c} = 2.62 + 4.5\left(\frac{\delta_0}{t_s}\right)^3 + 5.10^{-5} Z \quad \text{for } 0 < \delta_0 < \delta_0^* \tag{7-15}$$

where L_{zw} and $L_{\theta w}$ are the dent height and width respectively in the Wullschleger study, Z is the Batdorf parameter (Eq. 2-2) and λ_c is the length of the classical axisymmetric buckling half wave length (Yamaki, 1984; Rotter, 2004):

$$\lambda = \frac{\pi}{(12(1-\nu^2))^{1/4}}\sqrt{Rt} = 1.73\sqrt{Rt} \tag{7-16}$$

δ_0^* is the marginal initial dent amplitude for the critical dimensions of Eqs 7-14 and 7-15 where it is around $\delta_0^* = 0.7t_s$ for the example shell of this study. A comparison between the dent dimensions obtained in the present study for 2D-A form (Eqs 7-9 and 7-6) and that given in Wullschleger (2006) (Eqs 7-14 and 7-15) is shown in Fig. 7-16. In this comparison, the dent shape of Wullschleger (Eq. 7-13) was used for the both sets of dimensions.

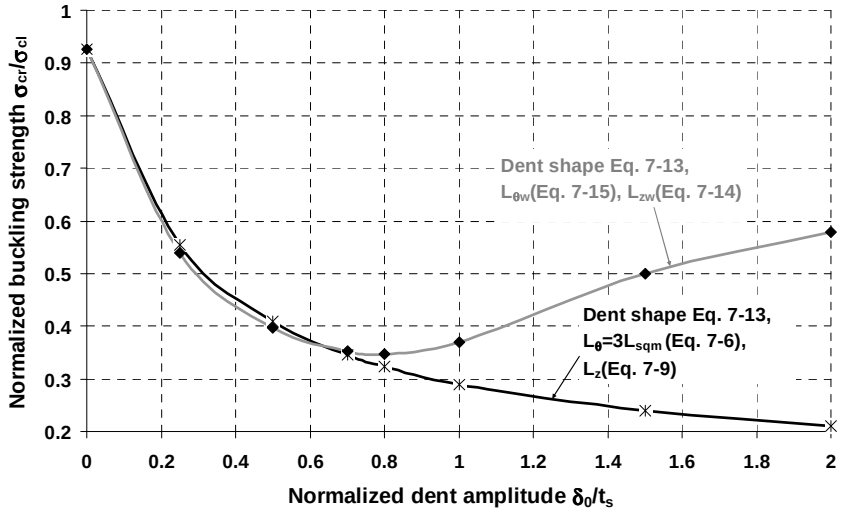

Fig. 7-16: Buckling strength for different dent amplitudes.

It is clear from Fig. 7-16 that the dent dimensions of Wullschleger (2006) give a critically low strength when the dent depth is small (less than $\delta_o = 0.7t_s$ for the example shell). Nevertheless using the dent dimensions of this chapter, a buckling strength obtained which is very close to that of Wullschleger (2006) for small dent amplitudes, but which exhibits a much lower strength when a large dent value is used. However, the dent shape of Eq. 7-13 is not a very good one, as it involves an

abrupt change of curvature at the edge of imperfection. The shape provided in the present study is better (Eq. 7-1).

The buckling strengths based on the empirical formulas found in this study are compared in Fig. 7-17 with those of Rotter and Teng (1989) for the cylindrical shell with an axisymmetric imperfection (Type A; Eq. 6-2).

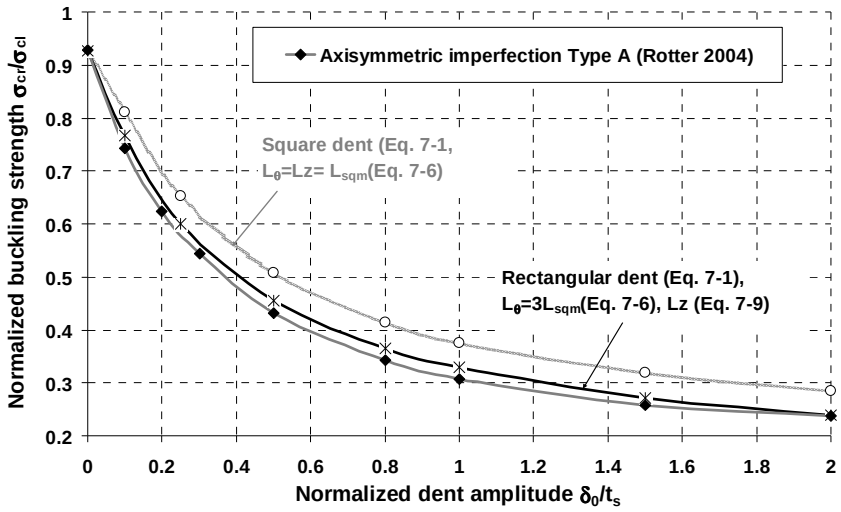

Fig. 7-17: The buckling strength for different shapes of dent.

The rectangular dent has a lower buckling strength than a square dent (Fig. 7-17), but the axisymmetric imperfection still produces the greatest reductions in the shell strength, as indicated in Rotter and Teng (1989). Although the axisymmetric dent has a particularly low strength, it is unlikely to be found as a fully axisymmetric depression. Thus, the critical rectangular dent of this study is a valuable form for theoretical studies of a practical nature, since it has a realistic credible form and produces rather low buckling strengths.

7.5 Buckling of FRP-Strengthened cylinder with a dent

The effectiveness of strengthening a shell with a local rectangular dent by using externally bonded FRP is explored here for the same example shell. The rectangular dent was assumed to have a width $L_\theta=3L_{sqm}$, where L_{sqm} is given in Eq. 7-6, and L_z is determined from Eq. 7-9, since this gave the lowest unrepaired buckling strength. The amplitude of the dent δ_0 was taken as $2t_s$.

The shell was assumed to be externally bonded with a CFRP sheet. The FRP sheet was modelled as an orthotropic material with the elastic moduli E_L of 230GPa in the fibre direction, E_T of 3GPa in the transverse direction and a Poisson's ratio ν_{LT} of 0.35 (Section 3.2). The adhesive layer thickness is taken as t_a=1mm, and the isotropic adhesive was assumed to have a Young's modulus E_a=3GPa and a Poisson's ratio ν_a=0.35.

Normalized load-displacement curves are shown in Fig. 7-18 for three values of the normalized flexural stiffness parameter $E_L t_f^3/E_s t_s^3$. These are compared with the curve for the unstrengthened shell.

The normalised buckling strength of the shell σ_{cr}/σ_{cl} can be significantly increased from the unstrengthened value 0.24 to a repaired value of 0.28 (nearly20% increase) when the dent is patched with a thin FRP lamina with the FRP fibres in the circumferential direction, and with a bending stiffness ratio $E_L t_f^3/E_s t_s^3$=0.5 and with FRP covering the dent area (Fig. 7-19) with $A_{frp}=A_{dent}=L_\theta \times L_z$. The buckling strength is further increased if the FRP bending stiffness is further increased (Fig. 7-18).

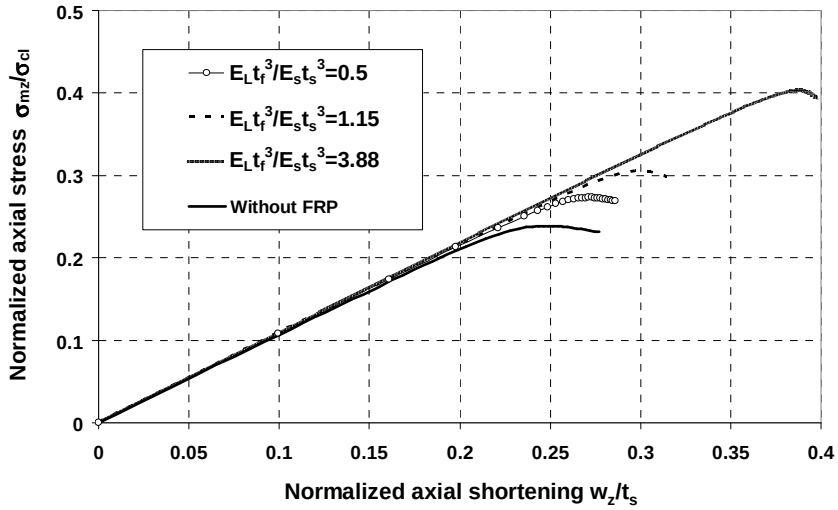

Fig. 7-18: Effect of FRP stiffness on axial stress-axial shortening curve (β=0 (Fig. 3-4), A_{FRP}/A_{dent}=1, δ_0/t_s=2).

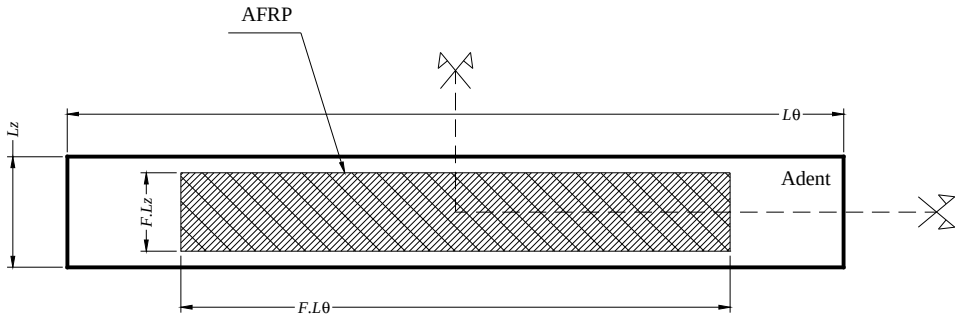

Fig. 7-19: The FRP area (A_{FRP}).

The circumferential and axial deformed shapes at buckling are shown in Figs 7-20 and 7-21 respectively. These show that the FRP reduces the deformations. This reduction is particularly pronounced when the FRP stiffness is very large. With very stiff FRP, the buckling mode becomes more complex and includes significant deformations outside the FRP sheet as shown in Fig. 7-21. The very large axial extent of the buckle is clear in Fig. 7-21. This confirms the finding in Chapter 6 that extended heights of FRP may have a significant influence on the buckling strength if the dent is deep (e.g. $\delta_0/t_s=2$).

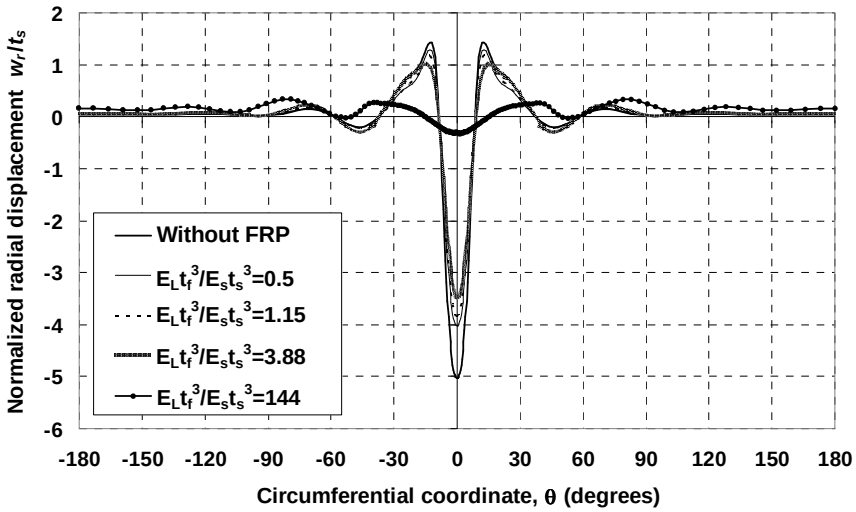

Fig. 7-20: Radial deformation around the circumference through the centre of the dent at the ultimate limit state ($z=0$, $\beta=0$, $A_{FRP}/A_{dent}=1$, $\delta_0/t_s=2$).

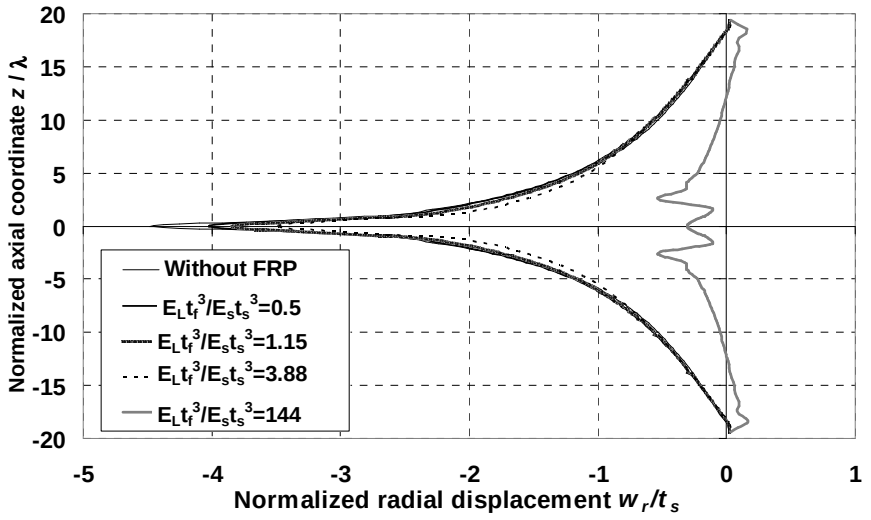

Fig. 7-21: Radial deformation along the axial axis through the centre of the dent at the ultimate limit state ($\theta=0$, $\beta=0$, $A_{FRP}/A_{dent}=1$, $\delta_0/t_s=2$).

The effect of the orientation of the FRP fibres on the buckling strength was studied next. For a normalized FRP bending stiffness in the fibre direction $E_Lt_f^3/E_st_s^3$=1.15 and the same area of the dent (A_{FRP}/A_{dent}=1), the result is shown in Fig. 7-22. The mechanical properties of the FRP lamina were obtained from Section 3.3. From Fig. 7-22, it can be seen that changing the angle of the fibres to the circumferential axis (β in Fig. 3-4) decreases the cylinder buckling strength. Low buckling strengths are observed when the fibres are oriented vertically ($\beta=90^o$).

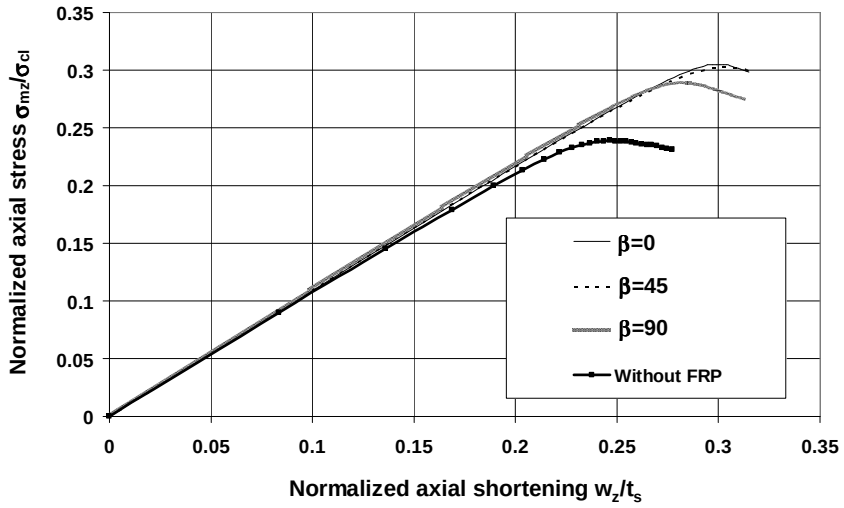

Fig. 7-22: Effect of normalised FRP area on axial stress-axial shortening curve ($E_Lt_f^3/E_st_s^3$=1.15, $A_{FRP}/A_{dent}=1$, $\delta_0/t_s=2$)

The moduli for the FRP sheet at different fibre orientations are shown in Fig. 7-23, which has the same shape as the figure provided by Cripps (2002).

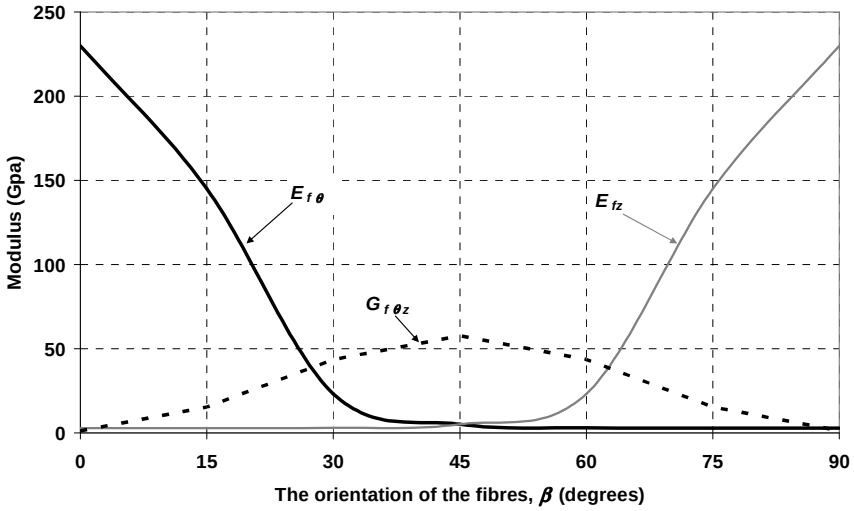

Fig. 7-23: The moduli for the FRP sheet with different fibre orientations.

The Young's modulus for the FRP sheet in the circumferential direction $E_{f\theta}$ falls rapidly when the fibre orientation moves away from the circumferential direction. At the same time, an enhancement in the Young's modulus in the meridional direction E_{fz} can be observed. The shear modulus, $G_{f\theta z}$, naturally reaches its maximum value at 45 degrees. Figure 7-23 shows that the low buckling strength obtained when the fibres are at β=90^{o} (Fig. 7-22) should be expected, because the circumferential stiffness is very small and a high circumferential stiffness is needed to reduce the imperfection sensitivity.

The effect of increasing the area of the shell covered with FRP is shown in Fig. 7-24, where it is clear that the FRP can be effective even if only the middle quarter of the dent is covered. The buckling strength rises as the FRP area is increased, but this rise is less than proportional to the area. The width and height of the FRP are here taken as proportion to L_θ and L_z respectively (Fig. 7-19).

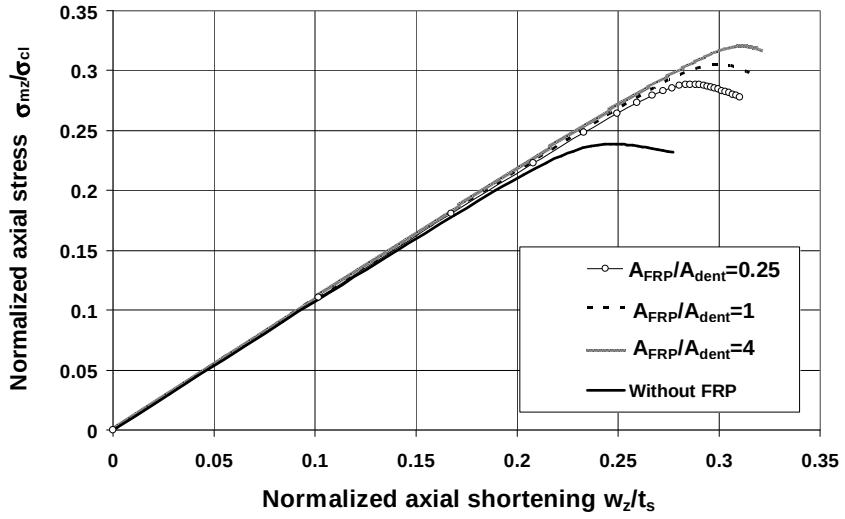

Fig. 7-24: Effect of normalised FRP area on axial stress-axial shortening curve ($E_L t_f^3/E_s t_s^3$=1.15, β=0, δ_0/t_s=2)

To obtain a fuller picture, a more detailed study was undertaken. The buckling strength is obtained (Fig. 7-25) for different FRP bending stiffnesses ($\alpha_b=E_L t_f^3/E_s t_s^3$) and different fibre orientations (β) relative to the circumferential axis.

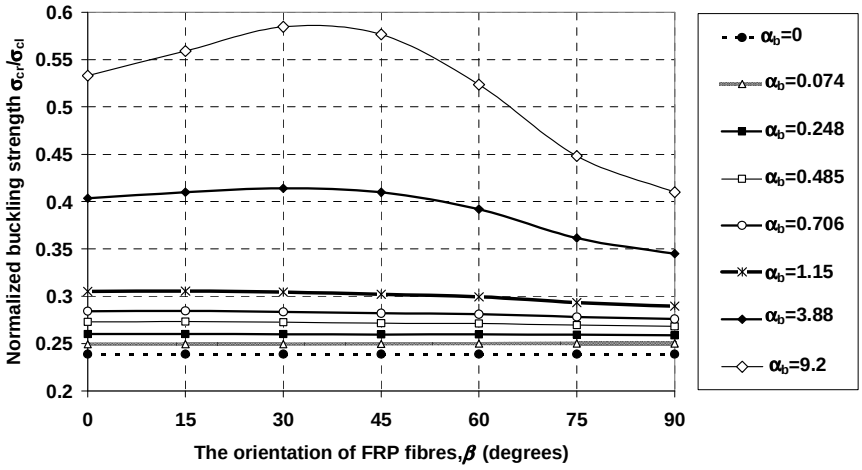

Fig. 7-25: The buckling strength for different FRP stiffnesses and different orientations (A_{FRP}/A_{dent}=1, δ_0/t_s=2)

As expected, an increased FRP thickness enhances the buckling strength (Fig. 7-25). On the other hand, the fibre orientations affect the buckling axial load. For a practical thin FRP thickness (α_b<1.15), the buckling load is steadily reduced as the orientation of the fibres changes from 0^o to 90^o. With a very stiff FRP sheet, the fibre orientation around 30^o registers the highest buckling strength. This increased strength

when a stiff FRP sheet has its fibres oriented at 30° to the circumferential axis suggests that the shear modulus of the sheet (Fig. 7-23) may become important for these rectangular dents, but the overall reason is not yet clear.

More detail can be seen in Fig. 7-26 for the effectiveness of the FRP area with an FRP stiffness ratio of $\alpha=E_L t_f^3/E_s t_s^3$ of 1.15 and different fibre orientations.

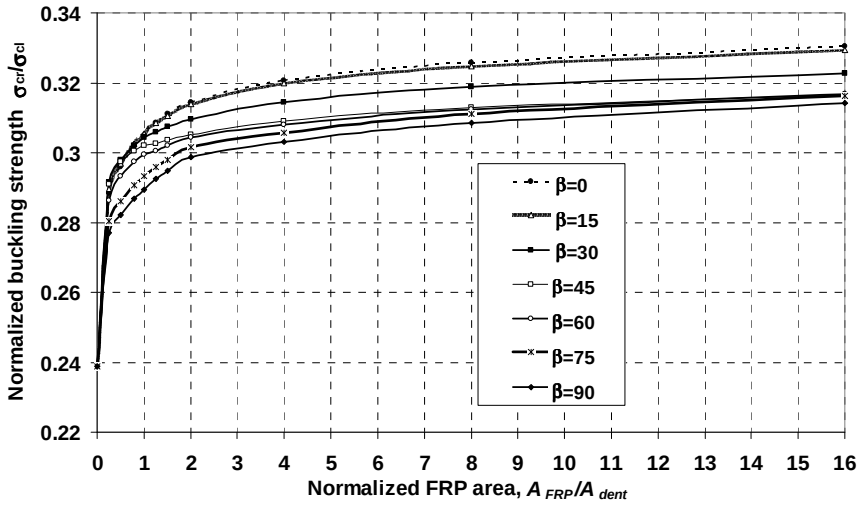

Fig. 7-26: The buckling strength for different FRP area and different orientations ($E_L t_f^3/E_s t_s^3$ =1.15, δ_0/t_s=2).

It is clear that the FRP can provide the cylinder with a much higher buckling strength when only a small area is covered (quarter of the dent area). The buckling strength is steadily further increased as this area grows. The fibre orientation of β=0 always provides the highest buckling strength.

7.6 Summary

This chapter has described the buckling strength of an axially compressed cylindrical shell with a local dent imperfection. A careful study was undertaken of different forms of imperfection, different shapes of local dent and different imperfection amplitudes. The conditions for the lowest strengths were identified, and careful checks made against the proposals of several other researchers. These comparisons showed that the present study has identified the most critical dent geometries and imperfection forms. A new repair method has been proposed to strengthen the shell locally in the area of the dent using externally bonded FRP. The

effectiveness of this method has been explored numerically using Geometrically Nonlinear Analysis with Imperfections (GNIA). For the worst rectangular dent, the effects of the FRP flexural stiffness, fibre orientations and the FRP area have been investigated. The results have shown that the buckling strength can be very significantly enhanced by bonding a small amount FRP locally within the dent zone.

Chapter 8

Conclusions and recommendations

8.1 Summary

Many analyses of cylindrical shells have been performed in this thesis to investigate the effectiveness of FRP composites to increase the buckling capacity of thin metal cylindrical shells.

Two loading conditions were applied: uniform internal pressure accompanied by axial load, and axial loads with geometric imperfections. The local imperfections were divided into two categories: an inward axisymmetric imperfection and a local dent imperfection. The imperfection amplitude was defined by the ratio δ_0/t_s where δ_0 is the imperfection depth at the centre of the imperfection and t_s is the metal thickness.

An analytical method was used first to derive the general equations governing the linear elastic behaviour of an FRP-strengthened cylindrical shell under internal pressure accompanied by axial force. Then, nonlinear finite element analysis was performed, using the ABAQUS program, to obtain all the results involving non linear analysis. The modified Riks routine (arc length technique) was used to trace all the nonlinear paths.

The example cylinder used in all the example calculations was chosen to have a radius to thickness ratio *R/t* of 1000 and corresponded to a medium- length

cylindrical shell. The metal cylinder was assumed to be made of an isotropic metal with Young's modulus E_s of 200 GPa and Poisson's ratio ν_s of 0.3. On the other hand, the FRP sheet was treated as orthotropic, with Young's modulus $E_{f\theta}$ in the circumferential direction, and E_{fz} in the meridional direction with a Poisson's ratio in the circumferential direction, $\nu_{f\theta}$.

The enhancement of the buckling strength achieved by using the bonded FRP was shown using the ratio of the axial stress at the buckling to the classical elastic critical buckling stress σ_{mx}/σ_{cl} or σ_{cr}/σ_{cl}.

In this chapter, the conclusions obtained from each of the studied problems are reviewed.

Finally, recommendations for future research work are suggested.

8.2 FRP preventing radial displacements in pressurized cylinders, Linear elastic Analysis (LA)

Chapter 4 presented an initial linear elastic study of the strengthening of a pressurized cylindrical shell using externally bonded FRP. The FRP sheet was assumed to consist of uniaxial fibres in the circumferential direction.

The general linear elastic equations for the FRP-strengthened cylinder were derived for both pinned base and fixed base boundary conditions.

Decreasing the radial displacement was the main concern in that chapter because radial displacements are closely linked to the circumferential stresses, which couple with the axial compression to cause premature failure by elephant's foot buckling.

The optimal FRP thickness t_f and FRP height h_f together with the optimal starting point for the FRP sheet above the base x_f were estimated for this purpose, using the equations obtained in that chapter.

It was found that a small amount of FRP sheet centred on the location where the radial displacement peaked in the unstrengthened cylinder is very effective in reducing the maximum deflection near the base to the membrane theory deflection. Moreover, both too little and too much FRP lead to higher radial deformations than the optimal amount.

8.3 Strengthening cylindrical shells against elephant's foot buckling using FRP

In chapter 5, the stability of a metal cylinder under high internal pressure accompanied with axial load was discussed.

Geometrically and Materially Nonlinear Analysis (GMNA) was used to study the elastic-plastic collapse by elephant's foot buckling of a simply supported metal cylindrical shell where the stress strain curve was assumed to be perfectly elastic-plastic with no hardening.

The analysis was done using the 2-node axisymmetric general-purpose shell element (SAX1) and the finite element analysis program ABAQUS.

The effect of circumferential uniaxial-fibre FRP strengthening on the elastic-plastic buckling strength of a cylinder of radius to thickness ratio R/t=1000 was established. The valuable gain in buckling strength was achieved using a small amount of FRP composite.

For the example cylinder, the optimal FRP thickness t_f, FRP height h_f and FRP starting distance above the base x_f were found with appropriate reference to the fabrication quality classes of Eurocode3 Part1.6 (2007). The aim was to increase the elastic-plastic collapse strength of the unstrengthened cylinder up to the limits of membrane yield (von Mises) or the elastic imperfect buckling strength. Then, empirical formulas for these three optimal FRP parameter values were produced.

It was shown clearly that if different values of the FRP parameters from the optimal ones were chosen, the strength could be significantly reduced. Further, the sensitivity of the buckling load to the starting distance x_f for the FRP above the base is much less than the sensitivity to the values of other two FRP parameters t_f or h_f. Furthermore, the buckling strength is more sensitive to the FRP height h_f than to the FRP thickness t_f in the membrane yield limit, whereas the reverse can be said for elastic buckling conditions.

8.4 Elastic buckling of FRP-strengthened cylinders with axisymmetric imperfections

Chapter 6 presented an initial study of the elastic buckling strength of an FRP-strengthened cylindrical shell with an axisymmetric inward imperfection.

Under uniform axial load applied at the top of the cylinder and an imperfection shape of weld Type A (Rotter and Teng, 1989), the strength obtained was limited by the elastic bifurcation buckling.

The example cylinder was assumed to have a radius to thickness ratio of 1000, and corresponds to a medium length cylinder with free boundary conditions, except for both rotations about the circumference and the circumferential displacement.

This axisymmetric inward imperfection was placed at the mid-height of the cylinder and the interaction between the neighbouring similar imperfections was ignored.

Geometrically Nonlinear Analysis with Imperfections (GNIA) was undertaken in this study using the finite element package ABAQUS and the modified Riks method. The 4-node doubly curved thin shell element S4R was used to model first the cylinder and then both the FRP and the adhesive in the next step.

The FRP was taken as uniaxial fibres in the circumferential direction. An adhesive layer of finite thickness was assumed between the FRP and the metallic cylinder. The adhesive layer was assumed to have isotropic properties with a low modulus.

Because of the expected high participation of the bending stiffness in the elastic buckling behaviour, the bending stiffness of the FRP sheet relative to that of the metal shell $E_{f\theta}t_f^3/E_st_s^3$ was used to explore the effectiveness of the FRP strengthening in enhancing the buckling strength. It was shown that a significant gain in buckling strength is obtained if this flexural stiffness is large. It was shown that the increased buckling strength of an FRP repaired shell depends on the change of flexural stiffness caused by the FRP, not the change in extensional stiffness. It was also shown that a thick layer of adhesive is very beneficial in raising the buckling strength, and this differs considerably from other applications of FRP to strengthen structures.

The buckling strength was found to increase when the height of the zone covered by the FRP is increased.

The study was extended to cover different imperfection amplitudes. In all cases, the buckling strength was enhanced when FRP composites were applied, but the FRP repair for elastic buckling was much less effective than its use to prevent elastic-plastic collapse by elephant's foot buckling. This conclusion was clear when the imperfection was deep (e.g. δ_0/t=2). The reason is that a circumferential FRP sheet is very effective in resisting the circumferential tension caused by a high internal pressure in the case of elephant's foot buckling, but it is less effective when an increase in the elastic buckling strength depends on achieving an increased flexural stiffness.

Studies of changes in the height of the FRP sheet showed that the buckling strength continued to rise even when the sheet extended for beyond the imperfection (at least for deep imperfection). The reason was found in the shape of the bifurcation mode, which has a large axial range for deep imperfections. This difference between a repair covering the imperfection and a repair covering the buckling mode has not been recognized before.

In conclusion, this study has shown that bonding FRP to the exterior of an imperfect shell can be a new economical repairing technique, even when only a relatively small zone is strengthened.

8.5 Using FRP in strengthening the elastic buckling of thin metallic cylinders with a single local dent

In Chapter 7, the bifurcation buckling of a cylindrical shell with a single local dent was studied first. The effectiveness of FRP strengthening to increase the buckling strength was then explored.

The cylinder was subjected to a uniform axial load at the top. A cylinder of radius to thickness ratio R/t of 1000 was chosen, corresponding to a medium length cylinder with free boundary conditions, except for rotations about the circumference and the circumferential displacement.

Geometrically Nonlinear Analysis with Imperfections (GNIA) was undertaken using the finite element package ABAQUS and modified Riks method. The 4-node

doubly curved thin shell element S4R was used to model the metal cylinder first and for both the FRP and adhesive in the next step.

A local single dent was studied at the mid-height of the cylinder and the buckling strength was calculated for different shapes and sizes of this dent.

A 2D imperfection in a form similar to the Type A weld depression of Rotter and Teng (1989) was chosen. When the buckling strength predictions were compared with previously published test results, this imperfection was found to give a reasonably satisfactory match. This imperfection has the advantage that no discontinuities of slope or curvature occur at the edges of the imperfect zone. Such discontinuities lead to high local stresses, so may be unrealistic.

Two shapes for dent zone were considered: square dent and rectangular dent. The critical dent sizes which lead to the minimum buckling strength were obtained for different dent amplitudes. Empirical formulas to represent these sizes were derived.

It was shown that a rectangular dent with a width L_θ equal to $3L_{sqm}$ (where L_{sqm} is the critical size of a square dent) produces the lowest buckling strength, but the complete axisymmetric imperfection still causes the greatest reduction in the bifurcation buckling strength of the shell.

The rectangular dent of width $3L_{sqm}$ and amplitude $\delta_0/t_s=2$ was chosen to be repaired, using an FRP lamina with Young's modulus E_L in the fibre direction and E_T in the transverse direction and Poisson's ratio ν_{LT}. An isotropic adhesive layer was installed between the FRP and metal.

The effects of the FRP stiffness, fibre orientation and FRP area were investigated. It was shown that a thin FRP lamina increased the buckling strength significantly. Fibres oriented in the circumferential direction provide a higher buckling strength than other orientations for practical FRP thicknesses. The lowest buckling strength was observed when the fibres were oriented vertically.

The elastic buckling strength of the cylinder was found to rise significantly when the FRP area is increased. However, the FRP became effective even if only the middle quarter of the dent was covered.

Thus, FRP composite material applied to a small zone at the centre of the dent can provide a significant enhancement in strength. This is a new technique to raise the elastic buckling strength of an imperfect cylinder.

8.6 Recommendations for future work

In this thesis, FRP composites have been used as a new technique to raise the buckling strength of a cylindrical metal shell under two loading conditions: internal pressure accompanied with axial load and uniform vertical load with imperfections. Within the limited time available for this research, the studies have demonstrated that FRP can be used effectively to enhance the stability of the cylindrical part of a steel tank or silo, but the author believes that there are still some questions that should be addressed. The following are some suggestions for future work.

In all the cases studied in this thesis, the cylinder radius to thickness ratio R/t was 1000. Therefore, there is an important question about the effect of changing this ratio. For example, in the case of elephant's foot buckling under high internal pressure, the elastic-plastic collapse strength changes when the radius to thickness ratio is changed, so new optimal FRP dimensions need to be obtained by changing this ratio. For the imperfect cylinder under axial load only, the buckling strength was found by Rotter and Teng (1989) to be independent of the radius to thickness ratio. However, the required amount of FRP to achieve a certain degree of strengthening may depend on R/t.

This thesis dealt with the FRP sheet as one layer. It may be that useful gains can be made using a layered FRP sheet with different fibre orientations for each layer. The effectiveness of the adhesive between the FRP layers needs to be explored as this can increase the flexural stiffness. It is clear that the final buckling strength may be connected with a new FRP flexural stiffness related to the number of the layers and the fibre orientation of each layer.

In Chapter 7, the fibre orientation was discussed without exploring the $E_{fz}/E_{f\theta}$ ratio itself. Therefore, this question needs additional work to be answered from the thinking that it will have a significant influence on the buckling strength.

In Chapter 7, the effectiveness of the FRP strengthening was studied, using one imperfection amplitude of δ_0/t_s=2. This study certainly needs to be extended to different imperfection amplitudes.

In this study, a continuous FRP sheet was bonded externally to the metal cylinder. A useful question needs to be answered about the effect of non-continuous FRP sheet. The effect of separated FRP strips on the buckling strength has not been studied. Is it more economical than the continuous one? What are the distance limits required between these strips for them to be effective?.

Finally, different load patterns, such as seismic loading, wind loading, external pressure loading etc., could be usefully explored in future studies.

References

ABAQUS, Version 6.5-4 (2005). ABAQUS/Standard User's Manual, ABAQUS Inc, USA.

Ashton JE, Halpin JC and Petit PH (1969). "Primer on composite materials". Analysis Technonic Publishing Co., Inc., Stamford, Conn., P.113.

Åström BT (1997). "Manufacturing of polymer composites". Chapman and Hall, London, UK.

Baker EH, Kovalevsky L, Rish FL (1986). "Structural analysis of shells". Robert E. Krieger publishing company, third edition, Florida.

Batikha M, Chen JF and Rotter JM (2007a). "FRP strengthening of metallic cylindrical shells against elephant's foot buckling." Proc. Of the Conference on Advanced composites in Construction, ACIC 07, 2-4 April, Bath, UK, 157-164.

Batikha M, Chen JF and Rotter JM (2007b). "Numerical modelling of shells repaired using FRP." Proc. of the 3rd international Conference on steel and composites structures, ICSCS07, 30July-1 August, Manchester, UK, 1065-1069.

Batikha M, Chen JF, Rotter JM (2007c). "Elastic buckling of FRP-strengthened cylinders with axisymmetric imperfections". Proc., Asia-Pacific Conference on FRP in Structures, APFIS2007, 12-14 December, Hong Kong, 1011-1016.

Batikha M, Chen JF, Rotter JM (2008). "Strengthening metallic shells with FRP against buckling". Proc. Of the 4th international conference on FRP composites in civil engineering, CICE2008, 22-24 July, Zurich, Switzerland, accepted.

Berry PA, Rotter JM and Bridge RQ (2000). "Compression tests on cylinders with circumferential weld depressions". Jnl of Engineering Mechanics, 126(4), 405-413.

BS EN 1991-4 (2006). Eurocode 1- Actions on structures, Part 4: silos and tanks. Brussels; CEN.

Cadei. JMC, Stratford TJ, Hollaway LC and Duckett WG (2004). Strengthening metallic structures using externally bonded fibre- reinforced polymers. CIRIA, C595, London.

Chaallal O, Hassan M and LeBlank M (2006). "Circular columns confined with FRP: Experimental versus predictions of models and guidelines". Journal of Composites for Construction, 10(1), 4-12.

Chajes A (1985). "Stability and collapse of axially compressed cylindrical shells". In: Narayanan, R. editor. "Shell structures- Stability and strength". Elsevier science publishing, Essex, UK, 1-17.

Chen JF and Teng JG (2001). "Anchorage strength models for FRP and steel plates bonded to concrete". Journal of Strctural Engineering, 127(7), 784-791.

Chen JF (2002). "Load-bearing capacity of masonry arch bridges strengthened with fibre reinforced polymer composites". Advances in Structural Engineering, 5(1), 37-44.

Chen JF, Rotter JM and Teng JG (2005). "Strengthening silos and tanks against elephant's foot buckling". Proc. 4th International Conference on Advances in Steel Structures, ICASS 05, 13-15 June, Shanghai, China, 459-466.

Chen JF, Rotter JM and Teng JG (2006). "A simple remedy for elephant's foot buckling in cylindrical silos and tanks". Advances in Structural Engineering, 9(3), 409-420.

Concrete Society (2004). "Design guidance for strengthening concrete structures using fibre composite materials ". Technical Report 55, second edition, Camberley, UK.

Cripps A (2002). "Fibre-reinforced polymer composites in construction". CIRIA, C564, London.

Ebead U, Marzouk H (2004). "Fiber-reinforced polymer strengthening of two way slabs". ACI Structural Journal, 101(5), 650-659.

EN 1993-1-6 (2007) Eurocode 3: Design of steel structures—Part 1-6: Strength and stability of shell structures. Brussels: CEN.

Enochsson O, Lundqvist J, Täljsten B, Rusinowski P, Olofsson T (2007). “CFRP strengthened openings in two-way concrete slabs –An experimental and numerical study”. Construction and Building Materials, 21, 810-826.

Flügge W (1973). “Stresses in shells”. Springer- Verlag, second edition, Berlin.

Gavrilenko GD (2007). “Transformed initial dent as a trigger of the post-buckling process”. Thin-walled structures, 45(10-11), 840-844.

Gavrilenko GD and Krasovskii VL (2004). “Stability of circular cylindrical shells with a single local dent”. Jnl of strength of materials, 36(3),260-268.

Geier B and Singh G (1997). “Some simple solutions for buckling loads of thin and moderately thick cylindrical shells and panels made of laminated composite material”. Aerospace Science and Technology, n^{o} 1, 47-63.

Geier B, Meyer-Piening HR and Zimmermann (2002). “On the influence of laminate stacking on buckling of composite cylindrical shells subjected to axial compression”. Composite Structures, 55, 467-474.

Gilfillan JR, Gilbert SG and Patrick GRH (2003). “The use of FRP composites in enhancing the structural behavior of timber beams”. Journal of Reinforced Plastics and Composites, 22(15), 1373-1388.

Gillie M and Rotter JM (2002). “The effects of patch loads on thin-walled steel silos”. Jnl of Thin- Walled Structures, 40 ,835-852.

Greiner R and Derler P (1995). “Effect of Imperfections on Wind-Loaded Cylindrical Shells”. Thin- Walled Structures, 23, 271-281.

Greiner R (1998). “Cylindrical shell: wind loading”. In: Brown CJ and Nielsen J, editors. “silos: Fundamentals of theory, behaviour and design”. E & FN Spon, London, 378-399.

Greiner R (2004). “Cylindrical shells under uniform external pressure”. In: Teng JG, Rotter JM, editors. “Buckling of thin metal shells”. Spon press, London, 154-174.

Greiner R and Guggenberger W (2004). “Tall cylindrical shells under wind pressure”. In: Teng JG, Rotter JM, editors. “Buckling of thin metal shells”. Spon press, London, 198-206.

Highways Agency (2002). “Strengthening of concrete bridge supports using fibre reinforced polymers”. BD 84/02, Design manual for roads and bridges. Volume 1,

Highway structures: approval procedures and general design. Section 3, General design. Part 16, Department of Transport, London.

Jamal M, Midani M, Damil N and Potier-Ferry M (1999). “Influence of localized imperfections on the buckling of cylindrical shells under axial compression”. International Journal of Solids and Structures, 36(3), 441-464.

Jamal M, Lahlou L, Midani M, Zarouni H, Limam A, Damil N and Potier-Ferry M (2003). “A semi-analytical buckling analysis of imperfect cylindrical shells under axial compression”. International Journal of Solids and Structures, 40(5), 1311-1327.

Koiter W. (1945). "On the stability of elastic equilibrium". Ph.D. Thesis, Delf. English translation, NASA Techn. Trans. F10, 1967.

Lorenz R (1908). “Achsensymmetrische Verzerrungen in Duennwandigen Holhlzylindern.” Zeitschrift VDI, 52, 1706-1713.

McCrum NG, Buckley CP and Bucknall CB (1997). “Principles of polymer engineering”. Oxford University press, second edition, Oxford, UK.

Mirmiran A, Shahawy M, Samaan M, Echary HEI, Mastrapa JC and Pico O (1997). “Effect of column parameters on FRP-confined concrete”. Journal of Composites for construction, 2(4), 175-185.

Photiou NK, Hollaway LC and Chryssanthopoulos MK (2006). “Buckling Strengthening of an artificially degraded steel beam utilising a carbon/glass composite system”. Construction and Building Materials , 20, 11-21.

Pircher M and Bridge RQ (2001). “Buckling of thin-walled silos and tanks under axial load—some new aspects”. Journal of Structural Engineering, 127(10), 1129-1136.

Riks E (1979). “An incremental approach to the solution of snapping and buckling proplems”. International Journal of Solids and Structures, 15(7), 529-551.

Rotter JM (1985a). “Membrane theory of shells for bins and silos”, Design of Steel bins for the Storage of Bulk Solids, School of Civil and Mining Engineering, University of Sydney, 58-70.

Rotter JM (1985b). “Bending theory of shells for bins and silos”, Design of Steel bins for the Storage of Bulk Solids, School of Civil and Mining Engineering, University of Sydney, pp 71-81.

Rotter JM (1989). “Stress amplification in unstiffened cylindrical steel silos and tanks”. Institution of Engineers, Australia, Civil Engrg Transactions, CE31(3), 142-148.

Rotter JM and Teng JG (1989). “Elastic stability of cylindrical shells with weld depressions”. Journal of Structural Engineering, 115(5), 1244-1263.

Rotter JM and Zhang Q (1990). “Elastic buckling of imperfect cylinders containing granular solids”. Journal of Structural Engineering, 116(8), 2253-2271.

Rotter JM (1990). “Local collapse of axially compressed pressurized thin steel cylinders”. Journal of Structural Engineering, 116(7), 1955-1969.

Rotter JM (1996). “Buckling and collapse internally pressurised axially compressed silo cylinders with measured axisymmetric imperfections: imperfections, residual stresses and local collapse”. The international workshop on imperfections in metal silos: Measurements, Characterisations, and strength analysis. CA-Silo, Lyon, France, 119-140.

Rotter JM (1997). “Design standards and calculations for imperfect pressurised axially compressed cylinders”. *Proc., Int. Conf. on Carrying Capacity of Steel structures*. Brno, 354-360.

Rotter JM (1998). “Cylindrical shells: Symmetrical solids loadings”. In: Brown CJ and Nielsen J, editors. “silos: Fundamentals of theory, behaviour and design”. E & FN Spon, London, 346-366.

Rotter JM (2001). “Guide for the economic design of circular metal silos”. Spon press, London.

Rotter JM (2004). “Cylindrical shells under axial compression”. In: Teng JG, Rotter JM, editors. “Buckling of thin metal shells”. Spon press, London, 42-87.

Seible F, Priestley MJN, Hegemier GA and Innamorato D (1997). “Seismic retrofit of RC columns with continuous carbon fiber jackets”. Journal of composites for construction, 1(2), 52-62.

Singer J, Baruch M and Harari O (1966). “Inversion of the eccentricity effect in stiffened cylindrical shells buckling under external pressure”. Journal of Mechanical Engineering Science, 8(4), 363-373.

Singer J, Baruch M and Harari O (1967). “On the stability of eccentrically stiffened cylindrical shells under axial compression”. International Journal of Solids and Structures, 3(4), 445-470.

Singer J, Arbocz J and Weller T (1998). “Buckling experiments- Experiments methods in buckling of thin-walled structures ”. John Wiley and Sons, New york, volume 1.

Singer J, Arbocz J and Weller T (2002). “Buckling experiments- Experiments methods in buckling of thin-walled structures ”. John Wiley and Sons, New york, volume 2.

Singer J (2004). “Stiffened cylindrical shells”. In: Teng JG, Rotter JM, editors. “Buckling of thin metal shells”. Spon press, London, 286-343.

Smith ST and Teng JG (2002). “FRP-strengthened RC beams. I: review of debonding strength models”. Engineering structures, 24, 385-395.

Southwell RV (1914). “On the General Theory of Elastic Stability.” Phil. Trans. Roy. Soc. of London, Series A, 213, 187-244.

Spagnoli A. (2003). "Koiter circles in the buckling of axially compressed conical shells". International Jnl of Solids and structures, 40(22), 6095-6109.

Stratford T and Cadei J (2006). “Elastic analysis of adhesion stresses for the design of a strengthening plate bonded to a beam”. Construction and Building Materials , 20, 34-45.

Teng JG and Rotter JM (1992). “Buckling of pressurized axisymmetrically imperfect cylinders under axial loads”. Journal of Engineering Mechanics, 118(2), 229-247.

Teng JG, Lam L, Chan W and Wang J (2000). “Retrofitting of deficient RC cantilever slabs using GFRP strips”. Journal of composites for construction, 4(2), 75-84.

Teng JG, Cao SY and Lam L (2001). “Behaviour of GFRP strengthened RC cantilever slabs”. Construction and Building Materials, 15, 339-349.

Teng JG, Chen JF, Smith ST and Lam L (2002). “FRP Strengthened RC Structures”. John Wiley and Sons, Chichester, UK.

Teng JG and Lam L (2004). “Behavior and modeling of fiber reinforced polymer-confined concrete”. Journal of Structural Engineering, 130(11), 1713-1723.

Teng JG and Hu YM (2004).”Suppression of local buckling in steel tubes by FRP jacketing”. Proc. Of the 2nd International Conference on FRP Composites in Civil Engineering. Adelaide, Australia, 8-10 December, 749-753.

Teng JG and Rotter JM (2004). “Buckling of thin shells- An overview”. In: Teng JG, Rotter JM, editors. “Buckling of thin metal shells”. Spon press, London, 1-41.

Teng JG and Zhao Y (2004).“Rings at shell junctions”. In: Teng JG, Rotter JM, editors. “Buckling of thin metal shells”. Spon press, London, 409-454.

Teng JG, Hu YM (2007). “Behaviour of FRP-jacketed circular steel tubes and cylindrical shells under axial comparison”. Construction and Building Materials, 21, 827-838.

Teng JG, Huang YL, Lam L and Ye LP (2007). “Theoretical Model for Fiber-Reinforced Polymer-Confined Concrete”. Journal of composites for construction, 11(2), 201-210.

Thomsen H, Spacone E, Limkatanyu S and Camata G (2004). “Failure Mode Analyses of Reinforced Concrete Beams Strengthened in Flexure with Externally Bonded Fiber-Reinforced Polymers”. Journal of composites for construction, 8(2), 123-131.

Timoshenko S (1910). “Einige Stabilitaetsprobleme Der Elastizitaetstheorie.” Zeitschrift Mathematik und Physik, 58, 337-385.

Timoshenko S (1936). “Theory of elastic stability”. McGraw-Hill book company, New York.

Toutanji H, Saxena P, Zhao L and Ooi T (2007). “Prediction of Interfacial Bond Failure of FRP–Concrete Surface”. Journal of composites for construction, 11(4), 427-436.

Triantafillou TC (1997). “Shear reinforcement of wood using FRP materials”. Journal of Materials in Civil Engineering, 9(2), 65-69.

Triantafillou TC (1998). “Strengthening of masonry structures using epoxy-bonded FRP laminates”. Journal of composites for construction, 2(2), 96-104.

Tsai CT and Palazotto AN (1990). “A modified Riks approach to composite shell snapping using a high-order shear deformation theory”. Computers and structures, 35(3), 221-226.

Tsai CT and Palazotto AN (1991). “Nonlinear and multiple snapping responses of cylindrical panels comparing displacement control and Riks method”. Computers and structures, 41(4), 605-610.

Vinson JR, Sierakowski RL (1986). “The behaviour of structures composed of composite materials”. Martinus Nijhoff publishers, Dordrecht, Netherlands.

Wang LM and Wu YF (2008). “Effect of corner radius on the performance of CFRP-confined square concrete columns: test ”. Engineering structures, 30, 493-505.

Wullschleger L (2006). “Numerical Investigation of the buckling behaviour of axially compressed circular cylinders having parametric initial dimple imperfections”. PhD thesis, Swiss Federal Institute of Technology, Zurich.

Yamaki N (1984).”Elastic stability of circular cylindrical shells”. North-Holland,Amesterdam.

Zienkiewicz OC (1971). “The finite element method in engineering science”. McGraw-Hill publishing company limited, second edition, London.

Appendix I

Matrices [A] and [B] in Equation (4-47): pinned base

For an FRP strengthened cylindrical shell with a pinned base, the coefficients in matrices [A] and [B] in equation (4-47) are given as follows:

$$\left.\begin{aligned} A_{11} &= -\frac{w_m}{w_{mb}} \\ A_{13} &= \cos\varpi_b e^{-\varpi_b} \\ A_{14} &= \sin\varpi_b e^{-\varpi_b} \\ A_{15} &= \cos\varpi_b e^{\varpi_b} \\ A_{16} &= \sin\varpi_b e^{\varpi_b} \end{aligned}\right\} \tag{I-1}$$

$$\left.\begin{aligned} A_{21} &= \frac{1}{F_1} \\ A_{22} &= -\frac{1}{F_1} \\ A_{23} &= -(\sin\varpi_b + \cos\varpi_b)e^{-\varpi_b} \\ A_{24} &= (\cos\varpi_b - \sin\varpi_b)e^{-\varpi_b} \\ A_{25} &= (-\sin\varpi_b + \cos\varpi_b)e^{\varpi_b} \\ A_{26} &= (\cos\varpi_b + \sin\varpi_b)e^{\varpi_b} \end{aligned}\right\} \tag{I-2}$$

$$\left.\begin{aligned} A_{32} &= -\frac{1}{F_2} \\ A_{33} &= -\sin\varpi_b e^{-\varpi_b} \\ A_{34} &= \cos\varpi_b e^{-\varpi_b} \\ A_{35} &= \sin\varpi_b e^{\varpi_b} \\ A_{36} &= -\cos\varpi_b e^{\varpi_b} \end{aligned}\right\} \tag{I-3}$$

$$
\left.
\begin{aligned}
A_{41} &= -\frac{1}{F_3} \\
A_{42} &= -\frac{1}{F_3} \\
A_{43} &= (-\sin\varpi_b + \cos\varpi_b)e^{-\varpi_b} \\
A_{44} &= (\cos\varpi_b + \sin\varpi_b)e^{-\varpi_b} \\
A_{45} &= -(\sin\varpi_b + \cos\varpi_b)e^{\varpi_b} \\
A_{46} &= (\cos\varpi_b - \sin\varpi_b)e^{\varpi_b}
\end{aligned}
\right\} \qquad \text{(I-4)}
$$

$$
\left.
\begin{aligned}
A_{53} &= -\frac{w_{mb}}{w_m} \\
A_{55} &= -\frac{w_{mb}}{w_m} \\
A_{57} &= \cos\varpi_c e^{-\varpi_c} - \cos\varpi_c e^{\varpi_c} \\
A_{58} &= \sin\varpi_c e^{-\varpi_c} + \sin\varpi_c e^{\varpi_c}
\end{aligned}
\right\} \qquad \text{(I-5)}
$$

$$
\left.
\begin{aligned}
A_{64} &= F_2 \\
A_{66} &= -F_2 \\
A_{67} &= \sin\varpi_c e^{-\varpi_c} + \sin\varpi_c e^{\varpi_c} \\
A_{68} &= \cos\varpi_c e^{\varpi_c} - \cos\varpi_c e^{-\varpi_c}
\end{aligned}
\right\} \qquad \text{(I-6)}
$$

$$
\left.
\begin{aligned}
A_{73} &= -F_3 \\
A_{74} &= -F_3 \\
A_{75} &= F_3 \\
A_{76} &= -F_3 \\
A_{77} &= (-\sin\varpi_c + \cos\varpi_c)e^{-\varpi_c} \\
A_{78} &= (\sin\varpi_c + \cos\varpi_c)e^{-\varpi_c} + (-\sin\varpi_c + \cos\varpi_c)e^{\varpi_c}
\end{aligned}
\right\} \qquad \text{(I-7)}
$$

$$
\left.
\begin{aligned}
A_{83} &= F_1 \\
A_{84} &= -F_1 \\
A_{85} &= -F_1 \\
A_{86} &= -F_1 \\
A_{87} &= -(\sin\varpi_c + \cos\varpi_c)e^{-\varpi_c} + (\sin\varpi_c - \cos\varpi_c)e^{\varpi_c} \\
A_{88} &= (-\sin\varpi_c + \cos\varpi_c)e^{-\varpi_c} + (\sin\varpi_c + \cos\varpi_c)e^{\varpi_c}
\end{aligned}
\right\} \qquad \text{(I-8)}
$$

$$
\left.
\begin{aligned}
B_1 &= \frac{w_m}{w_{mb}} - 1 \\
B_5 &= \frac{w_{mb}}{w_m} - 1 + \cos\varpi_c e^{\varpi_c} \\
B_6 &= -\sin\varpi_c e^{\varpi_c} \\
B_7 &= -(\cos\varpi_c + \sin\varpi_c) e^{\varpi_c} \\
B_8 &= (\cos\varpi_c - \sin\varpi_c) e^{\varpi_c}
\end{aligned}
\right\} \qquad \text{(I-9)}
$$

Appendix II

Matrices [A] and [B] in Equation (4-47): fixed base

For an FRP strengthened cylindrical shell with a fixed base, the coefficients in matrices [A] and [B] in equation (4-47) are given as follows.

$$\left.\begin{aligned} A_{11} &= -\frac{w_m}{w_{mb}} \\ A_{13} &= \cos\varpi_b e^{-\varpi_b} \\ A_{14} &= \sin\varpi_b e^{-\varpi_b} \\ A_{15} &= \cos\varpi_b e^{\varpi_b} \\ A_{16} &= \sin\varpi_b e^{\varpi_b} \end{aligned}\right\} \tag{II-1}$$

$$\left.\begin{aligned} A_{21} &= \frac{1}{F_1} \\ A_{22} &= -\frac{1}{F_1} \\ A_{23} &= -(\sin\varpi_b + \cos\varpi_b)e^{-\varpi_b} \\ A_{24} &= (\cos\varpi_b - \sin\varpi_b)e^{-\varpi_b} \\ A_{25} &= (-\sin\varpi_b + \cos\varpi_b)e^{\varpi_b} \\ A_{26} &= (\cos\varpi_b + \sin\varpi_b)e^{\varpi_b} \end{aligned}\right\} \tag{II-2}$$

$$\left.\begin{aligned} A_{32} &= -\frac{1}{F_2} \\ A_{33} &= -\sin\varpi_b e^{-\varpi_b} \\ A_{34} &= \cos\varpi_b e^{-\varpi_b} \\ A_{35} &= \sin\varpi_b e^{\varpi_b} \\ A_{36} &= -\cos\varpi_b e^{\varpi_b} \end{aligned}\right\} \tag{II-3}$$

$$
\left.
\begin{aligned}
A_{41} &= -\frac{1}{F_3} \\
A_{42} &= -\frac{1}{F_3} \\
A_{43} &= (-\sin\varpi_b + \cos\varpi_b)e^{-\varpi_b} \\
A_{44} &= (\cos\varpi_b + \sin\varpi_b)e^{-\varpi_b} \\
A_{45} &= -(\sin\varpi_b + \cos\varpi_b)e^{\varpi_b} \\
A_{46} &= (\cos\varpi_b - \sin\varpi_b)e^{\varpi_b}
\end{aligned}
\right\} \qquad \text{(II-4)}
$$

$$
\left.
\begin{aligned}
A_{53} &= -\frac{w_{mb}}{w_m} \\
A_{55} &= -\frac{w_{mb}}{w_m} \\
A_{57} &= \cos\varpi_c e^{-\varpi_c} - \cos\varpi_c e^{\varpi_c} + 2\sin\varpi_c e^{\varpi_c} \\
A_{58} &= \sin\varpi_c (e^{-\varpi_c} - e^{\varpi_c})
\end{aligned}
\right\} \qquad \text{(II-5)}
$$

$$
\left.
\begin{aligned}
A_{64} &= F_2 \\
A_{66} &= -F_2 \\
A_{67} &= \sin\varpi_c e^{-\varpi_c} + \sin\varpi_c e^{\varpi_c} + 2\cos\varpi_c e^{\varpi_c} \\
A_{68} &= -\cos\varpi_c (e^{\varpi_c} + e^{-\varpi_c})
\end{aligned}
\right\} \qquad \text{(II-6)}
$$

$$
\left.
\begin{aligned}
A_{73} &= -F_3 \\
A_{74} &= -F_3 \\
A_{75} &= F_3 \\
A_{76} &= -F_3 \\
A_{77} &= (-\sin\varpi_c + \cos\varpi_c)e^{-\varpi_c} + (\sin\varpi_c + \cos\varpi_c)e^{\varpi_c} \\
&+ 2(-\sin\varpi_c + \cos\varpi_c)e^{\varpi_c} \\
A_{78} &= (\sin\varpi_c + \cos\varpi_c)e^{-\varpi_c} - (-\sin\varpi_c + \cos\varpi_c)e^{\varpi_c}
\end{aligned}
\right\} \qquad \text{(II-7)}
$$

$$
\left.
\begin{aligned}
A_{83} &= F_1 \\
A_{84} &= -F_1 \\
A_{85} &= -F_1 \\
A_{86} &= -F_1 \\
A_{87} &= -(\sin\varpi_c + \cos\varpi_c)e^{-\varpi_c} + (\sin\varpi_c - \cos\varpi_c)e^{\varpi_c} \\
&\quad + 2(\sin\varpi_c + \cos\varpi_c)e^{\varpi_c} \\
A_{88} &= (-\sin\varpi_c + \cos\varpi_c)e^{-\varpi_c} - (\sin\varpi_c + \cos\varpi_c)e^{\varpi_c}
\end{aligned}
\right\} \qquad \text{(II-8)}
$$

$$
\left.
\begin{aligned}
B_1 &= \frac{w_m}{w_{mb}} - 1 \\
B_5 &= \frac{w_{mb}}{w_m} - 1 + (\cos\varpi_c - \sin\varpi_c)e^{\varpi_c} \\
B_6 &= -(\sin\varpi_c + \cos\varpi_c)e^{\varpi_c} \\
B_7 &= -2\cos\varpi_c e^{\varpi_c} \\
B_8 &= -2\sin\varpi_c e^{\varpi_c}
\end{aligned}
\right\} \qquad \text{(II-9)}
$$